CRANFIELD UNIVERSITY

KALYAN SHRESTHA

INVESTIGATION ON THE ACCURACY OF RANS MODELS FOR UNDER-EXPANDED JET INJECTED INTO A SUPERSONIC CROSS-FLOW

SCHOOL OF ENGINEERING

COMPUTATIONAL FLUID DYNAMICS

MSc THESIS

Academic Year: 2010 - 2011

Supervisor: DR. BEN THORNBER

AUGUST 2011

CRANFIELD UNIVERSITY

SCHOOL OF ENGINEERING

COMPUTATIONAL FLUID DYNAMICS

MSc THESIS

Academic Year 2010 - 2011

KALYAN SHRESTHA

INVESTIGATION ON THE ACCURACY OF RANS MODELS FOR UNDER-EXPANDED JET INJECTED INTO A SUPERSONIC CROSS-FLOW

Supervisor: DR. BEN THORNBER

AUGUST 2011

This thesis is submitted in partial fulfilment of the requirements for the degree of MSc

ABSTRACT

Jet injected in a supersonic cross-flow (JISC) is a very important problem in fluid dynamics because of its applicability to scramjet combustion chamber, thrust vector control of rocket nozzles and cooling of nozzle walls. Since, combustion process has very short residence time, experimental investigation becomes difficult. Advanced turbulence modelling like DNS, LES, ILES, hybrid RANS-LES becomes computationally expensive. Thus for industrial investigation, RANS modelling becomes a very useful tool to study the flow features, flow behaviour and mixing phenomena. This thesis focuses on an under-expanded sonic jet in a supersonic cross-flow with Mach number = 1.6. It investigates two cases. The first one investigates the accuracy of four RANS models to the JISC case with jet-to-cross-flow momentum = 1.7 and flow interaction of air and air. The second one investigates the flow with jet-to-cross-flow momentum = 0.3 and non-reacting flow interaction of air (cross-flow) and hydrogen (jet). Since, supersonic turbulent boundary layer (STBL) is very important for this flow physics, inlet Mach number profile borrowed from experimental data is input at the inflow boundary. This thesis details flow features, counter rotating vortices, Mach contours, velocity profile, TKE, passive scalar, pressure distribution, jet penetration and jet mixing at different locations from upstream to downstream of the flow. The results for first case are compared to ILES and experiment with similar case setup. The investigation shows that RANS models fail to correctly predict the lambda shock position and corresponding separation zone size. However, the results downstream of jet injection are very competitive with ILES. Finally, the realizable k-ϵ model comes out to be the best RANS model for this type of flow.

Keywords:

Scramjet combustion chamber, flow features, mixing phenomena, jet-to-cross-flow momentum flux ratio, supersonic turbulent boundary layer, lambda shock position, separation zone, realizable k-ϵ

ACKNOWLEDGEMENTS

First of all, I would like to express my gratitude to my supervisor Dr. Ben Thornber, who motivated me and provided guidance at all times throughout the project. I would like to thank Dr. Zeeshan Rana, who led me on the right path and provided advice and guidance constantly. This project would not have been successful without both of them.

I would like to thank Dr. Evgeniy Shapiro, my course director, who has been of great support throughout the year. Also, I would like to thank Dr. Nikolas Asproulis and Dr. Vladimir Titarev, who have been my tutors in CFD course. I feel fortunate to be involved with them in the CFD course in Cranfield University.

Finally, I would like to dedicate this thesis to my parents for their support throughout my life.

TABLE OF CONTENTS

LIST OF FIGURES

LIST OF TABLES

NOTATIONS

J	Jet-to-cross-flow momentum flux ratio
M	Mach number
p	Pressure
T	Temperature
R	Gas constant
D	Diameter of the jet-hole
H_{mid}	Height of mid-point of Mach disk
U_{inf}	Average cross-flow velocity
V_{inf}	Average wall normal velocity
P_{inf}	Average pressure
y^+	Non-dimensional wall distance
Re	Reynolds number
μ_t	Turbulent dynamic viscosity
kPa	Kilopascal
K	Kelvin

GREEK SYMBOLS

γ	Specific heat ratio
ρ	Density
ϵ	Turbulent kinetic energy dissipation
ω	Specific dissipation rate

SUBSCRIPTS

j	conditions at jet exit
c	cross-flow conditions

ACRONYMS

JISC	Jet Injected in a Supersonic Cross-flow
CFD	Computational Fluid Dynamics
DNS	Direct Numerical Simulation
LES	Large Eddy Simulation
ILES	Implicit Large Eddy Simulation
RANS	Reynolds Averaged Navier-Stokes
RKE	Realizable k-ϵ
NPR	Nozzle Pressure Ratio
DLR	German Aerospace Centre
STBL	Supersonic Turbulent Boundary Layer
CVP	Counter-rotating Vortex Pair
CRV	Counter-Rotating Vortices
TCRV	Trailing Counter-Rotating Vortices
SA	Spalart Allmaras
RSM	Reynolds Stress Model
SST	Shear Stress Transport
TKE	Turbulent Kinetic Energy

Chapter 1: Introduction

1.1 Motivation

Under-expanded sonic jet injected into a supersonic cross-flow is a complex flow phenomenon in fluid dynamics. Due to variety of flow features like separation zone, recirculation zone, bow shock, lambda shock, barrel shock, reflected shock, vortical structures, the flow is complex but important in the study of compressible flows. The injection of under-expanded sonic jet in a supersonic turbulent flow is challenging field with applications to areas of thrust vector control of rocket nozzles, active flow control in cavities, nozzle wall cooling and scramjet combustors. The topic of interest for this project is the study of the flow in combustor chamber where the oxidizer (air) moving in with supersonic speed is mixed with the fuel (jet) injected to the chamber at sonic speed. Fuel injection, penetration and mixing are important factors in design of supersonic combustors that requires understanding of the flow physics.

The sonic under-expanded injection enhances mixing. The efficient mixing of the fuel and oxidiser improves results like maximum thrust from the air breathing propulsion systems. Unfortunately, mixing phenomena of the flow are extremely difficult to visualise because of the extreme conditions and the short residence time of the air inside the chamber. Also, advanced turbulence modelling like DNS, LES, ILES, and hybrid LES-RANS would be computationally very expensive and not very suitable for industrial investigations. Thus, numerical analysis is performed by the RANS turbulence modelling and focussed on the flow behaviour at Scramjet combustion chamber with aspects like turbulent boundary layer for the free stream supersonic flow, Mach number contours, velocity profiles at different locations, counter rotating vortices, pressure distribution on the plate and turbulent kinetic energy in the downstream flow field.

The thesis builds up from the earlier work on the standard JISC case (J = 1.7) for Mach number = 1.6. The flow conditions were investigated experimentally by

1

Santiago and Dutton [1]; using classical LES by Kawai and Lele [2]; using ILES by Rana, Thornber and Drikakis [3] and hybrid RANS-LES by Higgins and Schimdt [4]. The present works extends to investigating accuracy of the prediction of flow features by RANS turbulence models.

The second part of the thesis is based upon the Hyshot-II case. Hyshot-II is a project launched in 2002 to investigate and develop scramjet technology that deals with Mach number =7.8 at very high altitudes of 23-35kms. It was initiated by University of Queensland Australia and further experimental and CFD investigations are continuing at various institutions. In particular, this part of thesis refers to the ILES investigation done by Rana, Thornber and Drikakis [5], although it uses different cross-flow Mach number of 2.4; jet-hole diameter of 2mm and different computational domain. The present thesis borrows only the jet-to-cross-flow momentum flux ratio and cold hydrogen injection setup from Hyshot-II case and investigates the flow structures and mixing phenomena using RANS models.

1.2 Thesis layout

Chapter 2 includes the general flow features of the JISC case. It discusses the effect on the flow due to various parameters. It tracks the previous work on this standard JISC case with Mach number = 1.6. Chapter 3 discusses the governing equations, need for turbulence modelling and turbulence models used. Chapter 4 discusses the geometry setup, grid generation and applied boundary conditions. Chapter 5 discusses the results for the standard JISC case with jet-to-cross-flow momentum flux ratio (J) of 1.7. The discussion is divided into qualitative and quantitative analysis which details the flow behaviour and compares with experiment and ILES at different locations. Chapter 6 discusses the results for JISC case with jet-to-cross-flow momentum flux ratio (J) of 0.3 (derived from Hyshot-II case). The final chapters include the conclusions and the recommended future work. Finally, references and appendices are attached at the end.

Chapter 2: Literature Review

2.1 JISC Flow Physics

The major domination of the flow field is due to the vortical structures coupled with the shock formations. As shown in figure 2-1, the shock formations were observed to be of three types: barrel shock, bow shock and separation induced shock called the Lambda shock. A concave indentation in the leeward side and folding of windward side of the barrel shock are unique features of barrel shock. The concave indentation is due to the reflection of shock on the solid surface resulting in lower local pressure. The folding in the windward side of the barrel shock is due to the inner reflection line caused by the asymmetry in back-pressure. The presence of shock induces steep pressure gradients resulting six strong primary vortical structures [6]. They are as follows:

- Horseshoe vortex – 1
- Upper trailing vortex - 1
- Trailing vortices in separation region back of bow shock -2
- Trailing vortices resulting one rotational motion -2

The concave indentation in the leeward side of barrel shock and the trailing vortices result into the low pressure region at the back of the injector. The mixing mechanism is found to be governed by the trailing vortices.

2.1.1 Main Flow features

The incoming turbulent supersonic flow is obstructed by the inclined barrel shock formed due to the under-expanded sonic jet. Because of this highly under expanded sonic jet, the barrel shock ends in a Mach disk. The obstruction of the flow creates a bow shock in front of the barrel shock generating a high pressure region as seen in figure 2-2. Flow separation occurs because of this adverse pressure gradient present. Also the back pressure associated with this problem is not uniform and the free stream loses its axis symmetry.

5
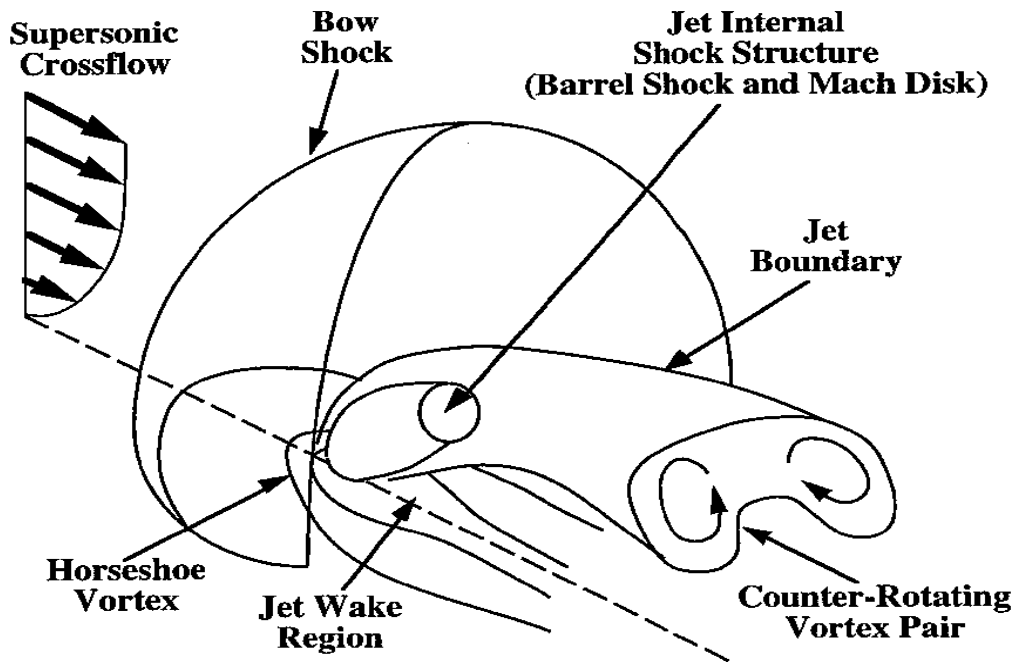
Figure 2-1 Schematic of transverse jet injected into supersonic cross-flow: 3D averaged flow features [7]
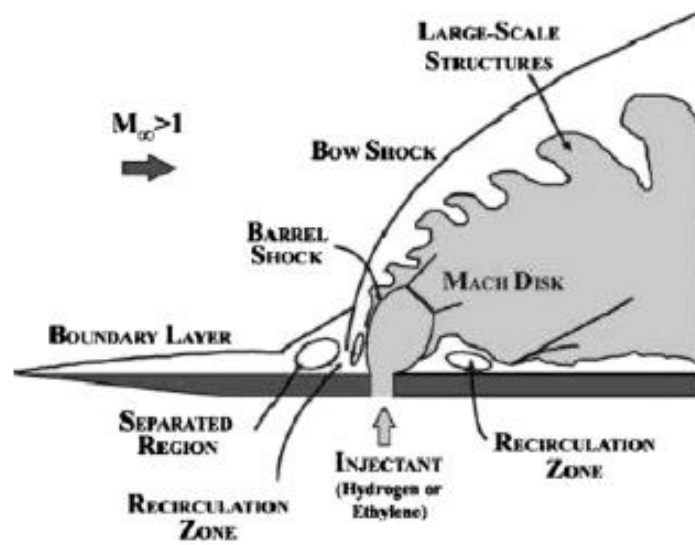
Figure 2-2 Schematic of transverse jet injected into supersonic cross-flow: 2D, instantaneous flow features [7]

6

Just in front of the bow shock, the boundary layer separates creating a small separation region and a lambda shock that interacts with bow shock. The flow decelerates in the recirculation zone just ahead of the jet and conversely, accelerates rapidly inside the jet plume towards the Mach disk. Thus, the maximum Mach number is present at the top edge of the jet plume.

The turbulent inflow has a major influence on the upstream flow properties and almost no influence on downstream flow properties [8]. The momentum of the mainstream flow affects the size and deflection of the small separation region.

As seen in figure 2-3, large expansion fans are present inside the barrel shock. The expansion shocks are bounded by the recompression shock that ends with Mack disk. The Mach disk reduces the velocity of flow to subsonic and forms a slip surface with the incoming supersonic flow. The two flows eventually mix downstream and results a highly turbulent flow. Due to the flow interactions at the windward side of the injector, a sonic recompression line is formed and not at the leeward side due to the solid wall. Triple point is identified at the intersection of downwind barrel shock and the Mach disk. The reflected shock arises from this triple point. This reflected shock impinges on the solid surface inducing a thickening of the boundary layer [9]. The maximum turbulent fluctuation velocities appear at this region very near to the solid bottom wall [10].
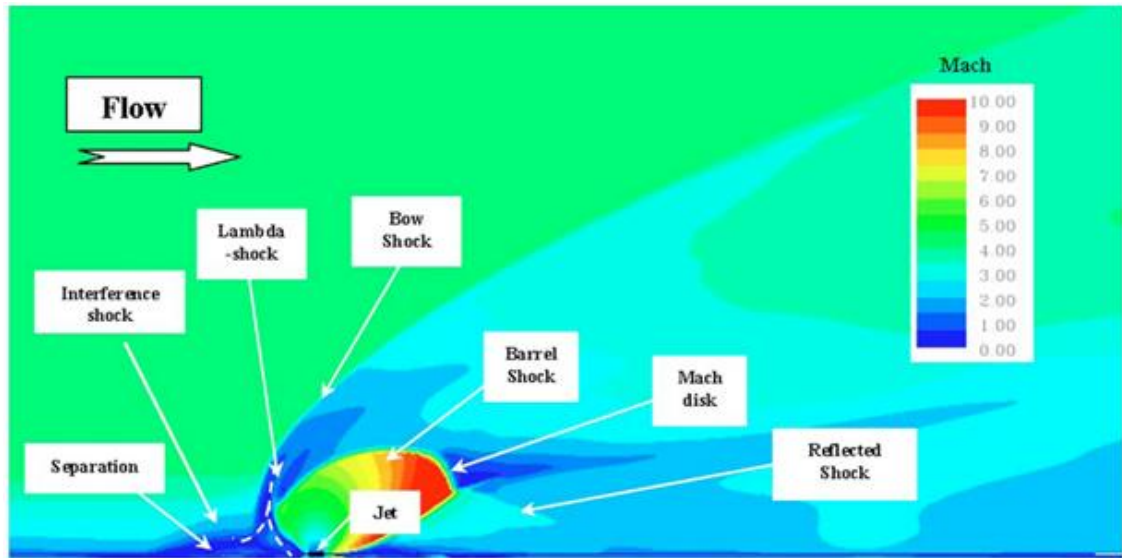
(a)
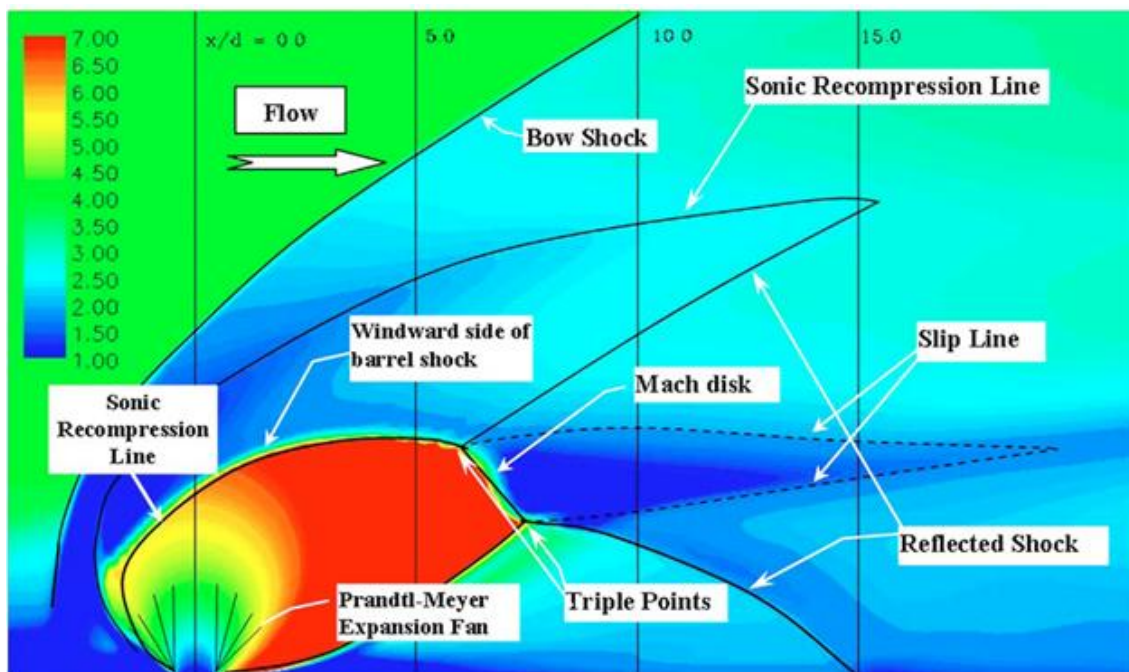
(b)

Figure 2-3 Under-expanded, sonic, circular jet injected into supersonic cross-flow (M=4) with pressure ratio of 532: Mach contours on the plane of symmetry: (a) entire domain (b) enlarged section around the jet injector [6]

2.2 Vortical Structures of JISC

2.2.1 Generation of Counter-rotating Vortex Pair (CVP)

(a)

(b)
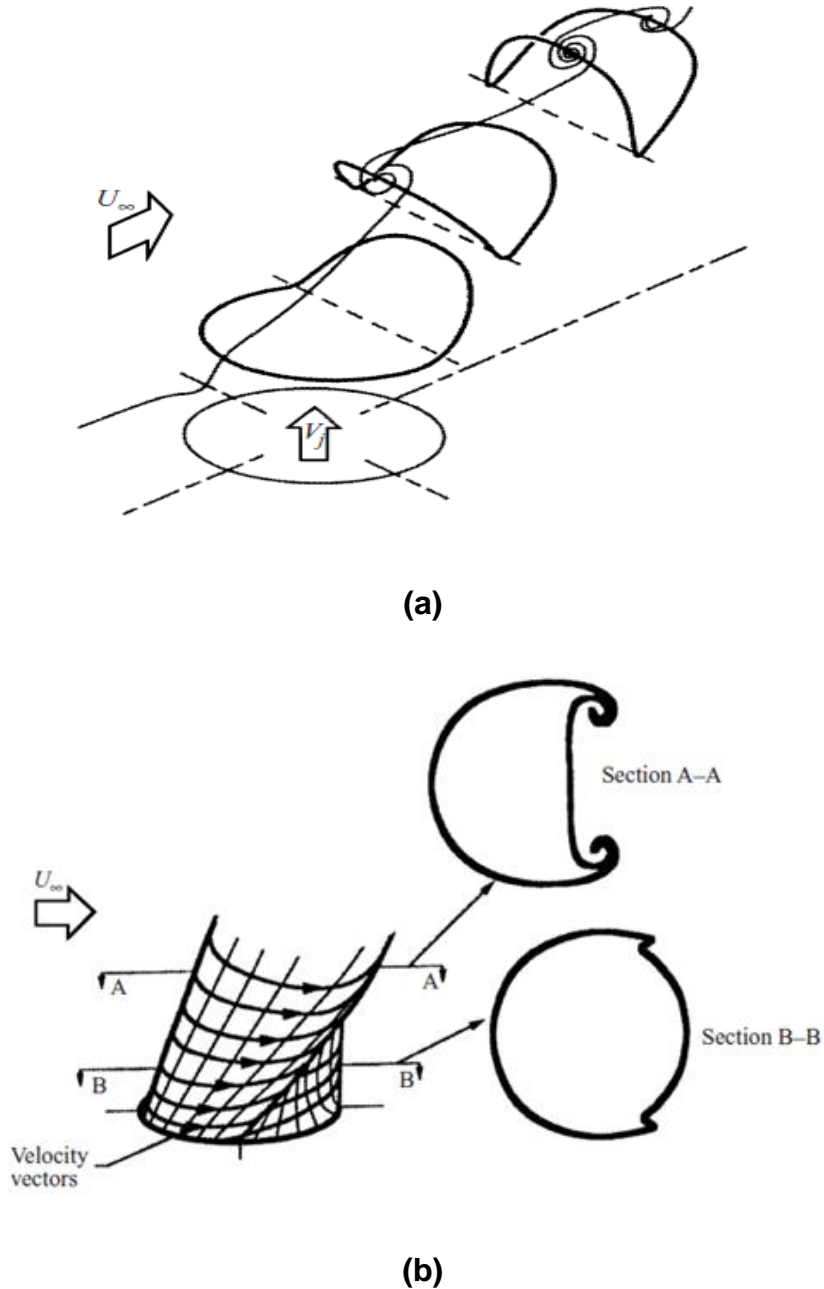
Figure 2-4 Shear layer evolution: (a) Isometric view of the vortex rings and the process of tilting and folding while convecting downstream (b) Schematic of the shear layer vorticity and the folding of cylindrical vortex sheet [11]

CVP is a global flow feature because it arises from the impulse of the jet and is convected downstream by the cross flow as seen in figure 2-4a. The rolling of periodic vortex rings arise from the jet-hole and the cross-flow reorients the vortices of the shear layer so that the cylindrical vortex sheet folds as presented in figure 2-4b. Due to this combined process, the upper part of the ring tilts with the jet's mean curvature and the lower part with the direction of jet which results in circulation of the CVP.

2.2.2 Types of CVP

The interaction of flows leads to five pairs of counter- rotating vortices presented in figure 2-5. Four pairs are formed in the recirculation zone and the remaining pair at the region of Mach disk. When passing through the Mack disk, the jet fluid is recompressed aiding to the formation of kidney- shaped vortex. Different types of CVP with their properties are as follows:

- Horse shoe vortex – moves horizontally away from the centreline, isolated from other vortex systems
- Trailing upper vortex – moves vertically away from the centre line, isolated from other vortex systems
- Longitudinal vortices – formed at the recirculation zone and gets stronger downstream
- Trailing lower vortices – formed at the recirculation zone, remains close to the surface and in the symmetry plane
- Kidney shaped counter-rotating vortices – formed downstream of the jet plume, plays a major role in mixing process

The trailing edge at the jet exit flattens to deform the circular cross section of the jet to kidney shaped. Along the leeward side, the counter rotating vortices are displaced from the centre streamline. Thus, the peak production of TKE is below the centreline at the far field. Also, peak production of TKE is seen in the leading edge of jet due to the jet and cross flow interaction. Due to these steep gradients and budget profiles at the jet exit, the RANS computation becomes difficult. [12]
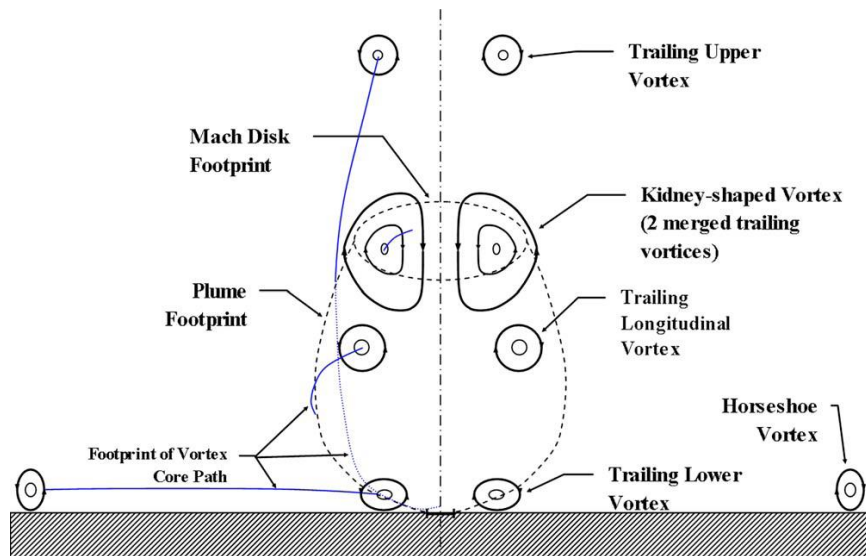
(a)
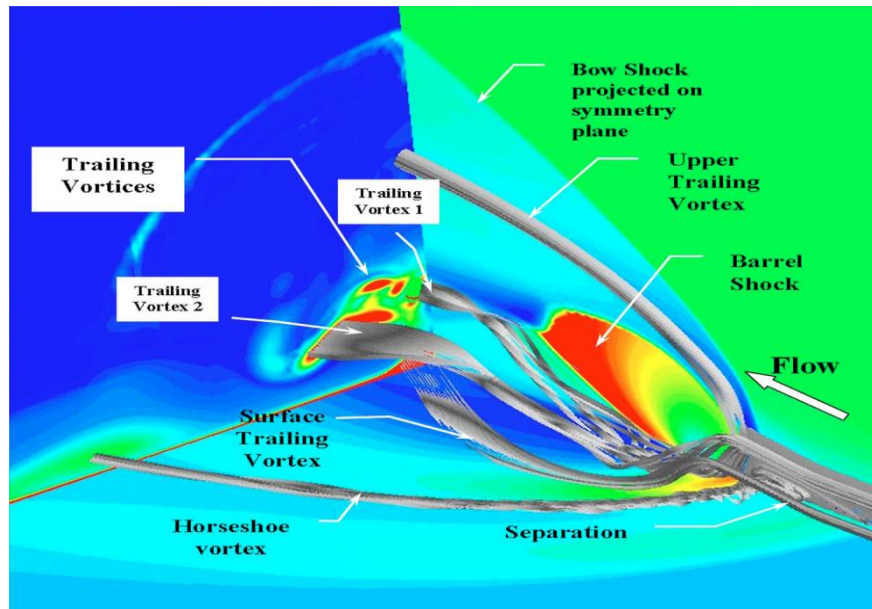
(b)

Figure 2-5 a) Transverse section at the aft of the barrel shock: depicting different CVP (b) Under-expanded sonic circular jet injected into supersonic cross-flow (M=4) with pressure ratio of 532: Isometric view for JISC with streamlines and main vortical structures. Symmetry plane - Mach contours: Surface plane - C_p contour: Cross plane - vorticity contour [6]

2.3 Computational and Experimental studies on JISC

2.3.1 Experimental Investigation

Santiago and Dutton [1] performed the experimental investigation of the JISC with a free stream flow of M = 1.6; Reynolds number (free-stream) = 58.8 * 10^6 m^{-1}; Reynolds number (jet) = 1.11 * $10^{4;}$ jet-to-cross-flow momentum flux ratio =1.7. The jet injected was a single, under-expanded, sonic, transverse and round jet. The experimental techniques used were two-component frequency shifted LDV and Schlieren / Shadowgraphy photography. It was used to measure the three main velocity components, turbulent velocity, TKE and Reynolds stresses and study the complex flow structures formed. The paper depicted that the recirculation zone, 1.5 jet diameters upstream and 0.5 jet diameters high from the wall, could be the possible ignition zone for reacting fluids. The leeward side of jet plume has low transverse velocity gradient and low Reynolds stress. Here, the fluid gets trapped because of counter rotating vortices and responsible for mixing mechanism. The jet loses momentum flux at the Mach disk and turns downstream. Unsteadiness of the flow is small on the windward side of the barrel shock at the recirculation region which enhances mixing in supersonic combustors. At three jet diameters downstream, the size of the jet plume increases transversely which emphasizes on the required configuration of supersonic combustors. The downstream velocity field of jet plume is dominated by kidney shaped counter rotating vortices. Rapid mixing is expected at areas of high Reynolds stress (shear layers). For better numerical modelling, small regions of high Reynolds shear stresses, high TKE must be carefully considered for grid size and turbulence models implemented.

2.3.2 Flow Visualisation

Van Lerberghe, Santiago, Dutton and Lutch [13] performed experimental investigation to study the mixing characteristics of the jet fluids. The flow visualisation (a side view of the barrel shock and side and end view cross section of the plume) was done by shadowgraphy and planar laser-induced fluorescence using acetone. Large scale turbulent structures responsible for

mixing were studied using instantaneous and statistical images. The wake region in the leeward region of the barrel shock and below the centreline of jet was found to have significant mixing. Also, the counter rotating vortices were found to be largely responsible for the scalar mixing process. The level of mixing of fluids was highest in the wake region below the jet centreline. Improvements in mixing levels were noticed as the downstream distance from Mach disk increased. Counter rotating stream-wise vortices make a key contribution to the mixing process as the jet fluid and the cross flow fluid are trapped to the wake region by these vortices. The penetration of the jet in the cross flow is due to the existing momentum of the jet. This gives rise to large turbulent structures that play a major role in mixing process. The counter rotating stream-wise vortices are asymmetric just after the Mach disk and turn symmetric downstream. The asymmetric nature is due to disturbances in the barrel shock region.

2.3.3 Numerical Investigation using Large Eddy Simulation (LES)

Kawai and Lele [2] used LES with high order compact differencing scheme and localised artificial diffusivity scheme (discontinuity capturing) for the study of JISC and jet mixing physics. The grid convergence test was also performed with reasonable improved results. The LES simulation reported similar flow structures with rich data on flow physics. It focussed on the jet mixing physics and the vortices (U-shaped counter rotating vortices sideways from symmetry plane and counter rotating above U-shaped vortices around symmetry plane). The breaking down of large scales longitudinal vortices in the turbulent region signified the role of eddy structures for fluid mixing. Pressure fluctuations in the upstream recirculation region; the unsteady dynamics of deformation of the barrel shock and bow shock and vortex formations were responsible for the upstream jet fluid mixing. Also, the paper noted that the turbulent free-stream enhances the mixing process better than the laminar free-stream.

2.3.4 Numerical Investigation using Implicit Large Eddy Simulation (ILES)
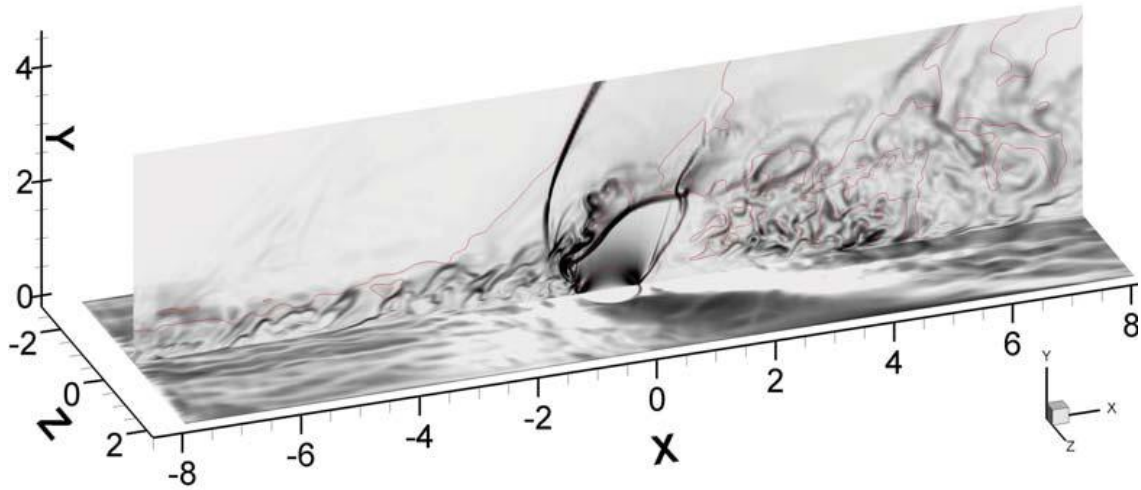
Figure 2-6 View of JISC using ILES with digital filters: Horizontal plane- Velocity contours: Vertical plane- density gradient contours: Red line- position of Mach number=1.5 [3]

Rana, Thornber and Drikakis [3] used a Godunov type ILES method to study a jet injected in supersonic cross-flow. The algorithm employed a fifth order method in space and second order method in time. The turbulent inflow data generator was produced using a digital filter. The free stream flow had M = 1.6 and the sonic jet injection penetrated and mixed with the flow which is seen in figure 2-6. A grid convergence test was performed and the flow properties were analysed. Mixing was enhanced by the Kelvin–Helmholtz instability in the jet shear layer. The results were compared to experimental and classical LES data. The results were pretty similar to the experiment and more accurate than LES. Also, the ILES computations were 45 times less expensive than the LES. The paper also presented that complicated flows involving discontinuities were captured accurately and fast using high resolution method. The mixing of two fluids was enhanced by incoming supersonic turbulent boundary layer. Kelvin Helmholtz instabilities generated on jet shear layer were responsible for better mixing of fluids. A rapid mixing process starts in the thick shear layer of jet

plume. The combustion process would be ignited initially by the high temperature of jet fluid captured in the recirculation zone upstream of jet plume.

2.3.5 Numerical Investigation using Hybrid LES-RANS

The same setup has been investigated by Peterson and Candler [14] using hybrid LES-RANS. It used an unstructured finite volume solver which was able to capture the unsteadiness in the jet plume. The investigation was repeated by Higgins and Schmidt [4], improved the investigation by the use of a synthetic inflow boundary layer. They simulated injection with finite volume structured mesh Navier - Stokes code. The flow structures like Mach disk, bow shock, lambda shock, barrel shock, large scale unsteady vortical structures were similarly depicted as the experiment by Santiago and Dutton [1]. It also predicted a 'necklace' vortex generated from the recirculation region that causes separation of the incoming turbulent boundary layer. The results of TKE and Reynolds stresses were reasonably good compared to experiment results. The hybrid LES – RANS simulation under-predicted the peak values may be due to the poor grid resolution.

2.4 Study of Jets

2.4.1 Axis-symmetric Jets

The circular convergent jets are classified into three according to the nozzle pressure ratio (NPR) [15]:

- Subsonic jet
- Under-expanded free jet
- Highly under-expanded free jet

Basically, the jet consists of a core where the velocity is constant, no viscous mixing occurs and surrounded by a mixing region. Far downstream, the core diminishes. However, the mixing region keeps spreading because of the decay of velocity to conserve angular momentum. The jet with NPR between the

ranges 1-1.893 is subsonic jet (Figure 2-7). Nozzle pressure ratio is defined as the ratio of total to static pressure of the nozzle.

For the NPR range 2-4 falls in the under expanded jets (Figure 2-8). At this range, the core consists of 'shock diamonds' or 'cells' where the numerous oblique shocks intersect. In this case, the inward diffusion of the mixing region dissipates the shock core and finally achieves a subsonic characteristic downstream.

For highly under-expanded free jet (Figure 2-9), the NPR is greater than 4. In this range, the formation of Mach disk is observed. The diffusion is lesser in this case, extending the core to long distances.

Exit Mach number and the pressure ratio across nozzle define the location of Mach disk. The angle of divergence and viscous effects has negligible influence on the position of Mach disk. Shock formation for under-expanded jets is similar to the flows through nozzles due to these reasons. Adding to these dependencies, the location of Mach disk could be calculated without detailed study of shock structures. Adamson and Nicholls [16] provided the method to calculate the position of the first Mach disk for the highly under-expanded nozzles. The position of first shock is calculated by finding the point where the static pressure is brought to atmospheric pressure due to the existence of shock. This means that the nozzle exhausts to atmospheric pressure through shock at exit.

Chizhikov [17] studied the gas flow rate across the Mach disk. He concluded that the maximum gas flow rate through Mach disk in an under-expanded jet means the outflow regime is sonic. In the jet, the redistribution of total energy is less than 10% because of the irreversibility of the process through flows with range of Mach numbers and inefficiency ratio (ratio of nozzle exit's static pressure to surrounding pressure). The gas flow rate is an asymptotic function of the inefficiency ratio.
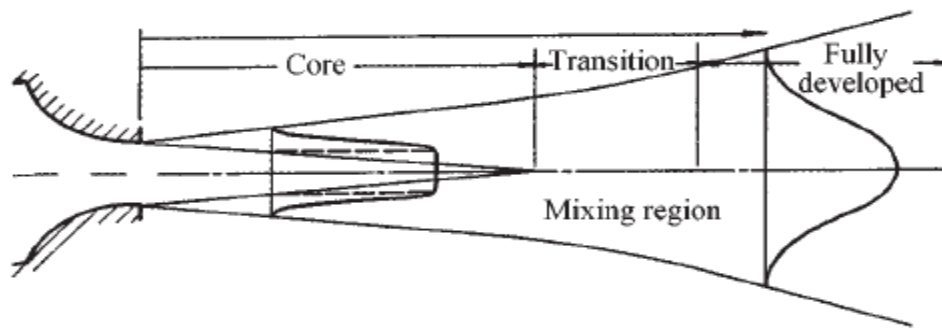
Figure 2-7 Subsonic free jet [15]
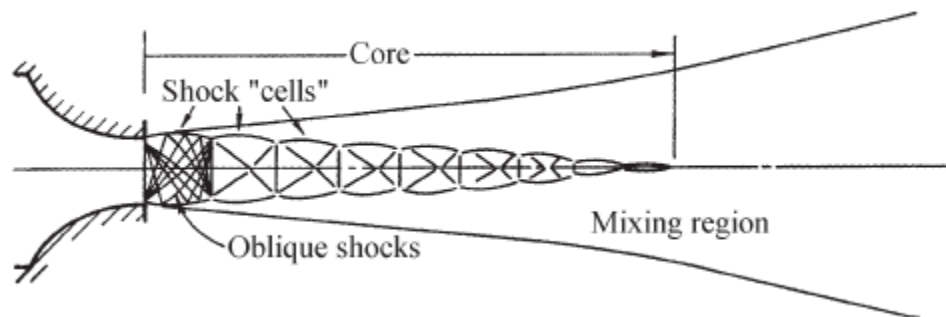
Figure 2-8 Under-expanded free jet [15]
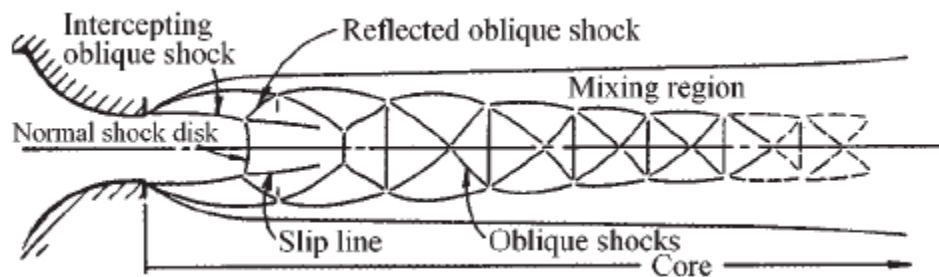
Figure 2-9 Highly under-expanded free jet [15]

The Mach disk is a distinctly observable discontinuity where thermodynamic and kinematic quantities vary significantly. Across the Mach disk, the total pressure drops whereas static pressure increases; static temperature increases whereas total temperature is preserved; flow reaches subsonic velocity; entropy increases and total enthalpy is conserved.

2.4.2 Different types of jet injection

The configuration of jet injection system can also be classified as follows [18]:

- Tangential slot injection (Figure 2-10a)
- Porous wall injector (Figure 2-10b)
- Transverse jet injection (figure 2-10c)

AIR

BOUNDARY LAYER

FUEL

SOLID WALL

(a)

AIR

BOUNDARY LAYER

FUEL

POROUS WALL

(b)

AIR

FUEL

BOUNDARY LAYER

SOLID WALL
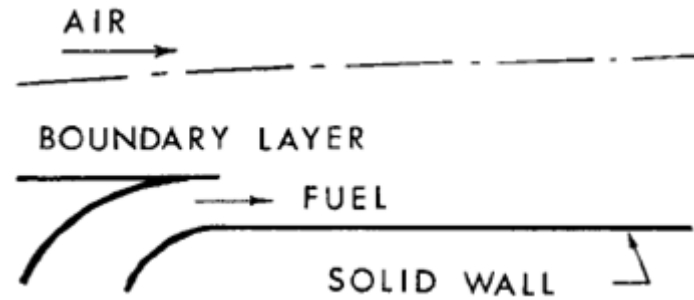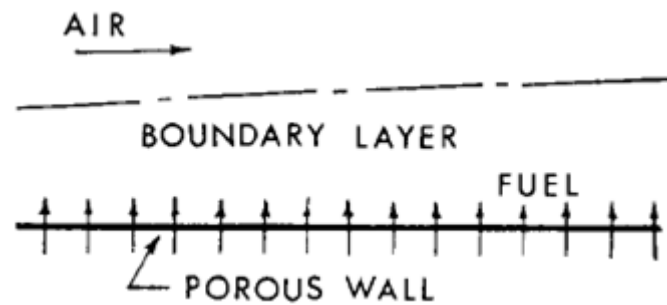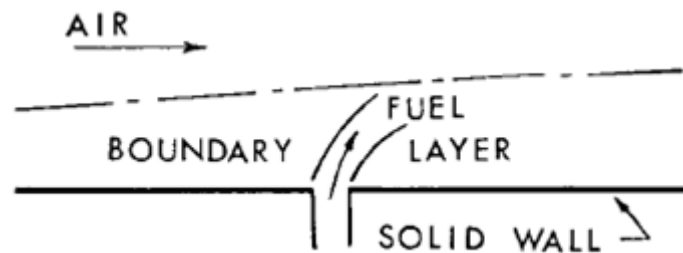
(c)

Figure 2-10 Configurations for the injection types (a) Slot injection (b) Distributed injection (c) Transverse injection [15]

The classification of the injection system that matches the discussion of the thesis is transverse jet injection. Transverse jet injection has an important aspect called the penetration of jet into cross-flow that depends on the jet-to-cross-flow momentum flux ratio which is defined by equation 2-1.

Jet-to-cross-flow momentum flux ratio [19], $J = \frac{\rho_j V_j^2}{\rho_c V_c^2} = \frac{\gamma_j P_j M_j^2}{\gamma_c P_c M_c^2}$ **(2-1)**

Here, ρ, V, γ, P, M are density, velocity, specific heat ratio, pressure and Mach number respectively and subscripts j and ∞ represent the jet and crossflow respectively. The jet momentum flux is dependent on the total pressure of the jet. The increment in total pressure of jet improves the penetration of the jet into the cross-flow. However, the interaction of flows could minimise the penetration. The initial formation of the jet can be explained by its exit static pressure to the surrounding. The Mach disk formation is also described by the process of a high pressure jet exiting to a low pressure medium. Also, the location of the Mach disk is determined by the ratio of specific heats and the ratio of static pressure to the back pressure. Another important property to be noticed is that the fuel penetration doesn't much depend on the injector shape for a given mass flow rate [18].

2.4.3 Influence of jet configuration

Experiments were performed by Kovar and Schulein [20] for free-stream with Mach number, M= 5; Reynolds number Re = 25 * 10^6 (based on length of flat plate) and jet pressure ratio = 100. Investigations were performed for single jet, four jets mounted in line and four jets mounted side by side.

Also, the test case was investigated numerically using TAU-code. TAU-code is developed by German Aerospace Centre (DLR) which uses Reynolds Averaging hybrid Navier-Stokes for calculating the three-dimensional compressible flows. Although the flow-fields are similar for the numerical (TAU-code) and experimental investigations, the separation and reattachment lines have shifted. The separation line shifts upstream for the one jet configuration as in figure 2-11a.

For the case of four jets mounted in-line as shown in figure 2-11b, the numerical simulation results are improved compared to one jet configuration. The separation and reattachment lines are much closer to the experimental results. At far lateral distances, a little shift of the lines is seen.

For the case of four jets mounted side by side as shown in figure 2-11c, the results are worse. Due to the complex jet- main flow interaction, a wide primary separation is observed and does not improve downstream.
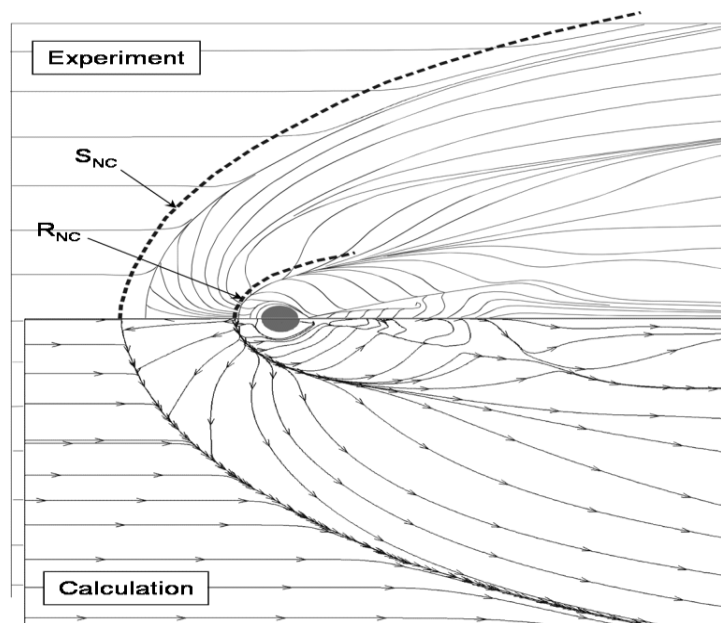
(a)
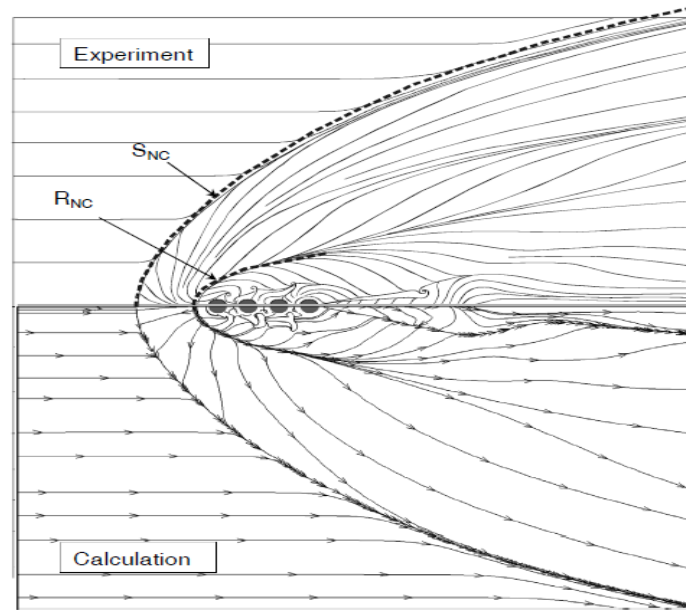
(b)
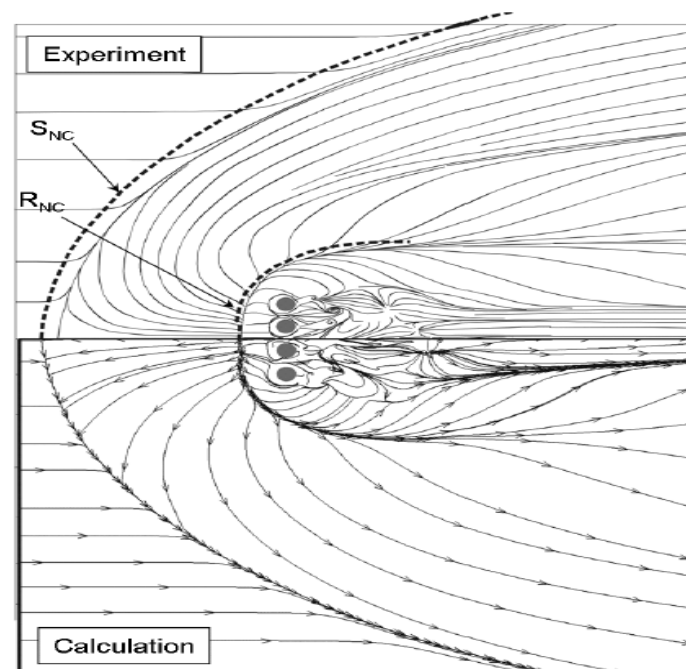
(c)

Figure 2-11 Representation of experimental (upper) and numerical (lower) wall streamlines. The dotted lines in the upper section is the mirrored line of the lower streamlines (a) single jet (b) four jets placed side- by-side (c) four jets in-line [20]

2.4.4 Influence due to shape of the jet-hole

According to Fric and Roshk's [21] experimental investigation (smoke wire visualisation technique) in the region of injector exit, velocity of the jet fluid tangent to the fluid interface had higher velocity than the free stream fluid. This was for the low speed cross-flow. These convection characteristics of vortices and near field behaviour could be influenced by geometry of injector as presented by Gruber, Nejad, Chen and Dutton [7].

Elliptic injectors tend to have asymmetric vortices due to asymmetric instability, and a shallow convection angle and skewed convection velocity towards the free-stream velocity affecting the near-field behaviour. The spreading characteristics of elliptic injectors exhibit structural difference to the circular jets, as investigated by Gruber, Nejad and Dutton [22]. Spreading of the jet happens differently on minor and major axes and after some time the minor axis plane could overtake the spreading phenomena (axis-switch phenomena). The strength of the bow shock formed is also comparatively weaker than the circular jets.

2.5 Parameters effecting flow field of JISC

2.5.1 Compressibility effects

Statistical data like standard deviation, 2D spatial correlations and characteristic information like large scale mixing and jet spreading and penetration were used as tools to investigate the compressibility effects. Gruber, Nejad, Chen and Dutton [23] performed experiments using planar Rayleigh/ Mie scattering from silicon dioxide particles seeded into cross-flow. The free-stream conditions were Mach number, M = 1.98, Reynolds number, Re = 3.9 $*10^7$ with jet-to-cross-flow momentum flux ratio of 2.9. Injected gases were air and helium. They showed that the transverse penetration of the jet into the cross-flow is not affected much by the molecular weight of the injecting jet. However, it made a difference to the

compressibility level and affected the large scale structures in the shear layer. The mixing and entrainment of the jet and cross-flow was also influenced. Higher compressibility maintained coherent large scale structures over a longer spatial range whereas the low compressibility enhanced the rapid breaking of the large eddies. The fluctuations of the mixing layer present near the jet edge interposed deeply into the jet fluid. This showed that a low compressibility fluid has potential to mix more effectively.

The convection of the large eddies are dependent on the compressibility of the fluid. Increased compressibility produced vortices with larger convection velocity and the large vortices convected with free stream velocity at far downstream [7].

Compressibility and turbulence level at the jet exits influence the near-field region of under-expanded jets. For a convective Mach number > 0.5, the mixing rates decrease due to compressibility effects. Conversely, mixing rates are increased by high turbulence levels. The former effect increases and the later effect decrease the length of the core of under-expanded jets. [24]

2.5.2 Jet-to-cross-flow momentum flux ratio effect

Wanga and Lub [25] studied the effects of the jet-to-momentum ratio on the flow structures, frequency behaviours and turbulent characters of the flow. Spectral analysis showed that the unsteadiness of the bow shock, barrel shock and jet shear layer had similar frequency and the evolution of horseshoe vortex had relatively lesser frequency. Identification of the wrapping of the horseshoe vortex in the windward side of jet and a small secondary vortex between the jet and the horseshoe vortex were also reported. Increasing jet-to-momentum ratio resulted in the increment of the following important characteristics (as seen in figure 2-12a, 2-12b):

- Strength of the bow shock
- Size of the barrel shock and the Mach disk
- Jet penetration into the cross-flow which enhances the mixing process
- Jet shear layer vortices which strengthens the mixing process
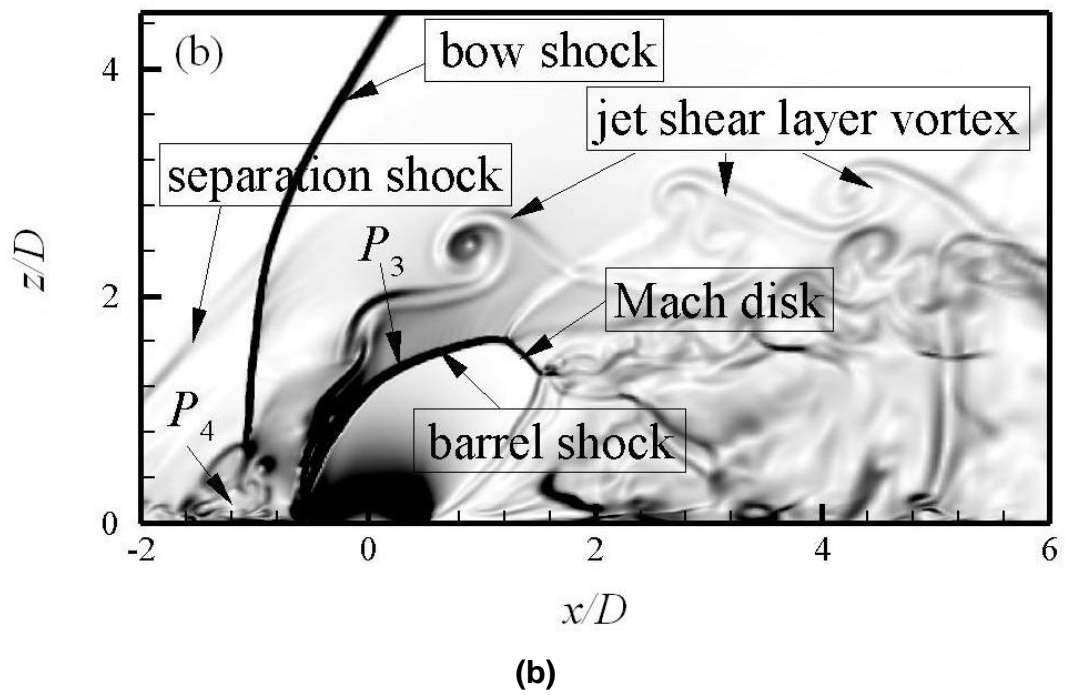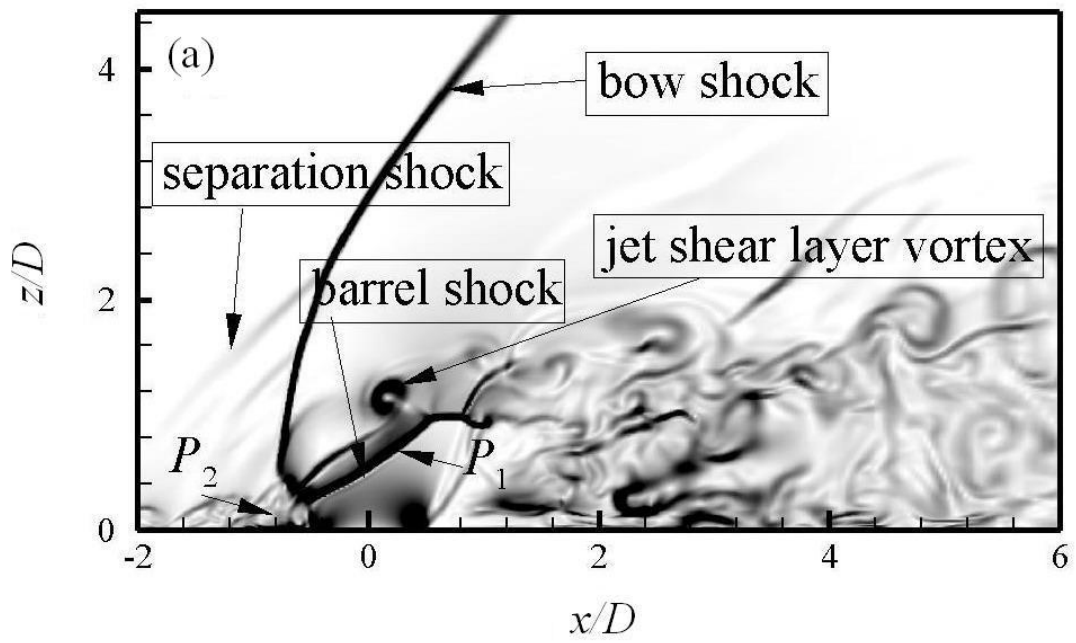
Figure 2-12 Instantaneous numerical visualization of contours of density gradients (a) For J=1.2 (b) For J=2.2 [25]

2.5.3 Mixing and penetration of jet

Mixing effectiveness is the percent of ideal energy exchanged jet and cross flow. The main operating variable responsible for the penetration and mixing of the jet is the jet-to-cross-flow momentum flux ratio and independent to the absolute momentum flux level of each fluid and the jet to main stream density ratio [19]. The mixing parameters are temperature distribution efficiency or the percent of energy exchange and pattern factor related to the distribution of exit temperature. Due to the short residence time, high penetration and mixing are difficult in supersonic combustion [26].

Mixing for the sonic jet injected in a supersonic cross-flow with M = 1.6, was studied experimentally by Van Lerberghe, Santiago, Dutton and Lutch [27]. They noted that instantaneous mixing occurred at the wake region of the barrel shock and below centreline of the jet. The jet plume and large scales structures played important role in transporting fluid across the three dimensional shear layer focussed due to the interaction of jet and cross-flow. The counter-rotating vortices in the stream-wise direction carried the jet to wake region and the cross-flow fluid to the jet, enhancing the scalar mixing. The mixing improves downstream from the Mach disk.

Cohen, Coulter and Egan [28] formulated the jet penetration height into cross flow using the non-dimensional ratio as shown in equation 2-2.

$$\frac{\mathrm{H}_{mid}}{\mathrm{D}} = \left[\frac{2\left(1+\frac{\gamma_j}{2}M_j^2\right)}{\gamma_j^2 M_j(\gamma_j+1)} \right]^{0.25} \times \left[\frac{1.25\left(1+\gamma_c\right)\gamma_c M_c^2}{(1-\gamma_c)+2\gamma_c M_c^2} \right]^{0.5} \times J \qquad \textbf{(2-2)}$$

Here, H_{mid} = height of midpoint of Mach disk

    D = diameter of jet-hole

    J = jet to cross flow momentum flux ratio

    γ = specific heat ratio

    M = Mach number

Amano and Sun [29] investigated the dependency of total pressure ratio of jet to free stream, separation length, and penetration height. The separation length and penetration height are defined in figure 2-13. It was concluded that the major influence on the jet is due to the pressure ratio of jet to free stream. The investigation showed that separation length and penetration height increase linearly with the total pressure ratio as in figure 2-14.
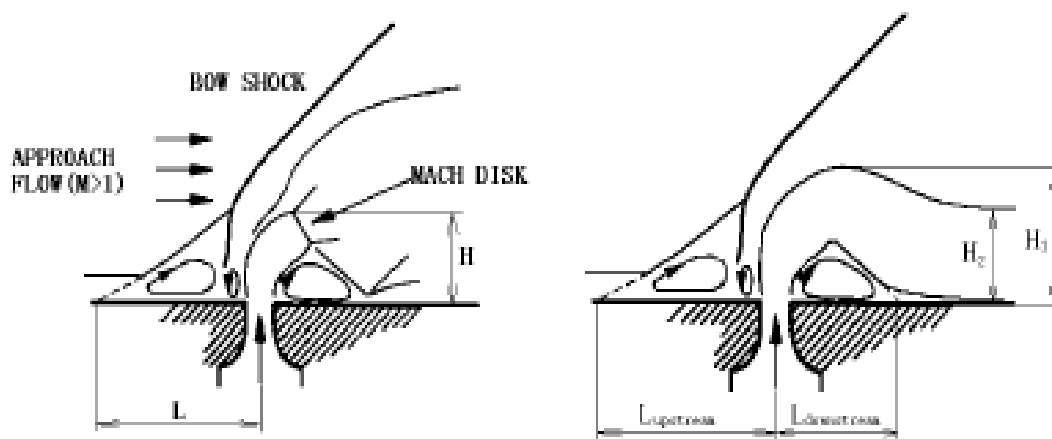
Figure 2-13 Defining separation length and penetration height [29]

Here, H_1 = highest penetration height

H_2 = height at downstream of injection

$L_{upstream}$ = upstream separation length

$L_{downstream}$ = downstream separation length
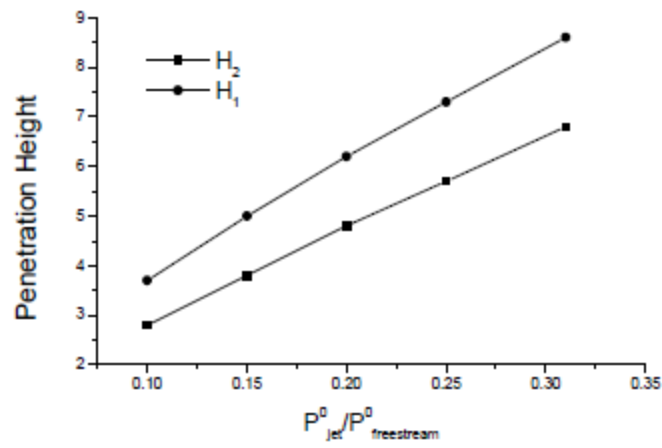
(a)
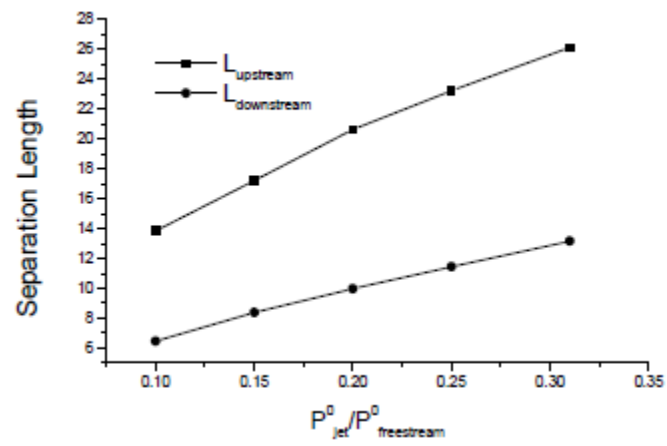
(b)

Figure 2-14 Dependency plots (a) Penetration height vs. total pressure ratio (b) Separation length vs. total pressure ratio [29]

Chapter 3: Numerical Methods

In this scientific world, all the flows are best tried to contain in mathematical equations. All fluid flows follow universal laws of mass, momentum and energy conservation. These equations are the basis for all CFD investigations. With the limitations of computer resources, these equations are simplified according to necessity. The thesis involves supersonic cross-flow interacting with jet injected through a circular hole.

3.1 Governing Equations

The universal laws have to be modified to fit the type of flow. These modified equations according to the flow type are the governing equations of the flow. For these types of flows, we need compressible Navier-Stokes equation for non-reacting gases. Equations 3-1 to 3-5 are the governing equations for the flow.

Continuity equation: $\frac{\partial \rho}{\partial t} + \nabla \cdot (\rho \boldsymbol{u}) = 0$ **(3-1)**

Momentum equations: $\frac{\partial \rho \boldsymbol{u}}{\partial t} + \nabla \cdot (\rho u \boldsymbol{u} + p\delta - \tau) = 0$ **(3-2)**

Energy equation: $\frac{\partial E}{\partial t} + \nabla \cdot [E\boldsymbol{u} + (p\delta - \tau) \cdot \boldsymbol{u} - \kappa \nabla T] = 0$ **(3-3)**

Here,

$$E = \frac{p}{\gamma - 1} + \frac{1}{2} \rho u \cdot \boldsymbol{u}$$ **(3-4)**

Passive scalar equation: $\frac{\partial \rho Y}{\partial t} + \nabla.(\rho \boldsymbol{u} Y) - \nabla(\rho D_c \nabla Y) = 0$ **(3-5)**

Ideal gas equation: $p = \rho R T$ **(3-6)**

In the above equations, ρ, $\boldsymbol{u}$, p, R, E, T, γ, δ, D_c, τ represent density, velocity vector, static pressure, gas constant, total energy, temperature, ratio of specific heats, unit tensor, diffusion coefficient for the passive scalar and viscous stress tensor respectively. For brevity, the above equations represent only *x* flow direction which could be expanded similarly for *y* and *z* flow directions.

3.2 Turbulence and RANS turbulence modelling

Turbulence is a three dimensional phenomena which is due to the instabilities at high Reynolds number. These instabilities arise due to interaction of viscous and non-inertial terms. These time-dependent motions have velocity fluctuations due to vortex stretching. The fluctuations spread to wide range of wavelengths. The large scale eddies are determined by boundary conditions of flow whereas small scale eddies are dependent on viscous forces. These velocity fluctuations induce fluctuations to the transport quantities – momentum, energy, passive scalar. The fluctuations to the transport equations make the computation very expensive. Computational expense can be reduced by averaging the equations. As in equation 3-7, Reynolds Averaging decomposes the flow variable (u) to mean (U) and fluctuating component (u'),

$$u = U + u'$$

    (3-7)

When these decomposed components are fitted to the flow variables in the Navier- Stokes equation and averaged on time, we obtain RANS equation. These RANS equations are impossible to solve because unknown Reynolds stress tensor (equation 3-8) have appeared.

Reynolds Stress Tensor, $\tau_{ij,t} = -\rho\overline{u_i'u_j'} = \begin{bmatrix} -\rho\overline{u'^2} & -\rho\overline{u'v'} & -\rho\overline{u'w'} \\ -\rho\overline{v'u'} & -\rho\overline{v'^2} & -\rho\overline{v'w'} \\ -\rho\overline{w'u'} & -\rho\overline{w'v'} & -\rho\overline{w'^2} \end{bmatrix}$ **(3-8)**

Reynolds stress tensors have six additional unknowns which are more than available four equations. So, the system of equations has to be closed which gives rise to the term called RANS turbulence modelling. For modelling of RANS equations, Boussinesq assumption is commonly used. It assumes isotropy for turbulence. It relates mean velocity gradient with unknown Reynolds stress tensor as shown in equation 3-9.

$$-\rho\overline{u_i'u_j'} = \mu_t \left(\frac{\partial \overline{u_i}}{\partial x_j} + \frac{\partial \overline{u_j}}{\partial x_i} \right) \qquad \textbf{(3-9)}$$

Alternatively, Reynolds Transport Models can be used which take each term of Reynolds stress tensor and solves transport equations. This would mean that additional five equations for 2D and seven equations for 3D have to be solved.

3.3 Spalart Allmaras (SA) turbulence model

Spalart Allmaras is a one equation model [30] which uses Boussinesq assumption to determine Reynolds stresses. This turbulent model solves just the transport equation for kinematic eddy viscosity and does not require calculating the length scale. This model is popular for aerospace applications and proves good for modelling boundary layer when adverse pressure gradients are involved. It is also expected to show good prediction for separation and reattachment in backward facing step.

However, Spalart Allmaras is inefficient for predicting spreading rates with round, planar and radial jets and when flow changes from wall bounded to shear flows. It can inaccurately predict shock induced boundary layer

31

separation for supersonic flows. Analysing the inefficiency, Spalart Allmaras model may not be regarded the most suitable for the kind of flow in the thesis.

3.3.1 Transport equation for Spalart Allmaras turbulence model

$$\frac{\partial}{\partial t}(\rho \tilde{v}) + \frac{\partial}{\partial x_i}(\rho \tilde{v} u_i)$$

$$= G_v + \frac{1}{\sigma_{\tilde{v}}} \left[\frac{\partial}{\partial x_j} \left\{ (\mu + \rho \tilde{v}) \frac{\partial \tilde{v}}{\partial x_i} \right\} + C_{b2} \rho \left(\frac{\partial \tilde{v}}{\partial x_j} \right)^2 \right] - Y_v + S_{\tilde{v}} \quad \textbf{(3-10)}$$

Here, G_v , Y_v , $\tilde{v}$ represent turbulent viscosity production, turbulent viscosity destruction and molecular kinematic viscosity. $\sigma_{\tilde{v}}$, C_{b2} are the equation constants and $S_{\tilde{v}}$ is the source term [31].

3.4 Realizable k-ϵ turbulence model

Realizable k-ϵ is a two equation model in the family of standard k-ϵ which was proposed by Shih et al. [32]. It uses a new turbulent viscosity formula and derives dissipation (ε) from equation of mean square vorticity fluctuation. This means that turbulent viscosity includes mean rotation. Due to this, Realizable k-ϵ could provide unphysical turbulent viscosities where rotating zone exist.

However this model has proved superior to standard k-ϵ in predicting spreading rates in planar jets, separation, recirculation and boundary layers under adverse pressure gradients. It performs very well for separated flows involving secondary flow and is very well suited for the type of flow in the thesis.

3.4.1 Transport equation for Realizable k-ϵ turbulence model

$$\frac{\partial}{\partial t}(\rho k) + \frac{\partial}{\partial x_j}(\rho k u_j) = \frac{\partial}{\partial x_j} \left[\left(\mu + \frac{\mu_t}{\sigma_k} \right) \frac{\partial k}{\partial x_j} \right] + G_k + G_b + \rho \varepsilon - Y_M + S_k \quad \textbf{(3-11)}$$

$$\frac{\partial}{\partial t}(\rho\epsilon) + \frac{\partial}{\partial x_j}(\rho\epsilon u_j)$$

$$= \frac{\partial}{\partial x_j}\left[\left(\mu + \frac{\mu_t}{\sigma_\epsilon}\right)\frac{\partial\epsilon}{\partial x_j}\right] + \rho C_1 S_\epsilon - \rho C_2 \frac{\epsilon^2}{k + \sqrt{v\epsilon}}$$

$$+ C_{1\epsilon}\frac{\epsilon}{k}C_{3\epsilon}G_b + S_\epsilon \qquad\qquad \textbf{(3-12)}$$

Here,

$$C_1 = \max\left[0.43, \frac{\eta}{\eta+5}\right], \quad \eta = S\frac{k}{\epsilon}, S = \sqrt{2S_{ij}S_{ij}}$$

Here, G_k, G_b, Y_M are generation of TKE due to mean velocity gradient, generation of TKE due to buoyancy and contribution of the fluctuating dilatation in compressible turbulence to the overall dissipation rate respectively. C_2 and $C_{1\epsilon}$ are constants, σ_k and σ_ϵ are turbulent Prandtl numbers for k and ϵ and S_k and S_ϵ are user-defined source terms [31].

3.5 Kω-sst turbulence model

Kω-sst is a two equation model proposed by Menter [33]. This model effectively implements k-omega model at wall boundary region and k-ε model at free stream region by using blending function. Kω-sst model modifies turbulent viscosity to model transport effects of turbulent shear stress. This is considered one of the best two equation models because of its robustness and accuracy to wall bounded flows. In the thesis, this could provide better results in predicting separation zone.

3.5.1 Transport equation for kω-sst turbulence model

$$\frac{\partial}{\partial t}(\rho k) + \frac{\partial}{\partial x_i}(\rho k u_i) = \frac{\partial}{\partial x_j}\left(\Gamma_k \frac{\partial k}{\partial x_j}\right) + \tilde{G}_k - Y_k + D_k + S_k \qquad \textbf{(3-13)}$$

$$\frac{\partial}{\partial t}(\rho\omega) + \frac{\partial}{\partial x_i}(\rho\omega u_i) = \frac{\partial}{\partial x_j}\left(\Gamma_\omega \frac{\partial\omega}{\partial x_j}\right) + G_\omega - Y_\omega + D_\omega + S_\omega \qquad \textbf{(3-14)}$$

Here, $\tilde{G}_k$, G_ω , D_ω represent generation of TKE due to mean velocity gradients; generation of ω and cross-diffusion term respectively. Γ_k , Y_k represent effective diffusivity and dissipation of k. Γ_ω , Y_ω represent effective diffusivity and dissipation of ω. S_k and S_ω are user-defined source terms [31].

3.6 Reynolds Stress turbulence model

RSM was developed from work by Launder [34, 35, 36] and is the most sophisticated RANS model. This is also known as second order or second moment closure model. It is different from other RANS models in a sense that it avoids the concept of isotropic turbulence. This model solves six transport equations for Reynolds stresses and one dissipation rate equation.

At wall bounded regions, RSM increases anisotropy by supposing the pressure fluctuations normal to wall. This model is expected to behave well for anisotropic flows and many complex flows. However, the computational cost is high because of more equations involved. It has been reported to perform poorly for axis-symmetric jets and unconfined recirculating flows.

3.6.1 Transport equation for RSM turbulence model

Local Time Derivative + Convection $\left(C_{ij}\right)$ = - Turbulent Diffusion $\left(D_{T,ij}\right)$ + Molecular Diffusion $\left(D_{L,ij}\right)$ - Stress Production $\left(P_{ij}\right)$ - Buoyancy production $\left(G_{ij}\right)$ + Pressure Strain $\left(\varphi_{ij}\right)$ - Dissipation $\left(\epsilon_{ij}\right)$ - production by System rotation $\left(F_{ij}\right)$ + User-defined Term

In the above equation, the following terms C_{ij} , $D_{T,ij}$, P_{ij} and F_{ij} do not require modelling whereas $D_{T,ij}$, G_{ij} , φ_{ij} and ϵ_{ij} require modelling to close the equation [31].

Chapter 4: Computational domain, Mesh generation and Flow conditions

4.1 Computational domain

The given problem setup consists of a flat plate with a circular injection hole of 4mm diameter (D). Taking the origin at the centre of the jet-hole, the domain extends from X/D = -5 to +8 in the x-direction, Y/D = 0 to +18 in the y direction and Z/D = -9.6 to +9.6 in the z-direction as shown in figure 4-1. It has been noted by Santiago and Dutton [1] that the flow is asymmetric as viewed on X/D =3 and X/D =5 planes due to unknown reasons, therefore full computational domain has been generated.
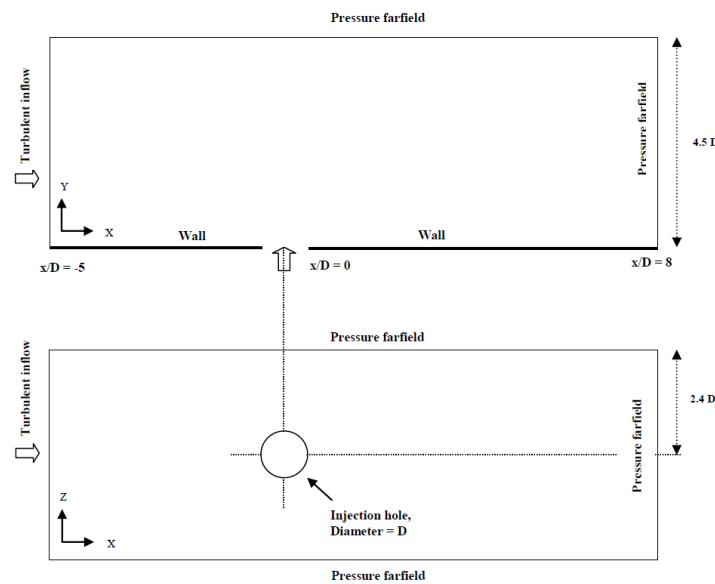
Figure 4-1 Schematic of the computational domain for JISC case with associated boundary conditions.

4.2 Mesh Generation

Three dimensional, multi-block, structured mesh was created using ICEM-CFD. The mesh consists of 29 blocks with O-grid type structured mesh. The O-grid type of structured block was made at the region of jet-hole as seen in figure 4-2a. This technique was necessary to refine the mesh at the place where the gaseous injected air interacts with the free-stream flow. Also, since we know that the jet plume inclines with angle 55 degrees as suggested by Santiago and Dutton [1], the area after the O-grid block is further blocked for required refinement as in figure 4-2b.
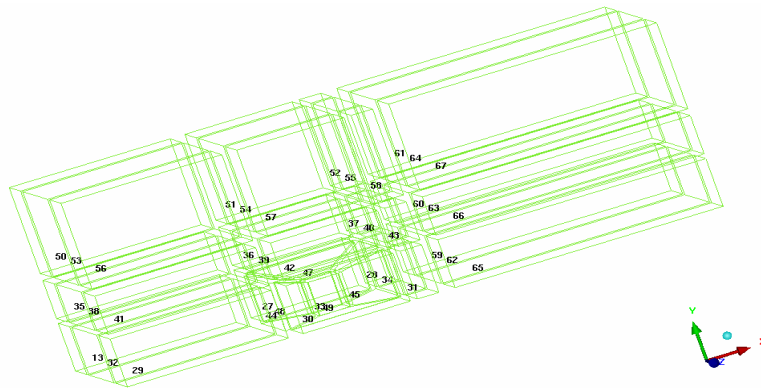
(a)
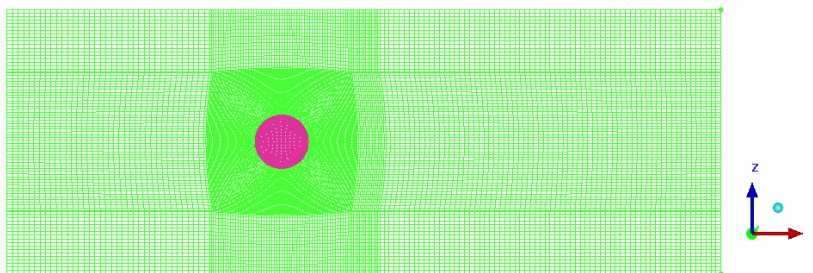
(b)

Figure 4-2 Meshing Strategy (a) Blocking strategy (b) Mesh on the bottom wall

The meshing strategy targets to achieve $y^+ = 1$. Thus, the first cell height from the available Reynolds number of 2.4 E+4 and reference length of 4mm

(diameter of the jet-hole) has been calculated to be 0.0000026m. Y plus contour of the surface has been plotted in figure 4-3. Figure 4-3 shows that Y plus is less than 1.939.
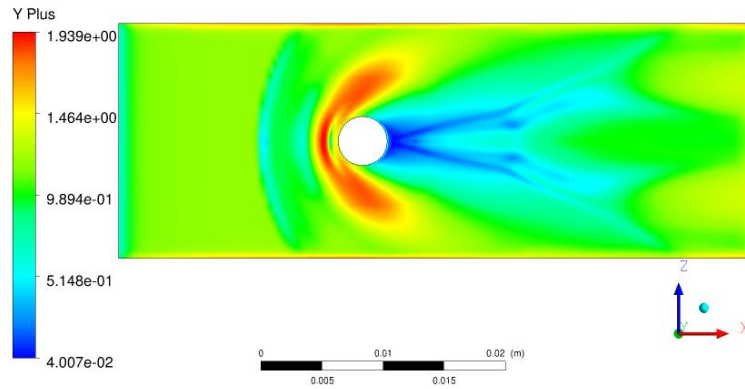
Figure 4-3 Wall Y plus contour

4.3 Boundary conditions

As illustrated in Fig 4-1, the computational domain is allowed with Supersonic Turbulent Boundary Layer (STBL) profile at the inlet (X/D = -5) available from the experiment. This shortens the computational domain as compared to ILES. The bottom surface was applied with adiabatic no-slip wall boundary type. Except the bottom wall, all other sides of the computational domain have been defined with pressure far-field boundary type. Use of symmetry boundary type at upper, left and right sides were tried for this case, but it resulted in suppressed jet plume and improper flow features.

Far-field conditions of static pressure and temperature for cross-flow as well as jet were calculated from the available stagnation temperature and pressure as in table 4-1. Top, left, right and outflow surfaces were provided with Mach number = 1.6 with X- component of flow direction = 1 whereas under-expanded sonic jet injection was provided with Y-component of flow direction = 1. Turbulent intensity was found to be 4.5% and turbulent length scale to be 1.24mm.

Table 4-1 Inflow conditions

Property	Cross-flow		Jet		Units
	Stagnation	Static	Stagnation	Static	
Pressure	241	56.7	476	251.46	kPa
Temperature	295	195.11	295	245.83	K
Mach number	1.6		1		

4.4 Solver settings

The computations have been performed using FLUENT 12.1.4. Density based solver was used for steady RANS simulations. Species transport equation was included with the continuity, momentum and energy equations. Multi-species technique employed the respective material properties (air and air for JISC case with J = 1.7; and air and hydrogen for JISC case with J=0.3) with default mass diffusivity value of 2.88E-05 m^2/s. Second order upwind scheme was used to reduce round-off errors. Implicit method with courant number = 1 was used along with Roe-FDS flux type formulation. Under-relaxation factors were enabled with value of 0.5 for improving convergence.

4.5 Grid Independence study

Pressure plots have been used to study the grid convergence. Three different meshes summarized in table 4-2 have been considered for the study. Figure 4-4a plots absolute pressure integral on the surface of the wall for different meshes. The value is almost constant for all mesh sizes and shows that it is grid independent. Also in figure 4-4b, all the meshes show not much difference among them. The finest mesh of 2.8 million cells has been adopted for the investigation of the case since it provides the best flow features.

Table 4-2 Number of cells corresponding to the mesh

Mesh	Number of cells
Mesh 1	188807
Mesh 2	663152
Mesh 4	2757162

(a)   (b)
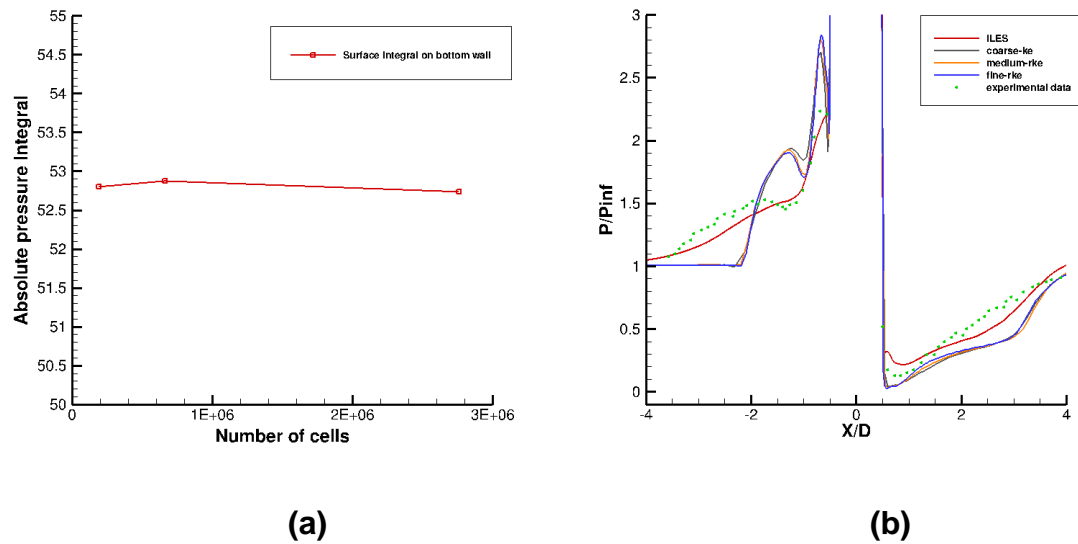
Figure 4-4 Grid convergence study using kω-sst model (a) absolute pressure integral vs. number of cells (b) study on pressure plots

Also to be noted from a paper by Adelp, Longo and Emunds [37] is that the jet-on conditions of the flow didn't satisfy the grid convergence at flow separation areas. They investigated the flow with free-stream Mach number = 2.8 using Reynolds averaged hybrid Navier - Stokes code TAU of DLR. For jet-off conditions, the investigation satisfied grid convergence on pressure profile whereas jet-on conditions failed to do so.

Chapter 5: Numerical investigation on standard JISC case with J= 1.7

5.1 Qualitative Analysis

5.1.1 Mach number contours at Z/D = 0 plane

(a)

(b)

(c)

(d)
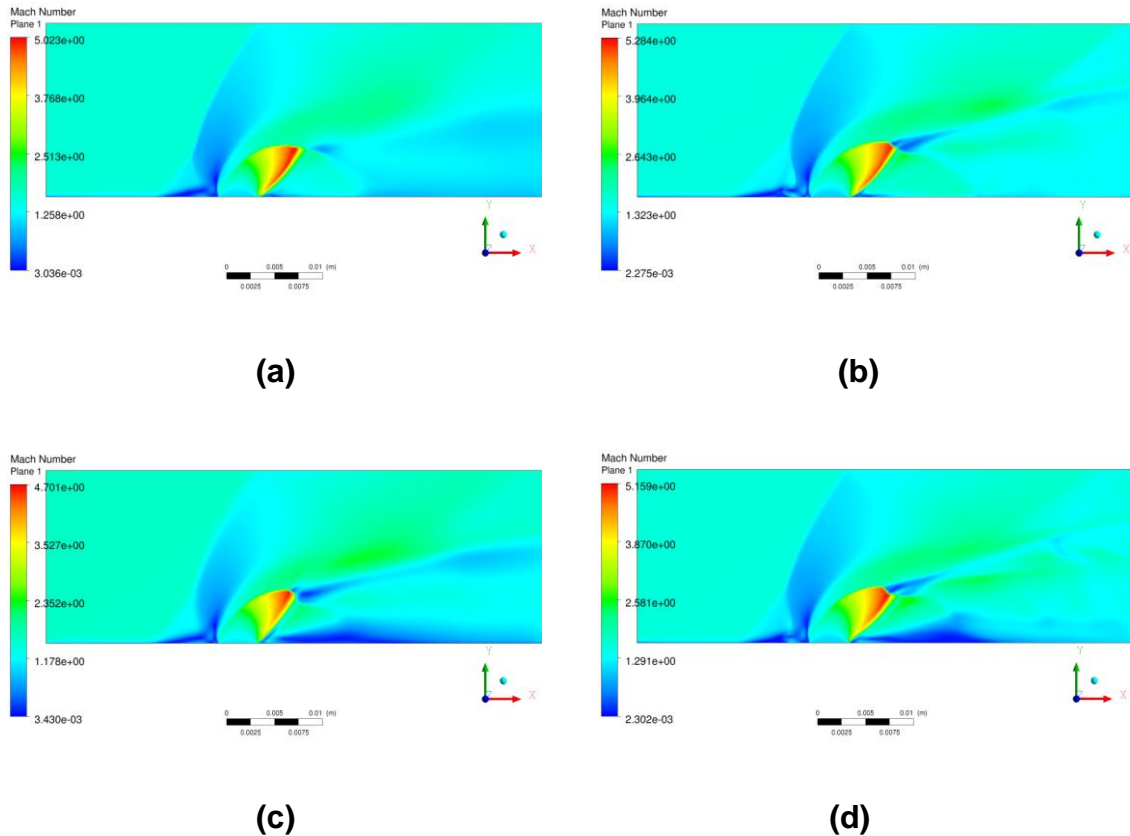
Figure 5-1 Mach number contours at Z/D = 0 plane (a) realizable k-ϵ (b) kω-sst (c) SA (d) RSM

Figure 5-1 shows the use of four different RANS models and their effect on the flow physics of the Jet Injected Supersonic Cross-flow (JISC) and Supersonic Turbulent Boundary Layer (STBL). All the major flow features like bow shock, barrel chock, Mach disk, lambda shock, upstream separation zone, recirculation zone just in-front of jet plume, recirculation zone just behind the jet plume, and a hint of weak reflected shock from the triple point, have been observed in all four figures with some noticeable difference.

41

It can be clearly observed in figure 5-1a that realizable k-ϵ fails to predict Mach disk. Figure 5-1b which is due to kω-sst RANS model can be noticed with the position of lambda shock farthest upstream among others. Although major discrepancies, quantitative discussions (section 5.2.1, 5.2.2) show that kω-sst is the best RANS model out of four to predict the lambda shock position although major discrepancies are observed when compared to ILES and experiment. Figure 5-1d (RSM model) has the largest Mach disk length. Maximum Mach number is noticed at location just before Mach disk inside the barrel shock. All RANS models over-predict the maximum Mach number compared to ILES and experiment. Experiment predicts 2.66 and ILES predicts 3.7 whereas RANS models predict around 5. Kω-sst predicts the maximum of 5.3 whereas Spalart Allmaras predicts the minimum of 4.7 among all RANS models. Another noticeable and important difference is that realizable k-ϵ and kω-sst have small recirculation zone just after the jet plume whereas SA and RSM have bigger recirculation zone.

5.1.2 Velocity Streamlines at Z/D = 0 plane

Figure 5-2 presents the streamlines of the flow for jet injected into supersonic cross-flow. Streamlines depict the maximum fluid flow at the windward side of the jet plume. The obstruction created by the jet plume creates bow shock and lambda shock. This aids to the formation of separation zone and recirculation zone. Noticeable feature in the streamlines is the separation zone where tertiary vortices can be seen for kω-sst and RSM. These tertiary vortices have been reported by Chenault and Beran [38] in the same location as in figures 5-2b and 5-2d. Tertiary vortices appear as counter rotating vortices between the core of the horse shoe vortex and the bottom wall. The larger recirculation zone in the leeward side of the jet plume also can be clearly seen in figures 5-2c and 5-2d for SA and RSM RANS models.

(a)

(b)

(c)

(d)
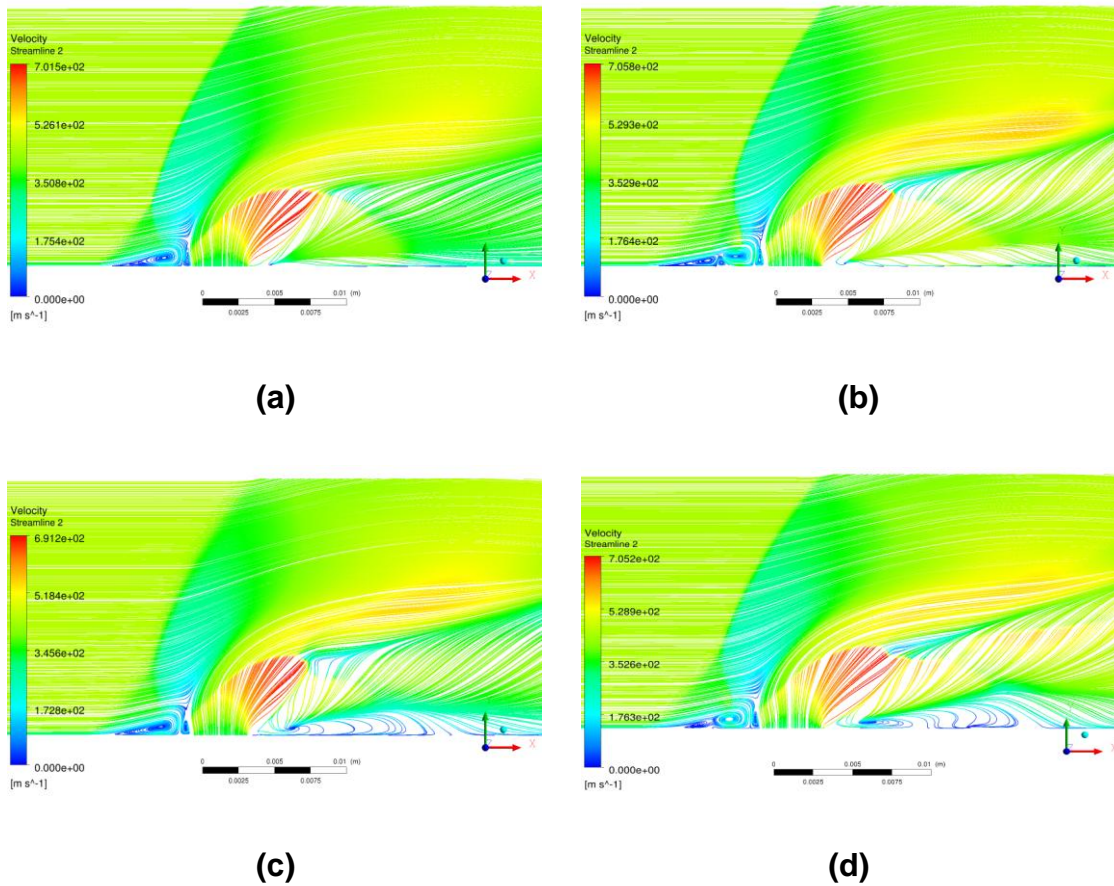
Figure 5-2 Velocity streamlines at Z/D = 0 mid-plane (a) realizable k-ε (b) kω-sst (c) SA (d) RSM

5.1.3 Isometric view of the flow

Mach contour, vorticity magnitude and pressure coefficient along with the 3D streamlines have been shown together in figure 5-3. Though all the properties of flow will be discussed separately, a combined look of the flow properties will give a better understanding to the flow.

Figure 5-4 shows the iso-surface for the Q-criterion of value 0.0035 using realizable k-ε. The existence of counter rotating vortices (CRV), horse-shoe vortex and trailing counter rotating vortices (TCRV) can be easily seen in figure 5-4.

(a)

(b)

44
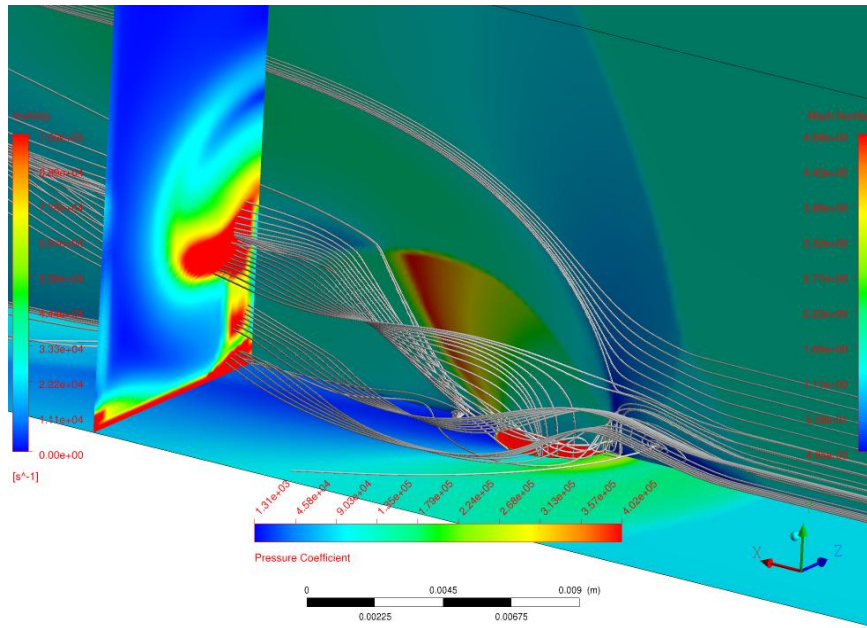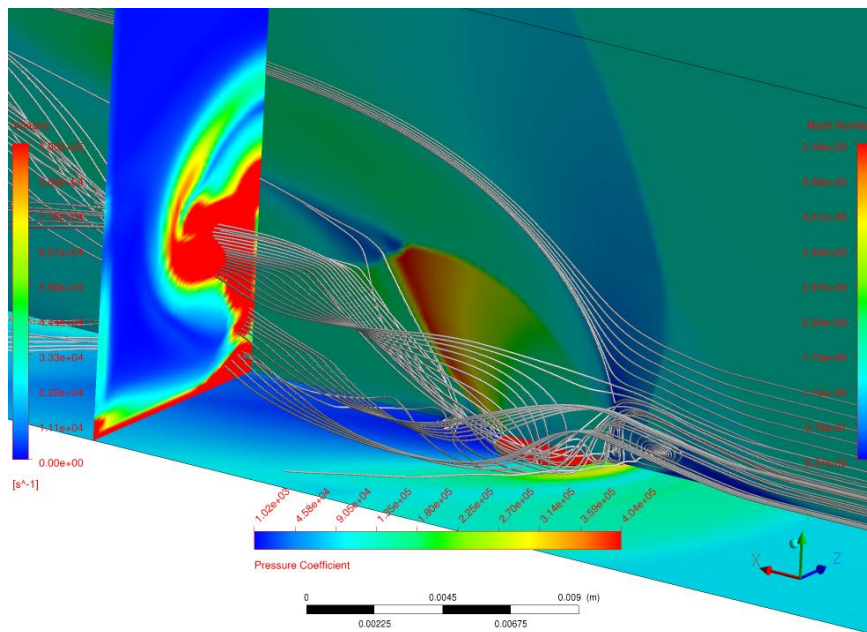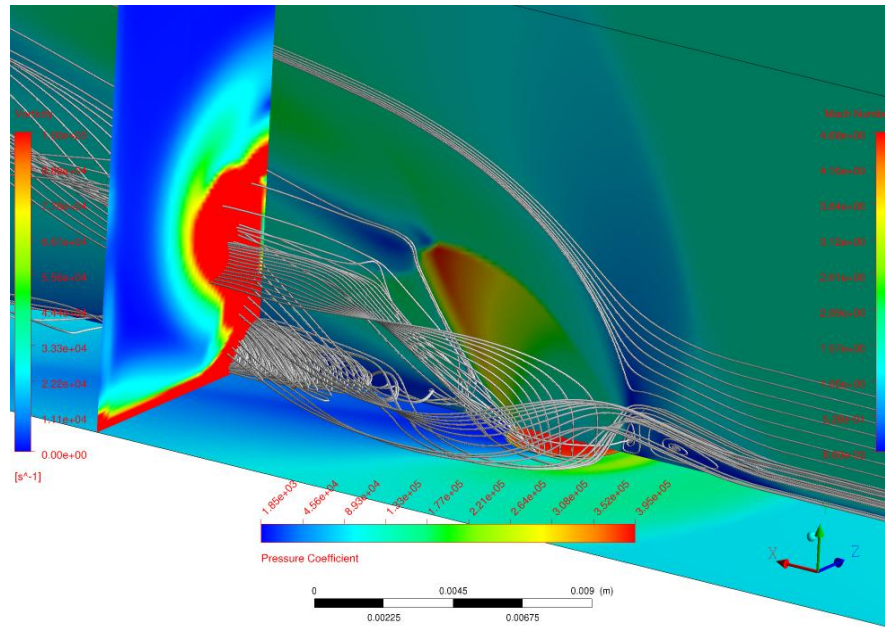
(c)
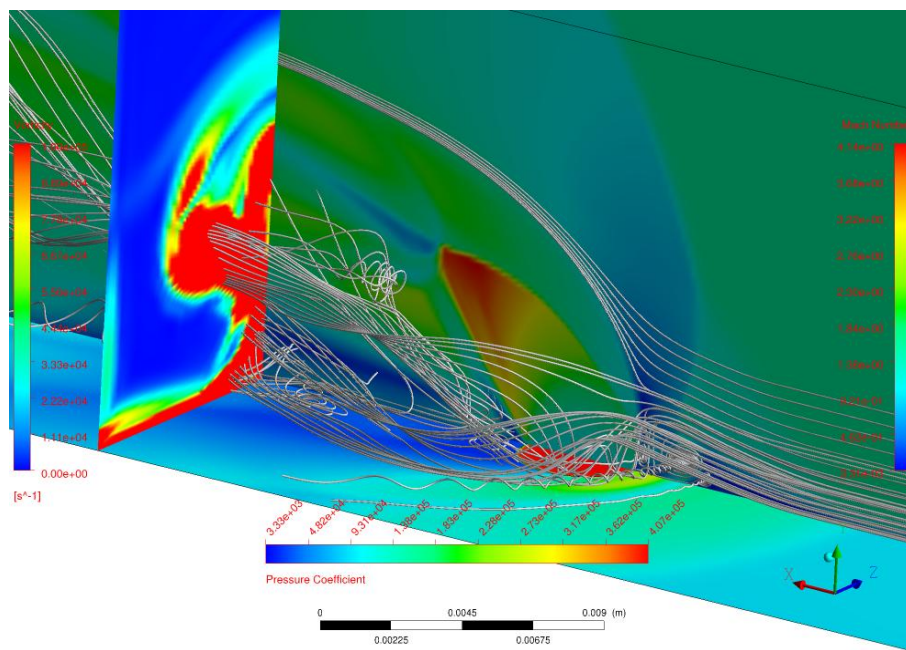
(d)

Figure 5-3 3D streamlines view: pressure coefficient (ZX plane): Mach Number (XY plane): vorticity magnitude (YZ plane) plane (a) realizable k-ϵ (b) kω-sst (c) SA (d) RSM
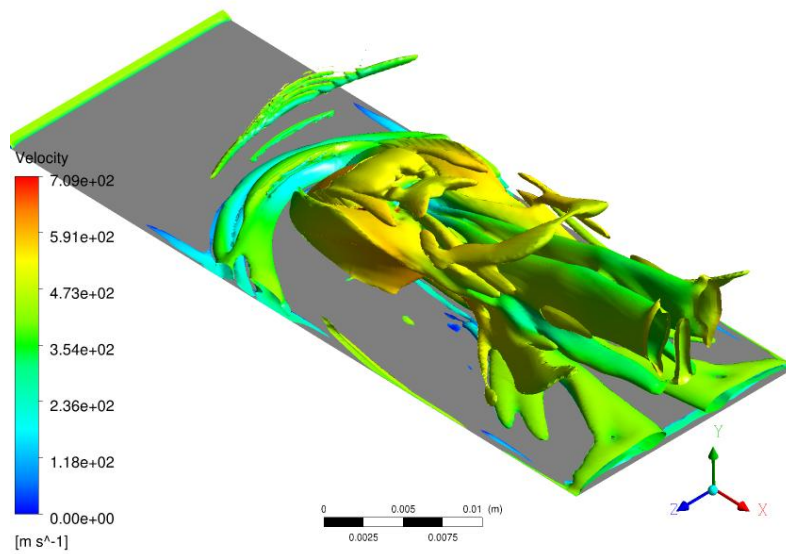
Figure 5-4 Q criterion (0.0035) iso-surfaces

5.1.4 Surface wall streamlines

(a)

(b)

(c)

(d)
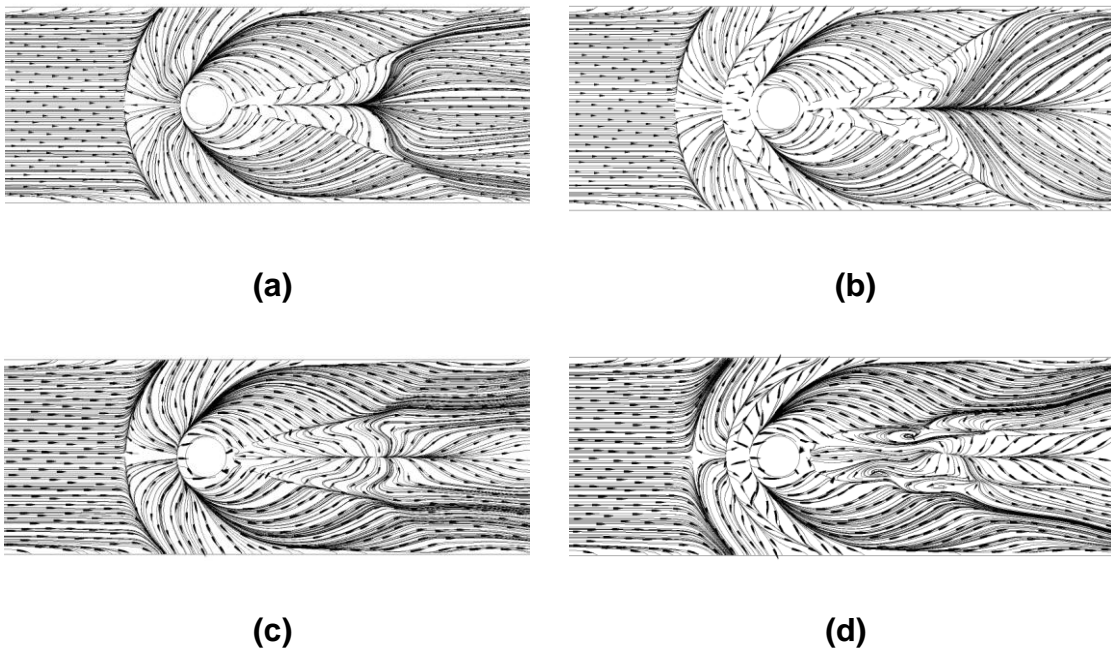
Figure 5-5 Surface wall streamlines (a) realizable k-ε (b) kω-sst (c) SA (d) RSM

Streamlines on the flat plate have been plotted in figure 5-5 for different RANS models. The general flow streamlines along with separation line and

reattachment line are well predicted by all RANS models. Also, the tertiary vortices formed between the core of horseshoe vortex and wall for kω-sst and RSM models can be located by lines between the separation and reattachment line in figure 5-5b and 5-5d. It can also be noticed that at the downstream of jet-hole, the streamlines for Realizable k-ε (fig 5-5a) are calm whereas RSM model predicts formation of vortices. The vortices formed at downstream of jet-hole are not symmetric (fig 5-5d). The experimental results by Santiago and Dutton [1] also show some asymmetry at X/D = 3 plane with unknown reason for it. Closely looking at the streamlines at 5-5d, the vortices look like the Karman vortex street past a circular body.

5.1.5 Turbulent Kinetic Energy contours at Z/D = 0 plane

The contours of TKE are shown by figure 5-6. High TKE regions are upstream, leeward side and windward side of jet plume. High TKE at upstream is due to the shock - boundary layer interaction. Windward side of jet plume has high TKE due to the high shear between the cross-flow and the jet fluid. High TKE at leeward side of jet plume is explained by eddy formations at this region. Counter-rotating vortices arise from downstream of jet plume suggesting high TKE.

Analysing figure 5-6, we can deduce that realizable k-ε predicts high TKE out of all RANS models compared. Kω-sst predicts very low TKE (1.87 E+4) compared to 4.31 E+4 predicted by realizable k-ε. In figure 5-6b for kω-sst model, maximum TKE is found at upstream and windward side of jet plume. RSM (figure 5-6c) show maximum production of TKE in the leeward side of the jet plume. This explains that TKE production is dominated by the formation of counter – rotating vortices for RSM model. However, referring to section 5.2.4, quantitative analysis shows that realizable k-ε only best predicts the TKE of the flow.

47

(a)   **(b)**

(c)
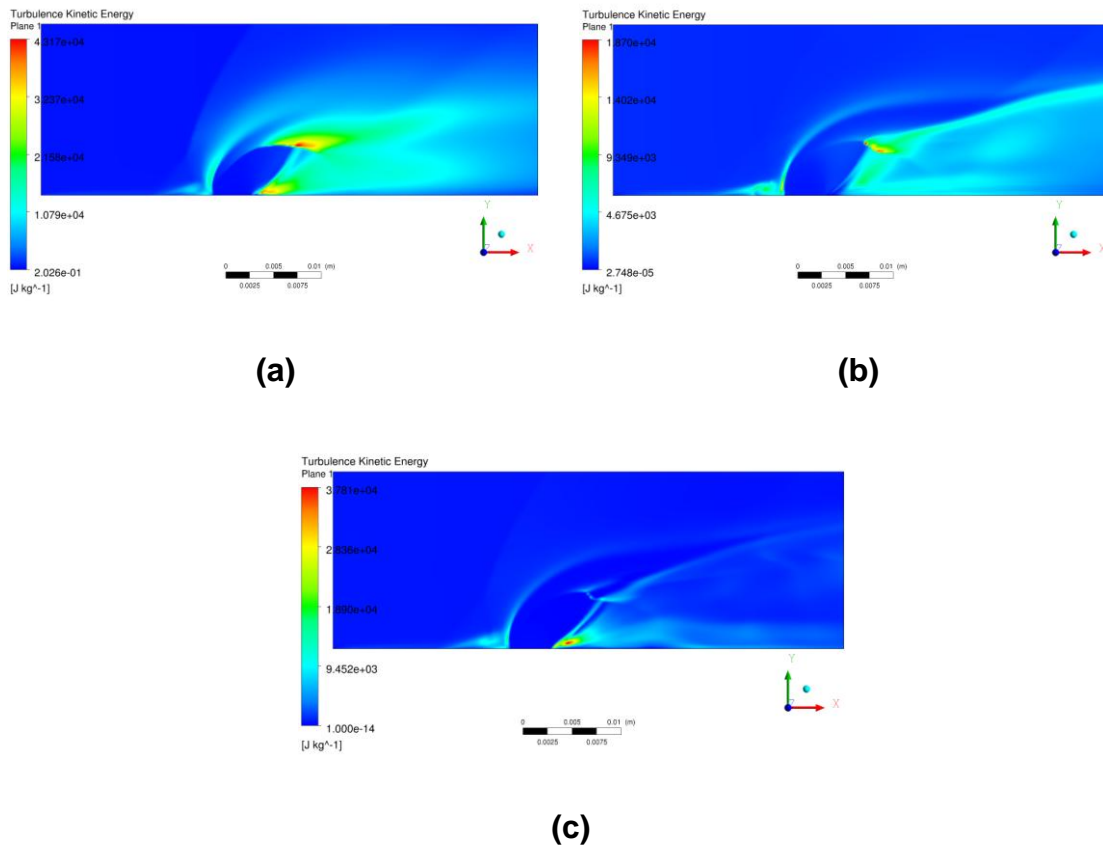
Figure 5-6 Turbulent Kinetic Energy (TKE) contour at Z/D = 0 mid-plane (a) realizable k-ϵ (b) kω-sst (c) RSM

5.1.6 Passive scalar contours at Z/D = 0 plane

Passive scalar (air mass fraction) contours of the jet fluid have been plotted in figure 5-7. It is seen that realizable k-ϵ (figure 5-7a) predicts proper mixing of free-stream and jet fluid. Kω-sst, SA and RSM turbulence models (fig 5-7b, 5-7d) show no progressive dilution downstream. High spreading rate of jet fluid and mixing at the leeward side of the jet plume is noticed for realizable k-ϵ and SA models whereas RSM model predicts the least.
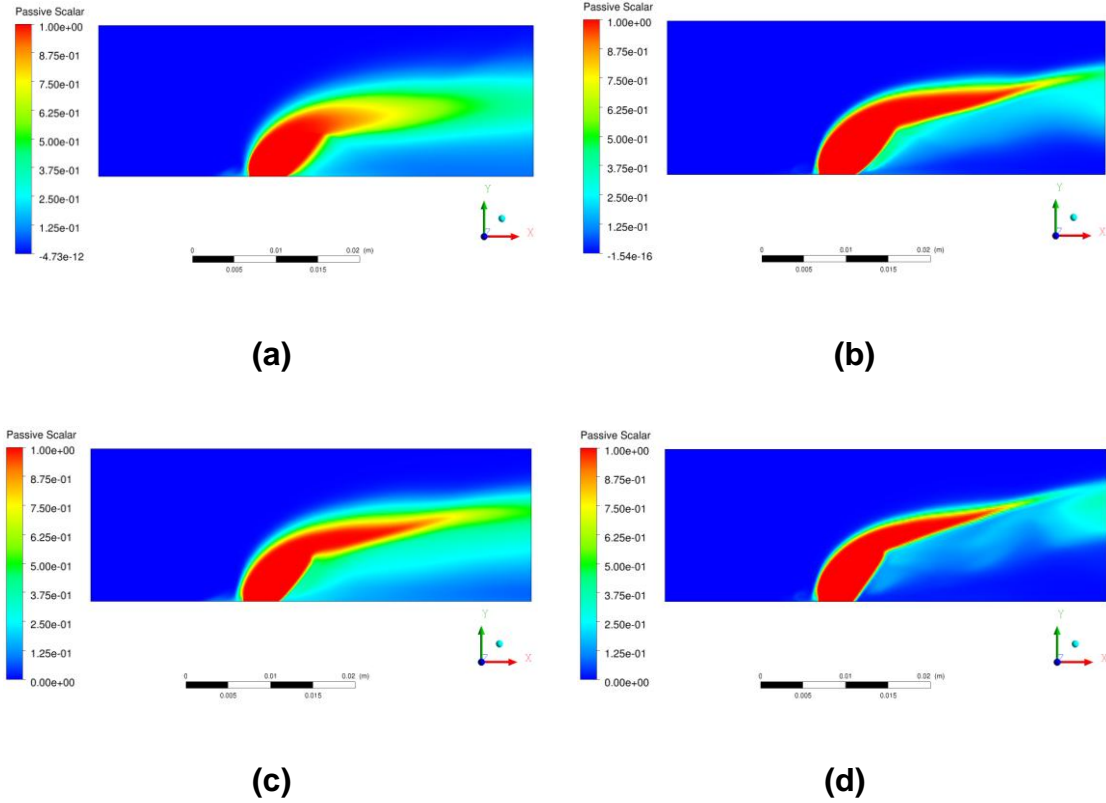
Figure 5-7 Passive Scalar (jet air mass fraction) contours at Z/D = 0 mid-plane (a) realizable k-ε (b) kω-sst (c) SA (d) RSM

5.1.7 Mach number streamlines at Y/D = 1 plane

The streamlines pattern at a height of Y/D = 1 have been studied in figure 5-8. The Mach number contours show the recirculation region before the jet plume and the streamlines are seen to move around the jet plume. Kω-sst and RSM (fig 5-8b and 5-8d respectively) show distinct separation line in the recirculation zone. This is because of the tertiary vortices formed which were explained in figure 5-2.

(a)   (b)

(c)   (d)
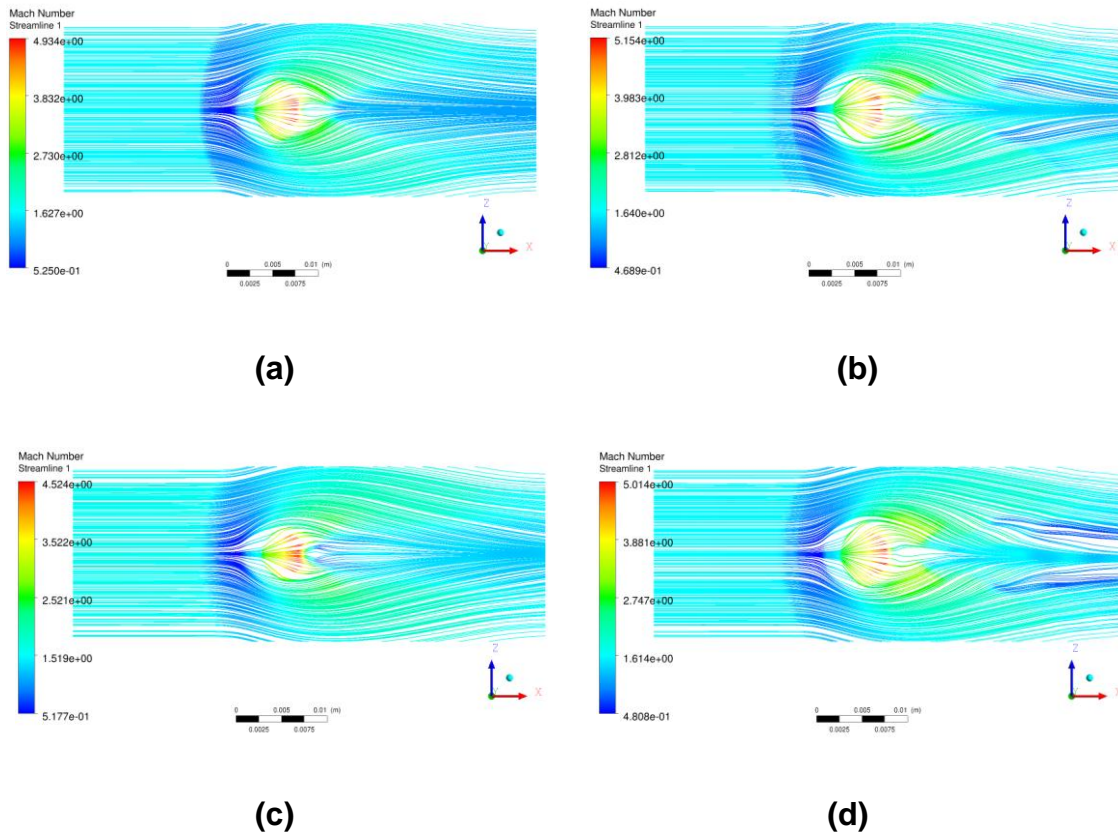
Figure 5-8 Mach number streamlines on ZX plane at Y/D =1 (a) realizable k-ϵ (b) kω-sst (c) SA (d) RSM

5.1.8 Passive scalar contours at Y/D = 1 plane

Contours of passive scalar (air mass fraction) at a height of Y/D = 1 have been studied in figure 5-9. The mass fractions of jet fluid (air) when interacting with supersonic cross-flow (air) have been plotted for four RANS models. Seeing the contours at the region near to jet-hole, the plots explain that just downstream of jet plume, RSM mixes quickly, followed by SA. Realizable k-ϵ and kω-sst does not show much mixing. Still further downstream, Realizable k-ϵ model depicts progressive dilution (fig 5-9a). Figures 5-9b and 5-9d (kω-sst and RSM turbulence models respectively) show contours of unmixed fluid at far downstream. Also, these models show no mixing at all at the centreline of the plane. This explains that the jet fluid doesn't get entrained to the centreline

region of the plane. SA model (fig 5-9c) show similar mixing trends to realizable k-ϵ but dilution are comparatively not strong enough.

(a)

(b)

(c)

(d)
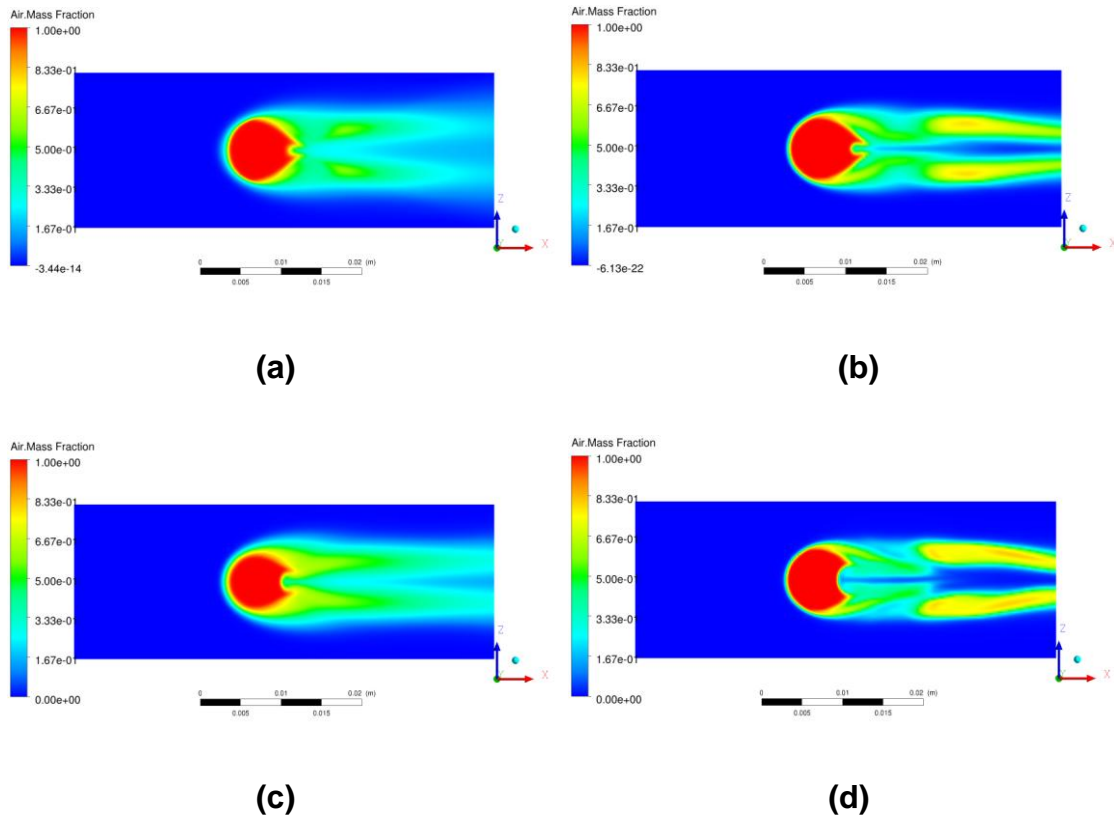
Figure 5-9 Passive scalar (air mass fraction) contours on ZX plane at Y/D = 1 height (a) realizable k-ϵ (b) kω-sst (c) SA (d) RSM

5.1.9 Turbulent kinetic energy contours at Y/D = 1 plane

Contours of TKE has been analysed at ZX plane at a height of Y/D = 1. Maximum TKE is predicted by realizable k-ϵ (fig 5-10a) compared to kω-sst and RSM (fig 5-10b and 5-10c respectively). Only, realizable k-ϵ show high TKE at the recirculation region upstream. It can be observed that high TKE is concentrated at the downstream region of jet-hole for realizable k-ϵ whereas kω-sst and RSM have high TKE at a small region just behind the jet plume and extends symmetrically downstream. Also, prediction of considerable TKE all over the plane by RSM turbulence model is noticed in figure 5-10c.

(a)   (b)

(c)
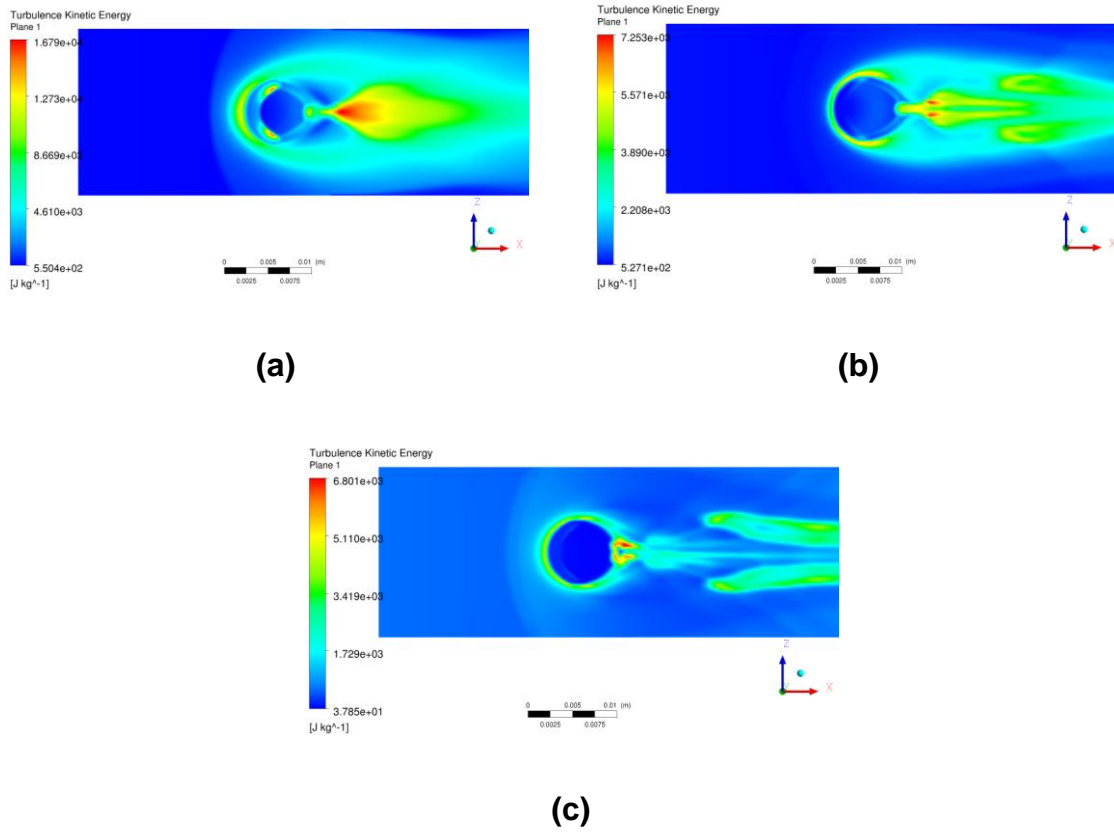
Figure 5-10 Turbulent Kinetic Energy contours on ZX plane at Y/D = 1 height (a) realizable k-ϵ (b) kω-sst (c) SA (d) RSM

5.1.10 Mach number streamlines at X/D = 1 plane

Figure 5-11 presents Mach number streamlines on X/D = 1 plane. All the plots show similar pattern of streamlines except Spalart Allmaras which predicts smaller counter rotating vortices. These counter rotating vortices are the kidney shaped vortices that form behind the jet plume and aids in the mixing process. The difference can also be found in the maximum value of Mach number in the contours of fig 5-11. Realizable k-ϵ predicts high Mach number at the jet plume region just before the Mach disk. Compared to experimental and ILES data, all RANS models highly over-predict Mach number at region just before the Mach disk. This was discussed in section 5.1.1.
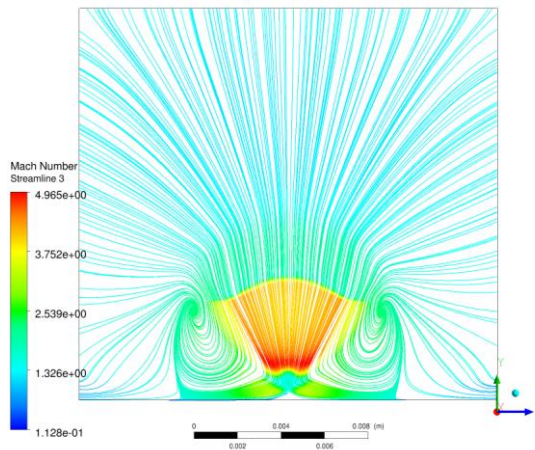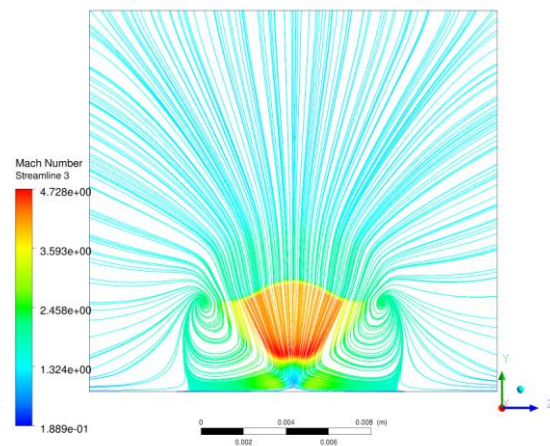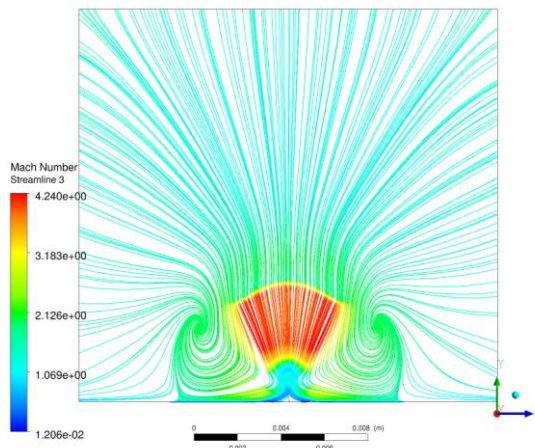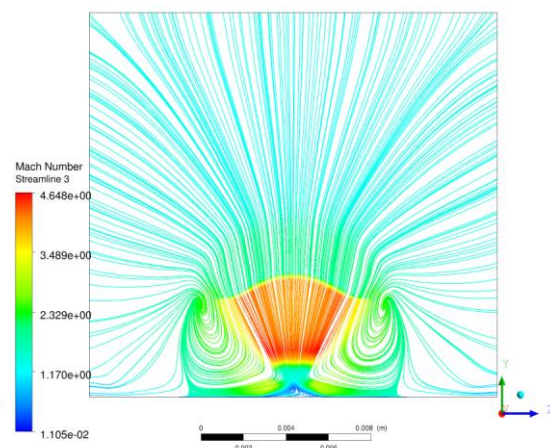
Figure 5-11 Mach number streamlines on X/D =1 plane (a) realizable k-ε (b) kω-sst (c) SA (d) RSM

5.1.11 Passive scalar (air mass fraction) contours at X/D = 1 plane

(a)

(b)

(c)

(d)

Figure 5-12 Passive scalar (air mass fraction) contours on X/D =1 plane (a) realizable k-ϵ (b) Kω-sst (c) SA (d) RSM

Passive scalar contours at X/D = 1 plane have been presented in figure 5-12. The contours predict that mixing process starts as soon as the jet is injected. Figure 5-12c shows contours of passive scalar for Spalart Allmaras which predicts mixing at windward as well as leeward side of the jet plume unlike the ILES. ILES predicts more mixing only on the windward side due to thick shear layer. Kω-sst (fig 5-12b) and RSM (fig 5-12d) predicts minimal mixing at this plane. It can also be observed that for these two RANS models, maximum mixing happens on the side of the jet plume because of the extensions in the jet plume. Realizable k-ϵ (fig 5-12a) shows some expected behaviour of more

mixing on the windward side of the jet plume due to same reasons of high shear layer between fluids. Also to be noticed is the slightly higher prediction of jet trajectory for RSM model compared to other RANS models.

5.1.12 Turbulent kinetic energy contours at X/D = 1 plane

(a)   (b)

(c)
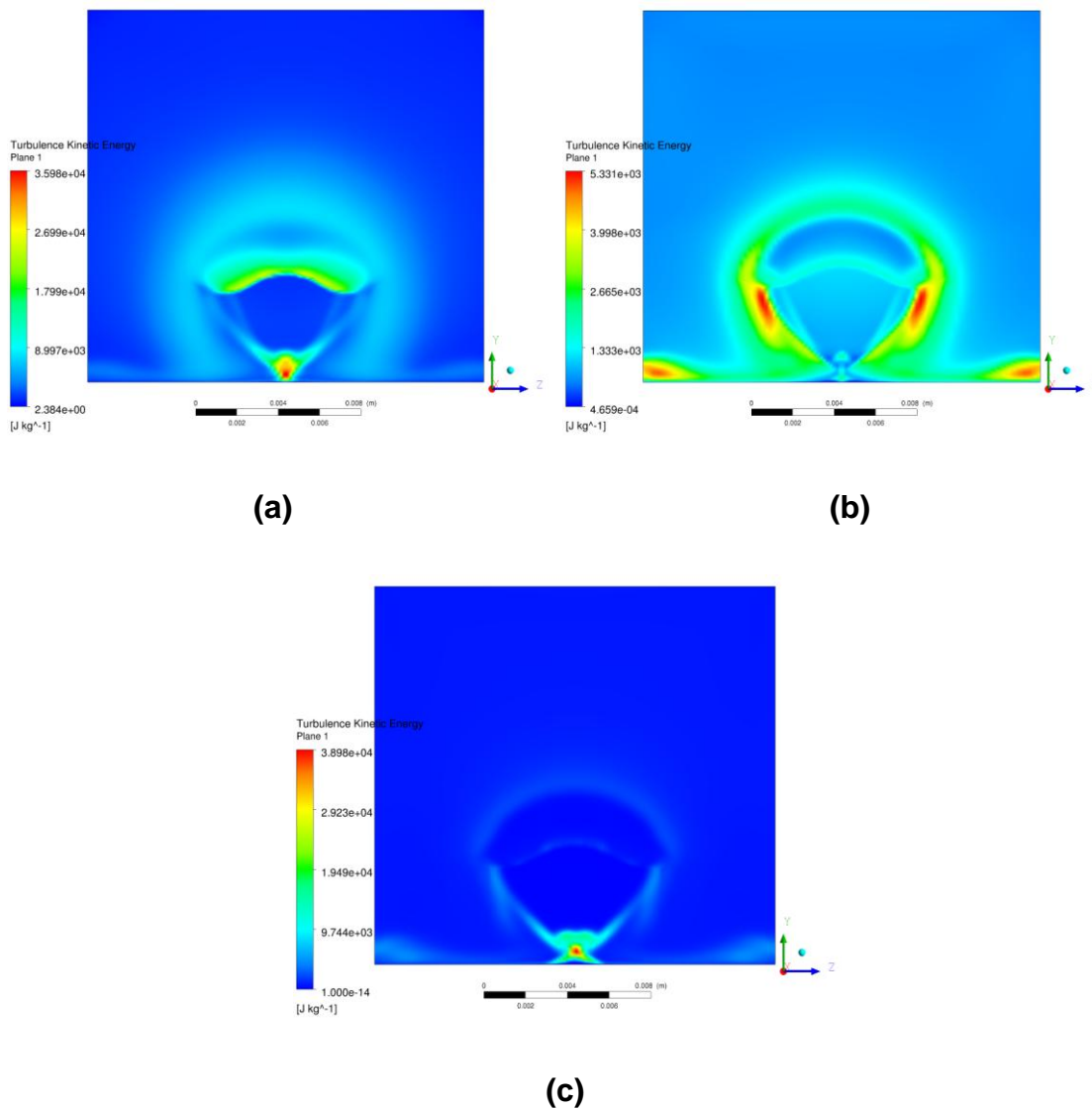
Figure 5-13 Turbulent Kinetic Energy contours on X/D =1 plane (a) realizable k-ϵ (b) Kω-sst (c) RSM

As mentioned earlier, high TKE exists at three regions in the JISC case. These regions are upstream, windward and leeward side of the jet plume. Realizable

k-ϵ (fig 5-13a) correctly predicts high TKE at windward and leeward side of jet plume. This explains that high shear is created due to the interaction of jet and cross-flow at the windward side. Also, high TKE at leeward side of jet plume illustrates the formation of counter rotating vortices at this region that grows in size as it moves further downstream. Kω-sst (fig 5-13b) shows unexpected contours with high TKE at the sides of jet plume and regions horizontally away from the centreline. RSM (fig 5-13c) shows contours of high TKE at the leeward side suggesting formation of counter rotating vortices but fails to predict the region of high TKE at the windward side. Clearly, Realizable k-ϵ is the only RANS model that gives correct prediction of the distribution of TKE at X/D = 1 plane. Also, kω-sst predicts maximum TKE value fairly low than realizable k-ϵ and RSM turbulence models.

5.1.13 Mach number streamlines at X/D = 3 plane

Plane X/D = 3 as in figure 5-14 introduces new pair of trailing counter rotating vortices along with the growing main counter rotating vortices. New trailing counter rotating vortices are due to the low pressure recirculation region just downstream of the jet plume. The main counter rotating vortices cover a large area where mixing occurs. It can be observed that the surface trailing vortices have the opposite rotation to the main counter rotating vortices. This enhances better mixing of fluid.

As expected from the paper by Rana et al. [8], realizable k-ϵ (fig 5-14a and Spalart Allmaras (fig 5-14c) turbulence models predict growth in the size of main counter rotating vortices with formation of small trailing counter rotating vortices near to the surface. Along with formation of small trailing counter rotating vortices, kω-sst (fig 5-14b) and RSM (fig 5-14d) turbulence models predict another small trailing counter rotating vortices above the main counter rotating vortices as pointed out by Viti et al. [6]. In terms of Mach number distribution, the surface trailing counter rotating vortices have very low Mach number just because they exist at the recirculation zone behind the jet plume.

(a)
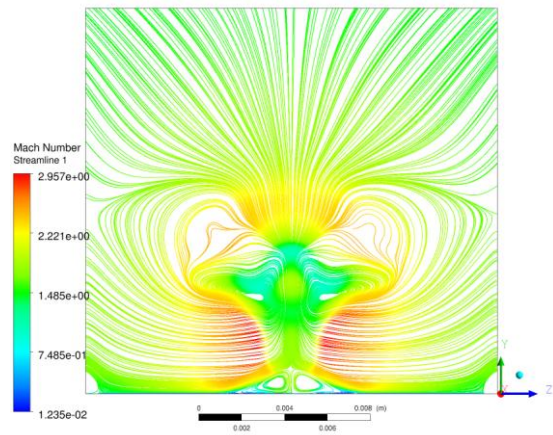
(b)
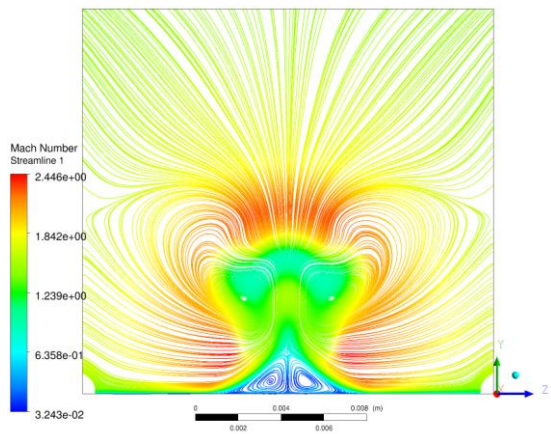
(c)
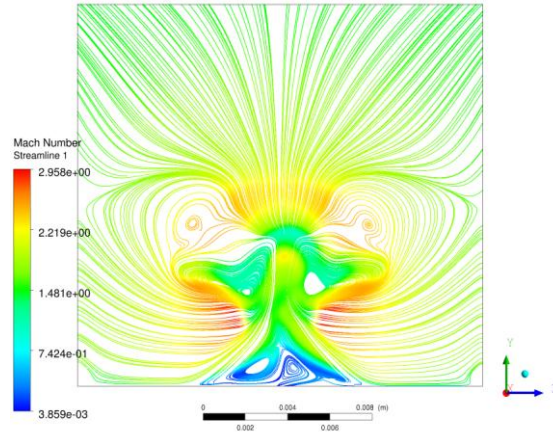
(d)

Figure 5-14 Mach number streamlines on X/D =3 plane (a) realizable k-ϵ (b) kω-sst (c) SA (d) RSM

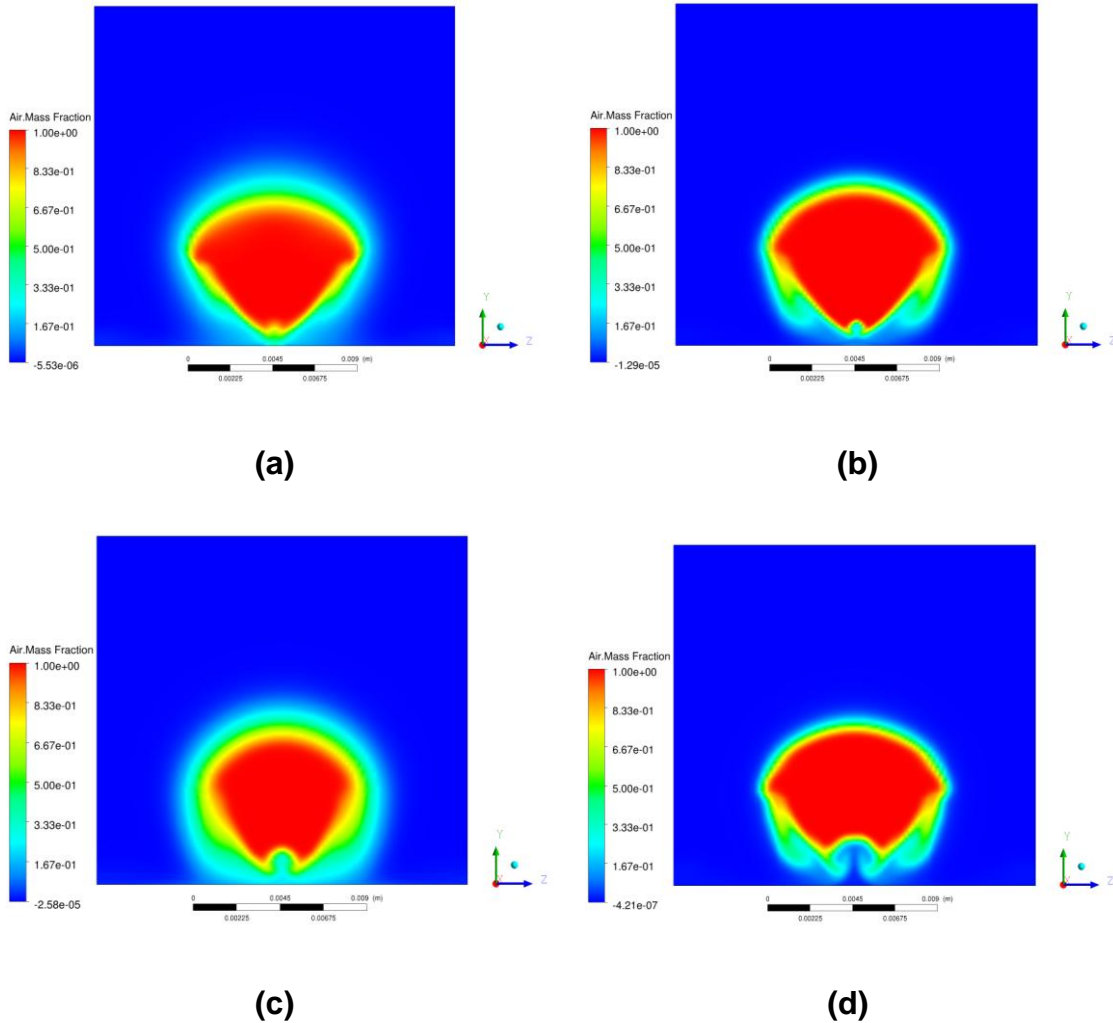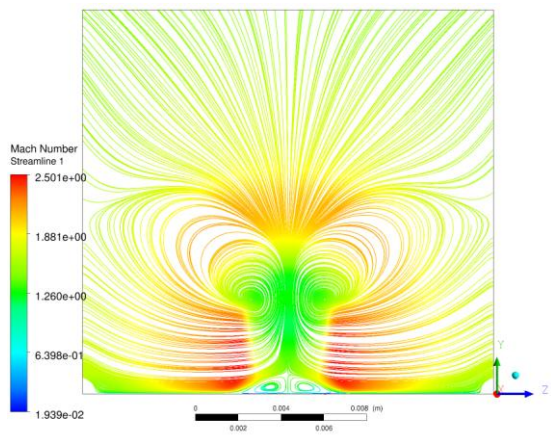## 5.1.14 Passive scalar contours at X/D = 3 plane

(a)

(b)

(c)

(d)
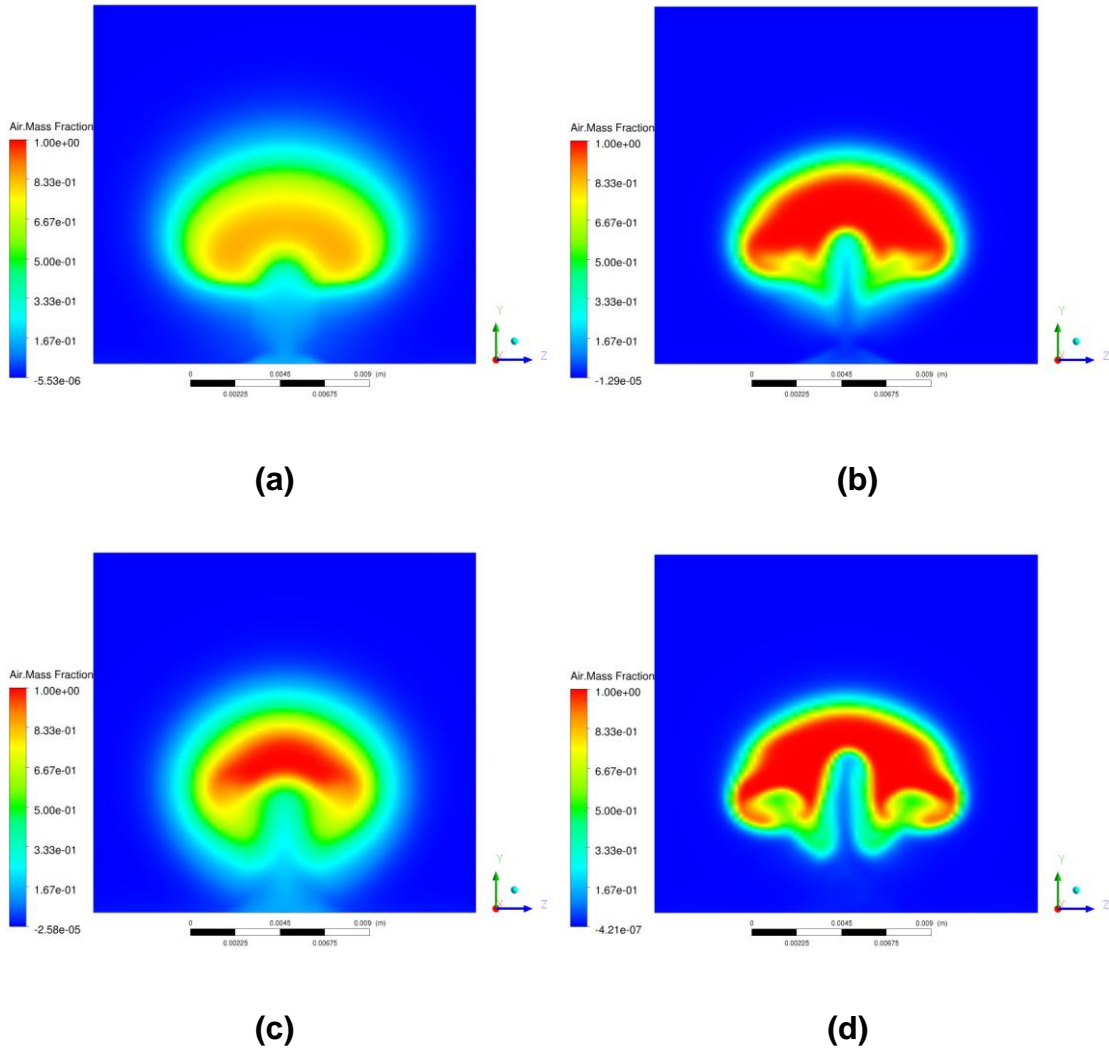
Figure 5-15 Passive scalar (air mass fraction) contours on X/D =3 plane (a) realizable k-ϵ (b) kω-sst (c) SA (d) RSM

Passive scalar contours at X/D = 3 plane have been shown by figure 5-15. Referring to the passive scalar profiles (section 5.2.5), good predictions of mixing comparable to ILES results were shown by realizable k-ϵ (fig 5-15a). The contour plot in figure 5-15a explains progressive mixing downstream. The jet trajectory can also be tracked from the contours. Again referring to section 5.2.5, Spalart Allmaras and kω-sst provide good prediction of the jet trajectory. From the contours in figure 5-15, realizable k-ϵ has comparatively lower height of jet centreline than the kw–sst or the Spalart Allmaras model. Figures 5-15b

and 5-15d show that kω-sst and RSM have the least mixing compared to others.

5.1.15 Turbulent kinetic energy contours at X/D = 3 plane

(a)

(b)

(c)
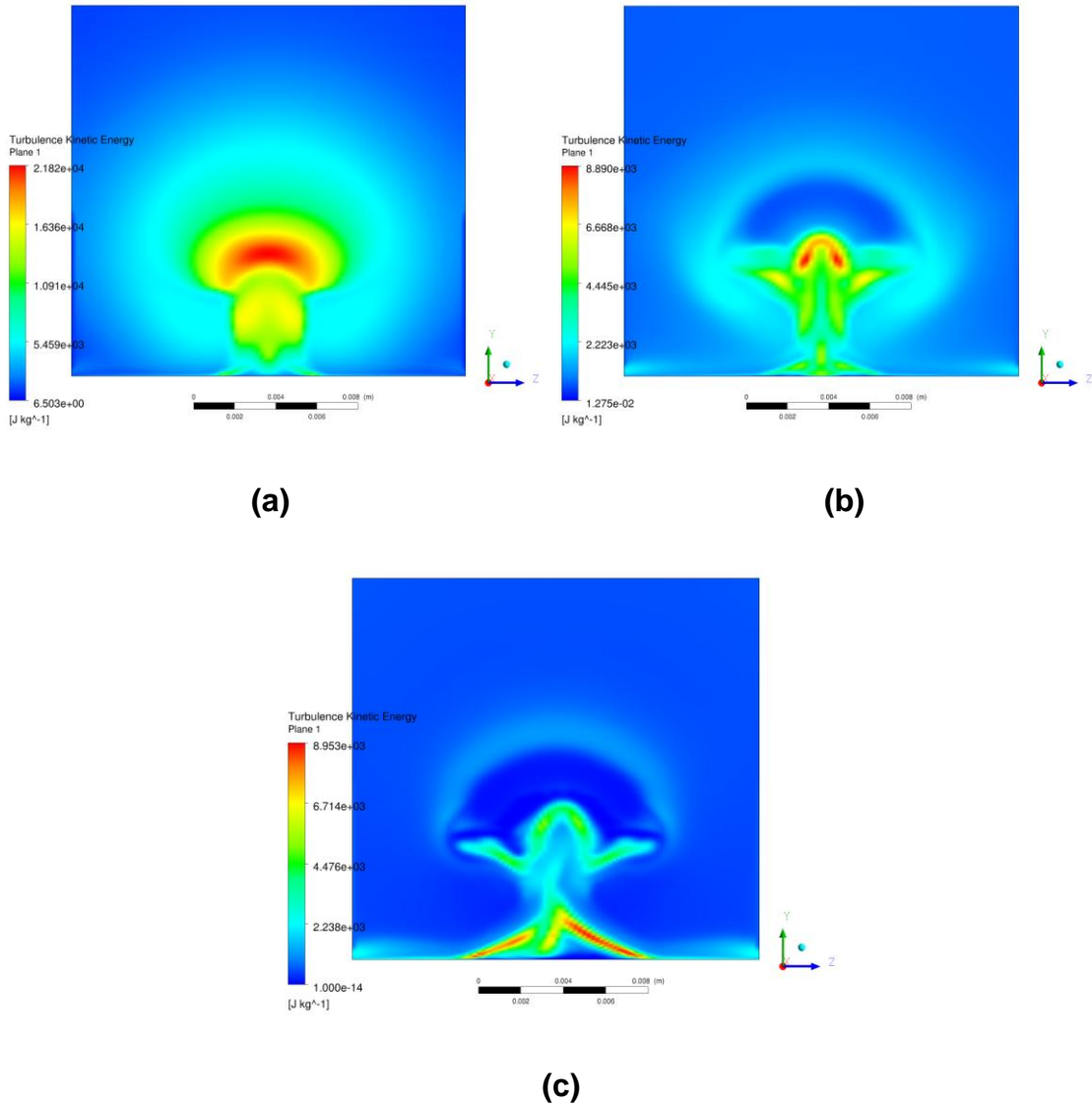
Figure 5-16 Turbulent kinetic energy contours on X/D = 3 plane (a) realizable k-ε (b) kω-sst (c) SA (d) RSM

TKE contours have been presented in figure 5-16. Figure 5-16a which uses realizable k-ε model, clearly shows high TKE at the high shear region between fluids at plane X/D = 3 whereas kω-sst (fig 5-16b) and RSM (fig 5-16c) models

predict comparatively less. Fig 5-16c which uses RSM model predicts asymmetry in the TKE contour at low height. The lower right half of the contour has higher TKE than the left counter-part. This asymmetry can be referred to results from experiment by Santiago and Dutton [1]. At this plane at Y/D = 2, turbulent intensities in the negative Z region were greater than positive Z region by 0.15 times the average cross-flow velocity. On the contrary, at Y/D = 1, turbulent intensities in the negative region were smaller than positive region by 0.18 times the average cross-flow velocity. The reason of asymmetry is unknown in experiment but for RSM RANS model, this could be due to the inclusion of Reynolds Stress Transport equations which redistributes Reynolds stresses in the shear flows. Also, turbulent stresses are linked to production of shear stress. Other RANS models with one and two equation models show perfect symmetry.

5.1.16 Mach number streamlines at X/D = 5 plane

Figure 5-17 presents the Mach number streamlines at far downstream plane of X/D = 5 plane. The main counter rotating vortices responsible for mixing phenomena have grown in size along with the surface trailing counter rotating vortices that appeared from X/D = 3 plane. Realizable k-ϵ (fig 5-17a) and kω-sst (fig 5-17b) show that the trailing counter rotating vortices have grown to big sizes compared to Spalart Allmaras (fig 5-17c) and RSM (fig 5-17d). Here, the most noticed figure is 5-17d where a pair of small trailing counter rotating vortices that appeared on top of main counter rotating vortices in X/D = 3 plane has shifted bottom of it.
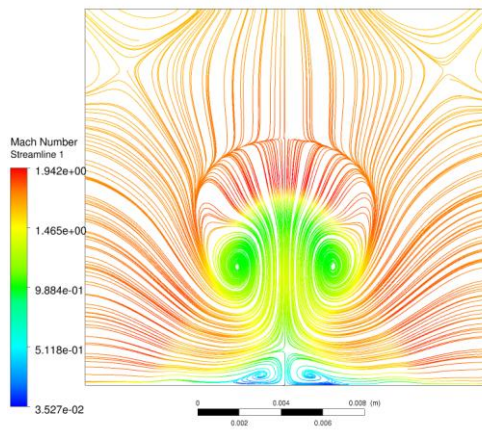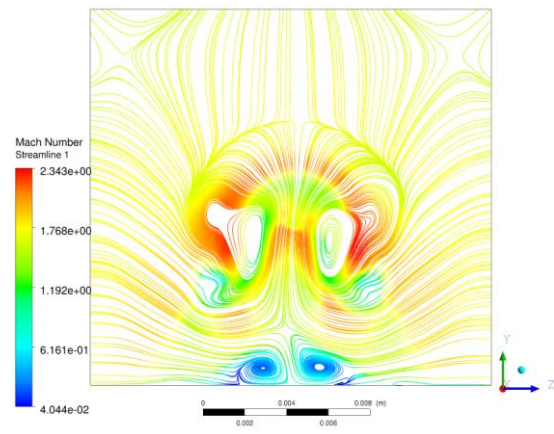
Figure 5-17 Mach number streamlines at X/D =5 plane (a) realizable k-ε (b) kω-sst (c) SA (d) RSM

5.1.17 Passive scalar contours at X/D = 5 plane

(a)

(b)

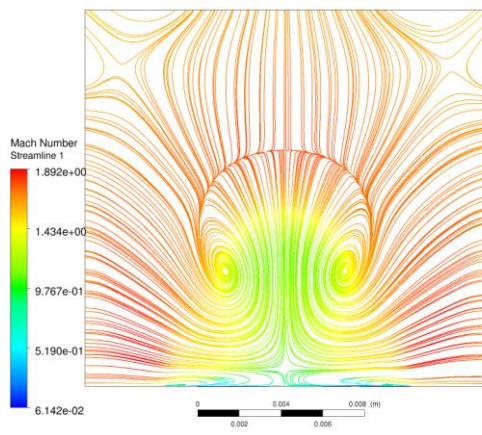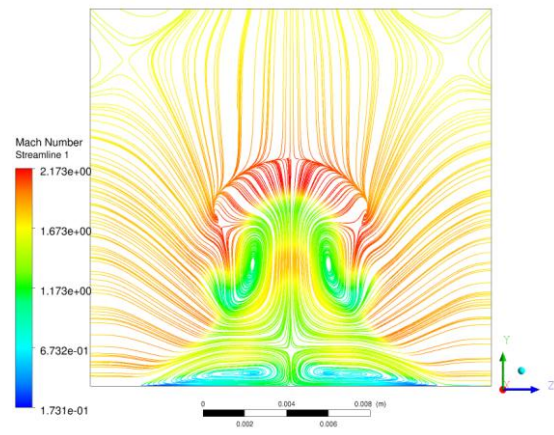
(c)

(d)
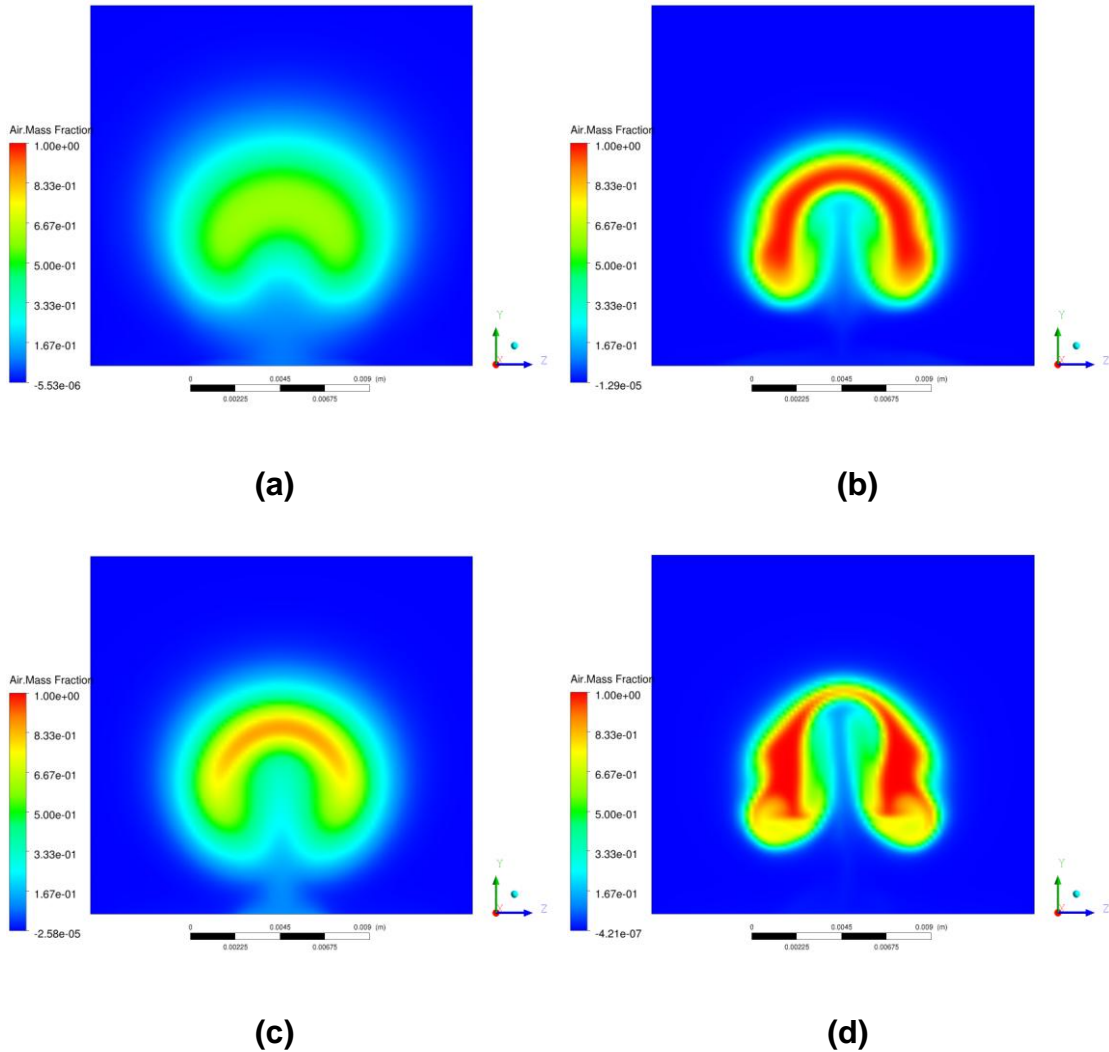
Figure 5-18 Passive scalar (air mass fraction) contours at X/D =5 plane (a) realizable k-ε (b) kω-sst (c) SA (d) RSM

At this plane of X/D = 5, figure 5-18 shows that the jet fluid have diluted remarkably. The contours explain that the mixing area increases as we go downstream because of the CRVs growing in size. Again, realizable k-ε shows the best mixing in figure 5-18a. Referring to section 5.2.5, Spalart Allmaras (fig 5-18c) and kω-sst (fig 5-18b) predicts correct height of jet centreline with under-predicted mixing.

5.1.18 Turbulent kinetic energy at X/D = 5 plane

(a)   (b)

(c)
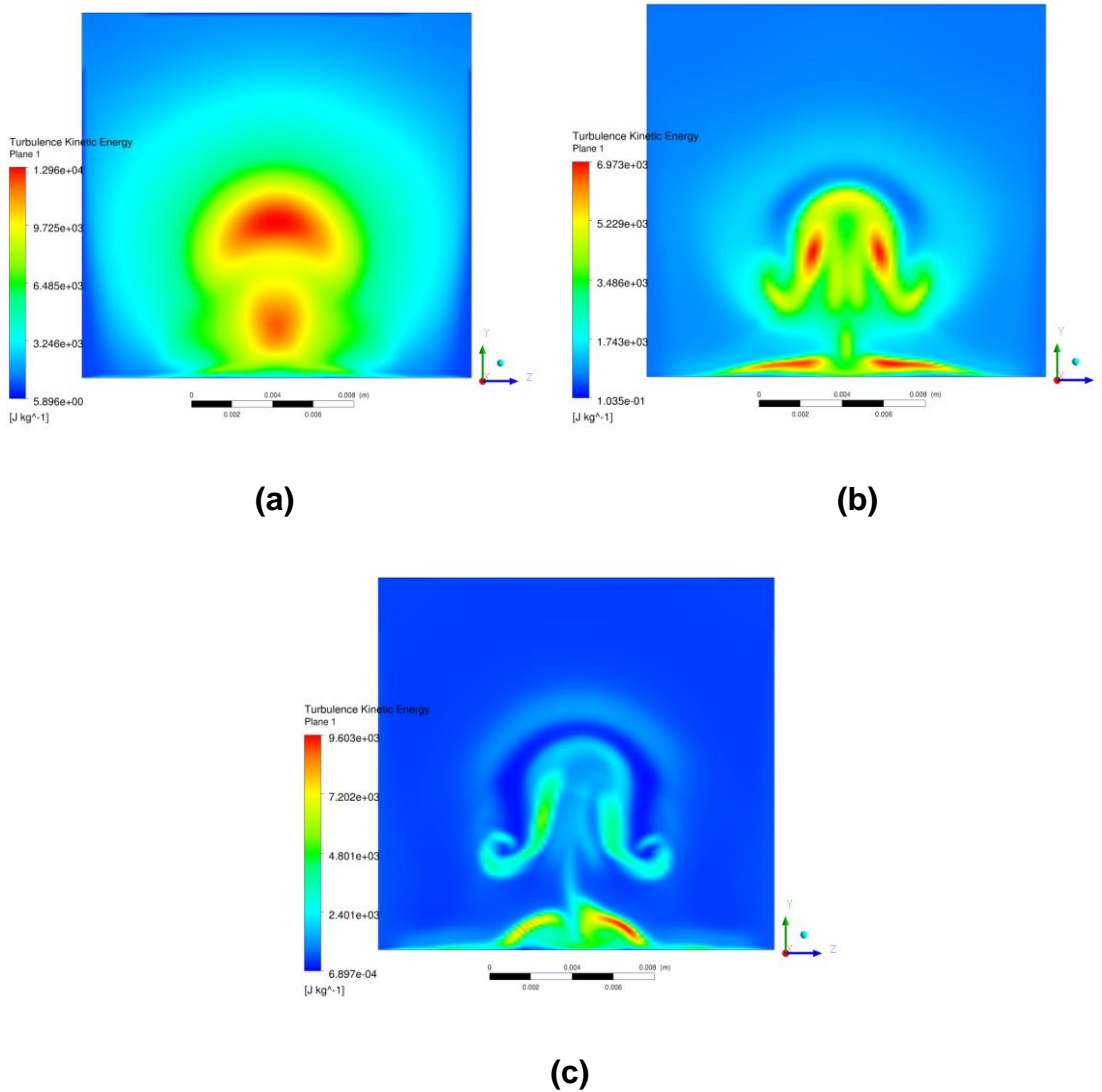
Figure 5-19 Turbulent Kinetic Energy contours at X/D =5 plane (a) realizable k-ϵ (b) kω-sst (c) RSM

As the flow moves downstream, TKE starts dissipating gradually. At X/D = 5 plane, realizable k-ϵ (fig 5-19a) shows good amount of TKE at the mixing region suggesting that the shear layer between the fluid still produces good amount of TKE. Kω-sst (fig 5-19b) and RSM (fig 5-19c) has comparatively lesser TKE than realizable k-ϵ model. High TKE is seen for kω-sst at near the surface because of the increasing sizes of trailing counter rotating vortices. Again, RSM model shows some asymmetry in TKE distribution.

5.1.19 Pressure contours at Z/D = 0 plane

(a)

(b)

(c)

(d)
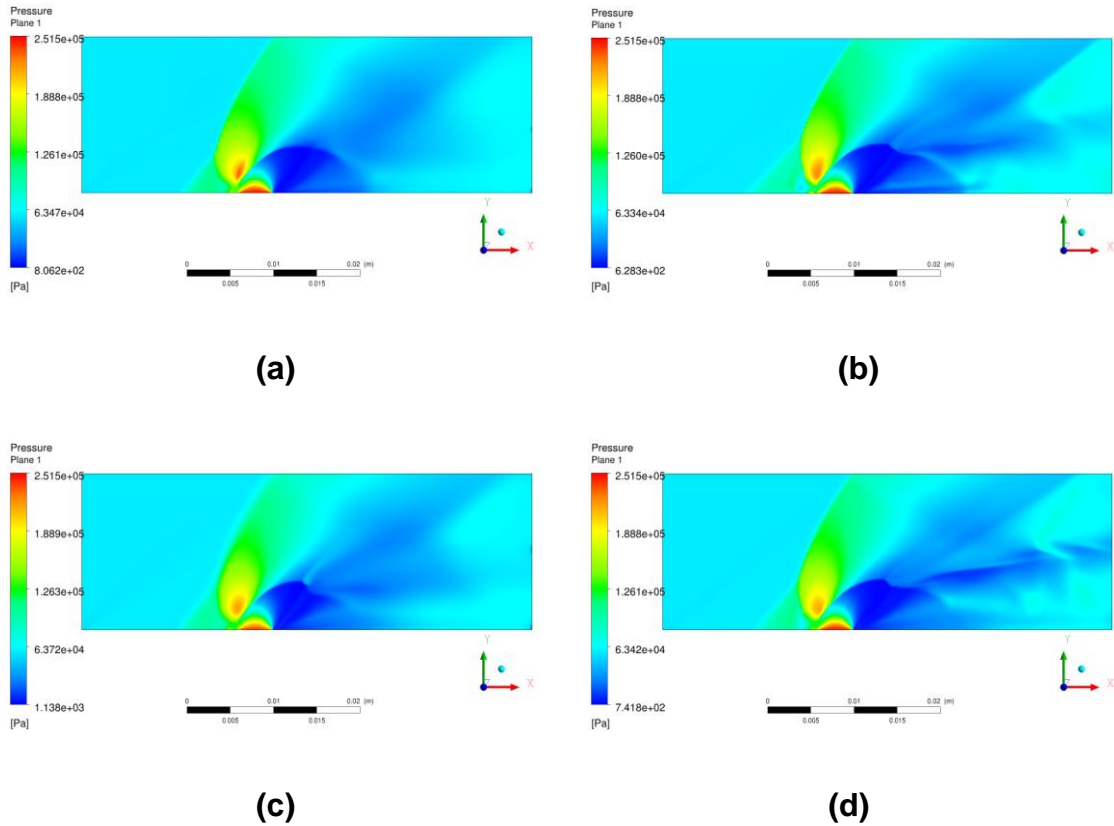
Figure 5-20 Pressure contours at Z/D = 0 plane (a) realizable k-ε (b) kω-sst (c) SA (d) RSM

Figure 5-20 shows the pressure distribution on Z/D = 0 plane. Typically all RANS models present similar behaviour. High pressure is depicted at region behind the bow shock and near the jet-hole. Comparatively, low pressures are seen in the upstream recirculation zone and very low pressure in the region just behind the jet plume. Inside the jet plume, due to the recompression wave formed while exiting from the jet-hole, the jet fluid looses pressure rapidly until it reaches the Mach disk.

5.1.20 Pressure contours at Y/D = 0 plane

(a)

(b)

(c)

(d)
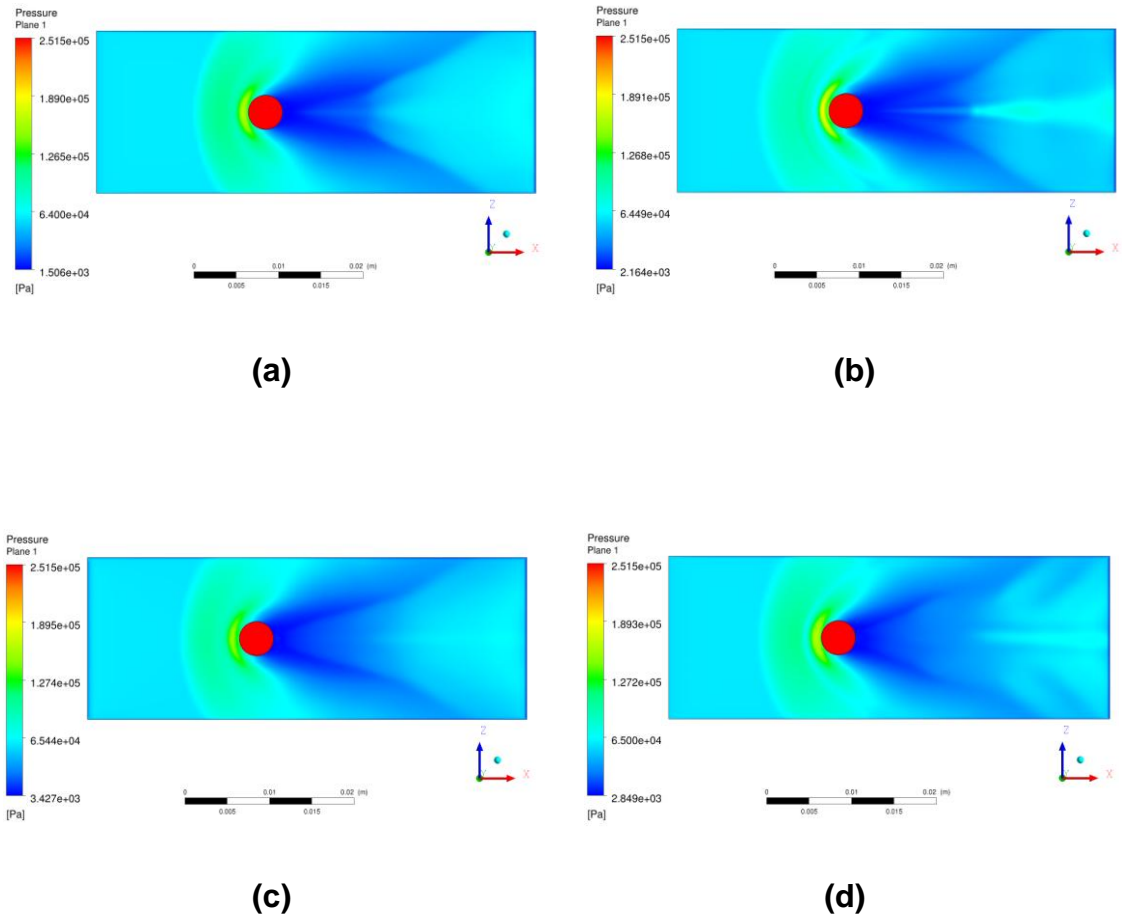
Figure 5-21 Pressure contours at Y/D = 0 plane (a) realizable k-ϵ (b) kω-sst (c) SA (d) RSM

Figure 5-21 shows the pressure contour at Y/D = 0 plane. Almost all RANS models show similar distribution of pressure except far downstream regions that vary insignificantly. The wall pressure increases just before the jet injection and suddenly decreases at the recirculation zone behind the jet plume.

5.2 Quantitative Analysis

5.2.1 X-velocity profiles
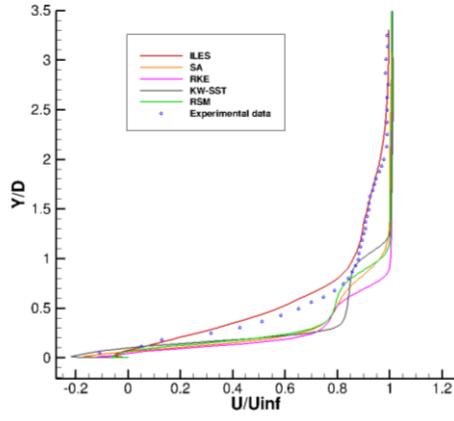
(a)

(b)
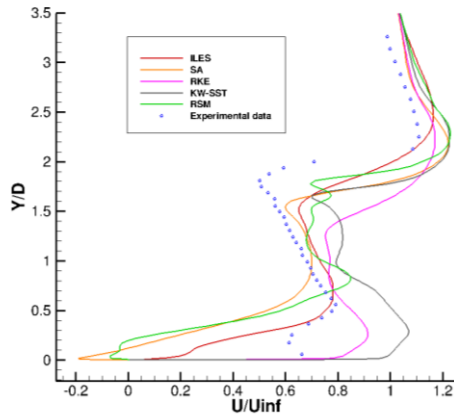
(c)

(d)

(e)

Figure 5-22 Comparison of X-velocity profiles of four RANS models, ILES and experiment at different locations (a) X/D = -1.5 (b) X/D = 2 (c) X/D = 3 (d) X/D = 4 (e) X/D = 5

Figure 5-22 are the comparison of the plots for the stream-wise velocities (normalised by dividing with U_{inf}) at positions upstream (X/D = -1.5) and downstream (X/D = 2, 3, 4, 5) at the mid-plane Z/D=0. The stream-wise velocities are non-dimensionlised by the main free-stream velocities and the length of the x-y-z dimensions are non-dimensionalised by the diameter of the jet-hole. Four different RANS models (Spalart Allmaras, realizable k-ϵ, kω-sst and Reynolds Stress model) are compared with ILES and experimental data.

Figure 5-22a is the position at upstream from the jet and is important for analysing the formation of lambda shock and separation zone. The formations of different structures are governed by the Supersonic Turbulent Boundary Layer Thickness (STBL) and turbulence. At the separation zone, kω-sst model shows good similarity with the experimental data. 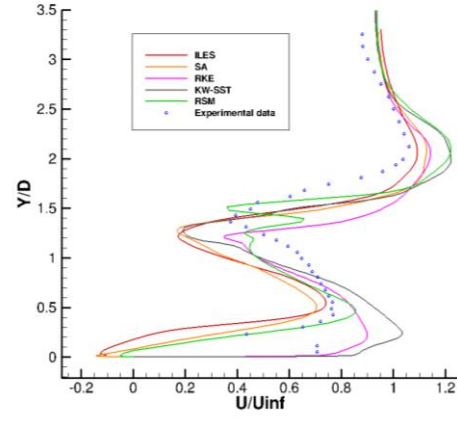The stream-wise velocities at the separation zone are comparatively better than ILES results. The next best model than kω-sst at the separation region is Spalart Allmaras but the height of separation zone is thinner. The thinnest separation zone is predicted by the realizable k-ϵ model. RSM model shows comparable results to the ILES.

67

As we move upwards from the separation zone, only ILES follows with the experimental data. All the RANS models show discrepancy by predicting higher stream-wise velocities than the ILES and experimental results. The lambda shock positions are also seen to be under-predicted by the RANS models. Out of all RANS models, lambda shock position is best predicted by kω-sst but still with major discrepancy compared to the experimental data. The experimental data shows the position of lambda shock at Y/D =2 whereas kω-sst predicts to be around at Y/D=1. This discrepancy could be due to the unsteady behaviour of the flow at the windward side of the jet plume. Thus, the steady simulation (RANS) couldn't capture the shock position correctly.

Figure 5-22b is at X/D=2 position from the jet-hole. The region near the wall is poorly predicted by the RANS models. SA and RSM follow the ILES trend of under-predicting from the experiment whereas kω-sst and realizable-k-ϵ over-predicts. At other places of the profile, RANS results are reasonably good with experiment and competitive with ILES. Moving downstream, at X/D = 3, the trend of discrepancy at the bottom wall region and nearness to the experiment at the upper region similar to ILES results is followed as in figure 5-22c. At X/D = 4 and X/D = 5 (figures 5-22d and 5-22e respectively), realizable k-ϵ and kω-sst results move towards the experiment and very competitive with the ILES data. Only, Spallart Allmaras and Reynolds Stress model still show some discrepancy at the bottom region. Also, to be noticed is that the recirculation zone at the leeward side of the jet plume is under-predicted by kω-sst and realizable k-ϵ but over-predicted by the Spalart Allmaras and Reynolds Stress model.
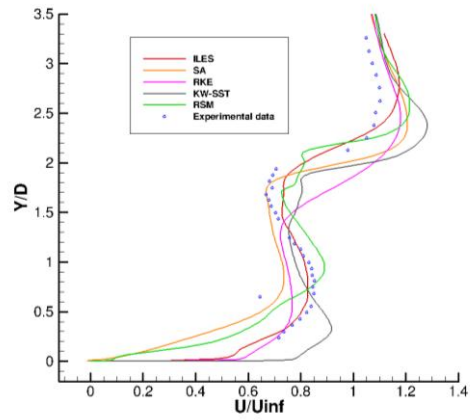
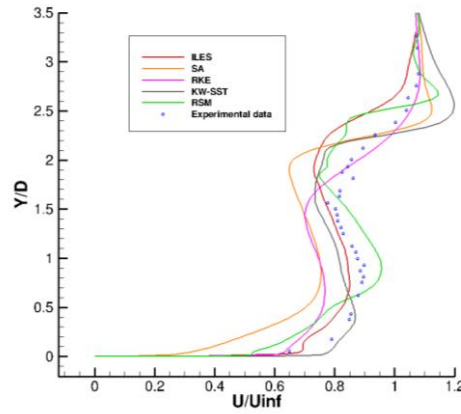## 5.2.2 Y-velocity profiles

(a)
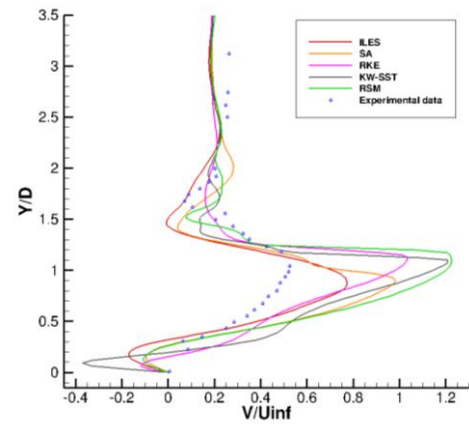
(b)
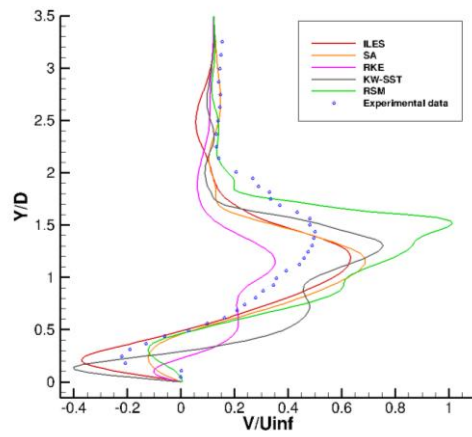
(c)
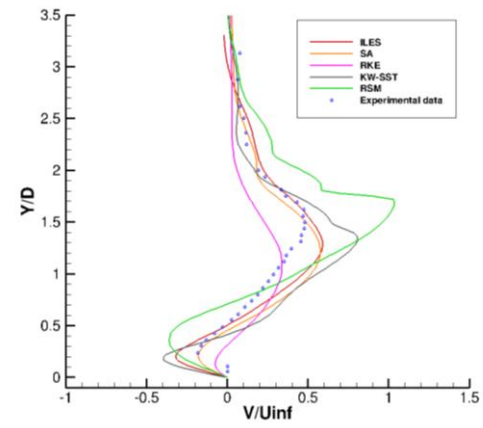
(d)
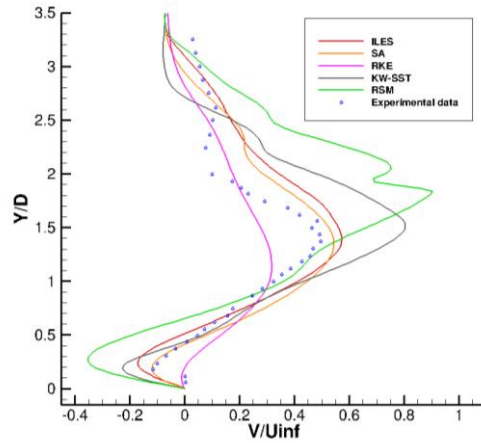
(e)

Figure 5-23 Comparison of Y-velocity profiles of four RANS models, ILES and experiment at different locations (a) X/D = -1.5 (b) X/D = 2 (c) X/D = 3 (d) X/D = 4 (e) X/D = 5
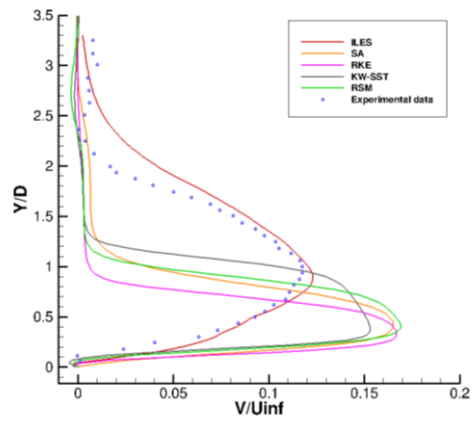
Figure 5-23 are the plots that compare the wall normal velocities (normalised by dividing with V_{inf}) for RANS, ILES and experiment. Fig 5-23a shows the discrepancy of RANS compared to experiment due to same reasons as in figure 5-22a. The incorrect prediction of shock position by RANS credits to its steady behaviour unlike the real unsteady behaviour at the windward side of the jet plume. All the RANS models predict the lambda shock at a height of Y/D=1 unlike the experimental data depicting at Y/D =2. Also, figure 5-23a shows the wall normal velocities are higher for RANS within the region below lambda shock. Out of four RANS models used, kω-sst shows comparatively better results at position X/D=-1.5 although it is far away from the experimental result.

The wall normal velocities plotted at locations downstream from the jet plume show good results for RANS models. Figure 5-23b, 5-23c, 5-23d over-predicts slightly from the experiment but show competitive results with ILES whereas Spalart Allmaras at position X/D = 5 (figure 5-23e) shows close results to the experiment. Overall, for wall normal velocities in the downstream direction, Spalart Allmaras model seems superior to other RANS models and very competitive with ILES.

70

5.2.3 Pressure profiles

(a)

(b)

(c)

Figure 5-24 Comparison of pressure profiles of four RANS models, ILES and experiment at different locations (a) Z/D = 0 (b) Z/D = 1 (c) Z/D = 2

Figure 5-24 presents the comparison plots for the absolute pressure distribution (normalised by dividing with P_{inf}) on the bottom wall of JISC setup. Pressure distributions are non-dimensionalised by the main-inflow pressure. Experiment shows that pressure rises at the separation zone, further rises at the recirculation zone ahead of the jet plume and drops heavily at the recirculation zone just after the jet plume. Gradually, the pressure rises downstream. This

behaviour is seen at planes Z/D = 0, 1, 2 (fig 5-24a, 5-24b, 5-25c), though the effect diminishes as we move away from the mid-plane.

Due to the wrong prediction of lambda shock positions by the RANS models, the initial positions of X/D (around X/D < -2), the pressure plot is flat. The discrepancy can be seen in all the plots (fig 5-24a, 5-24b, 5-25c). Out of all the RANS models, kω-sst is nearest to the experiment because this RANS model is better for predicting the lambda shock. RANS models predict smaller separation zone than the experiment and ILES. Due to smaller separation zone, higher pressure is predicted at that region whereas ILES under-predicts as in figure 5-24a. Also, RANS models show sharp drop in pressure when shifting from separation zone to the recirculation zone just ahead of the jet plume. Experiment shows little hint of it whereas ILES shows no sign. Again, at the recirculation zone, RANS models over-predict pressure value. At recirculation zone just after the jet plume, Spalart Allmaras and RSM model show good concurrency with experiment and predicts better than ILES. At downstream positions, pressure values are under-predicted by RANS models but sooner catch-up with the experiment at around X/D=4.

As we move away from the mid-plane (Z/D = 0), the shock positions are predicted more worst and the downstream results move a little away (fig 5-24b, 5-24c) as compared to fig 5-24a. This may be due to the coarse mesh away from the jet plume region. Also to be noticed is figure 5-24c where kω-sst shows good results at regions near the jet plume (-1 < X/D < 1). Except at the separation region, RANS models seem to be competitive with ILES.

5.2.4 Turbulent kinetic energy profiles

(a)
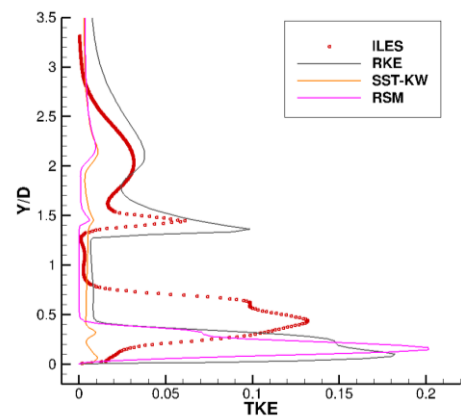
(b)
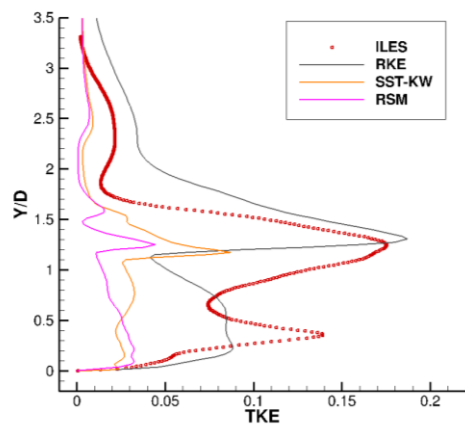
(c)
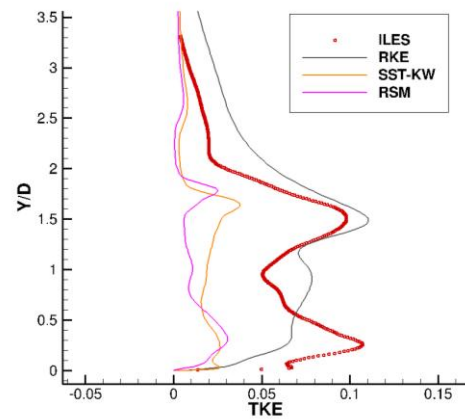
(d)
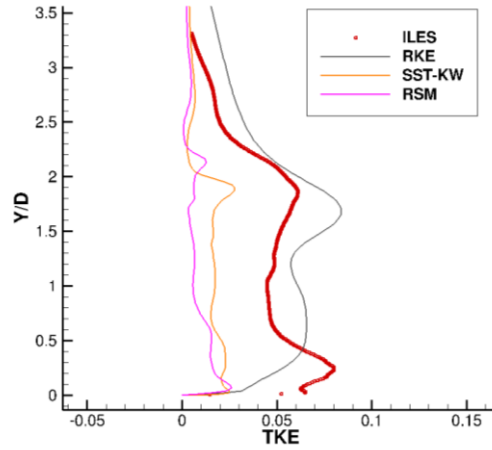
(e)

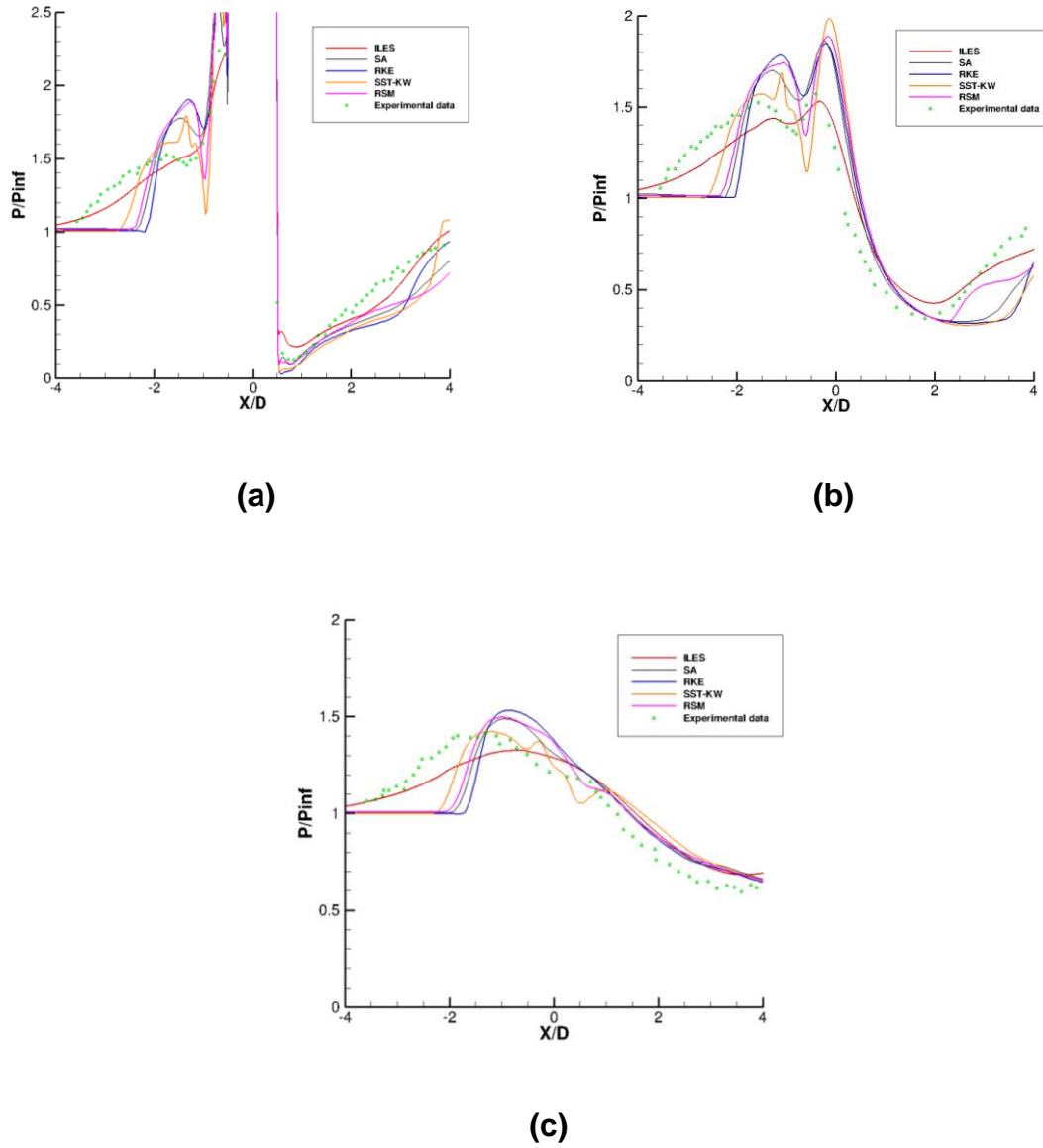**Figure 5-25 Comparison of TKE profiles of four RANS models and ILES at different locations (a) X/D = 0 (b) X/D = 1 (c) X/D = 2 (d) X/D = 3 (e) X/D = 4**
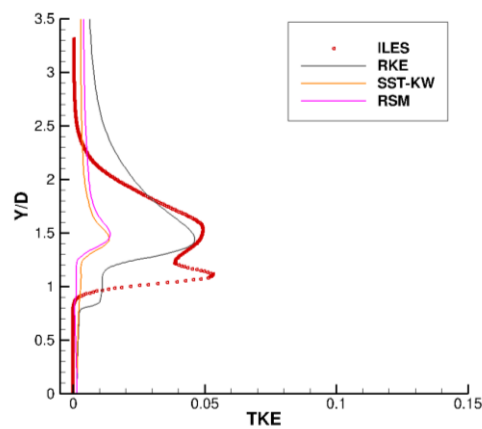
Comparison of TKE plots (normalised by dividing with U_{inf}^2) are shown in figure 5-25. Three RANS models (except Spalart Almaras which is a one-equation model) are compared with available ILES data. It can be seen clearly that only realizable k-ϵ model follows the ILES trend whereas other models incorrectly predict very less TKE. Only in figure 5-25b, RSM show some existence of TKE but at incorrect height compared to ILES.

Turbulent Kinetic Energy is due to the generation of eddies and increment in TKE means that the production terms are bigger than the loss terms. Only Realizable k-e model (out of RANS models) is able to correctly predict the production and loss terms. It can also be noticed (from fig 5-25a, 5-25b, 5-25c, 5-25d, 5-25e) that maximum TKE is found in the mixing region because the jet fluid flows mainly in the windward side of the jet plume. Maximum TKE is seen at X/D =2 at a height of 1.5D where maximum mixing occurs. Also, smaller peaks of TKE can be seen at height of 0.5D, which is because of the generation of eddies. It can be concluded that maximum TKE can be found between X/D =1 to X/D =3 and below Y/D =2.5.

5.2.5 Passive scalar profiles
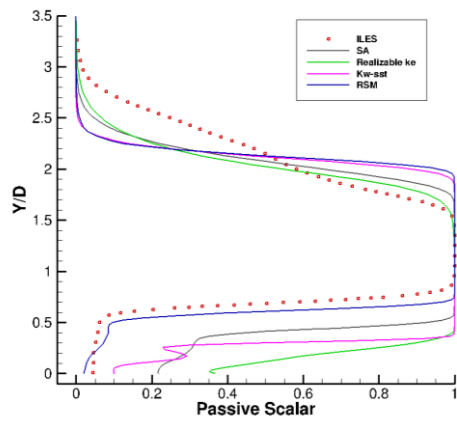
(a)

(b)
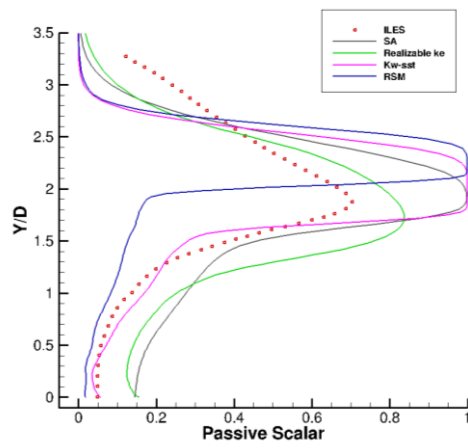
(c)
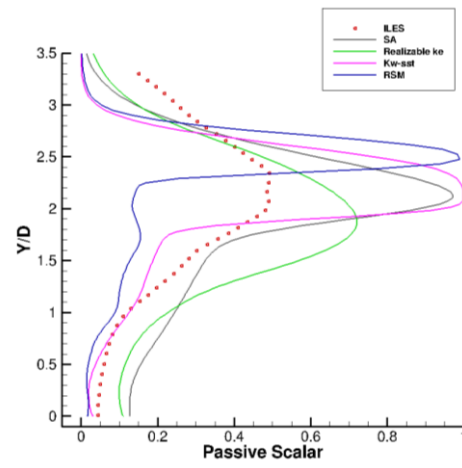
(d)
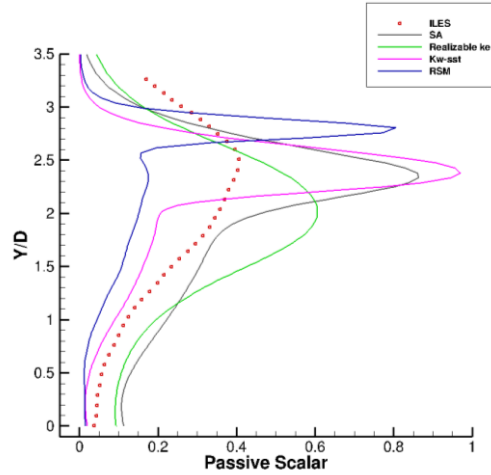
(e)

Figure 5-26 Comparison of passive scalar (air mass fraction) profiles of four RANS models and ILES at different locations (a) X/D = 1 (b) X/D = 2 (c) X/D = 3 (d) X/D = 4 (e) X/D = 5

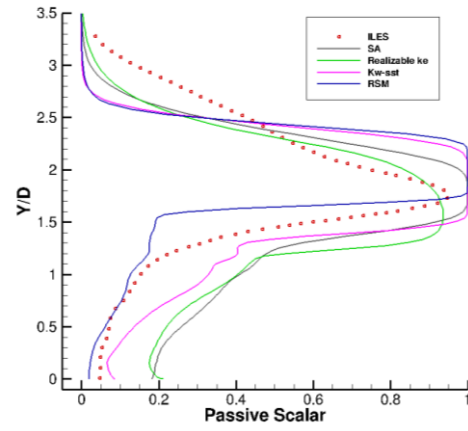Figure 5-26 presents the passive scalar plots on the mid-plane (Z/D = 0) at different locations (X/D =1, 2, 3, 4, 5) downstream of the jet plume. Figure 5-26 explains the mixing phenomena occurring at the windward side of the jet plume and progressive dilution downstream. Mixing is enhanced by the turbulent flow therefore the inlet has been allowed with supersonic turbulent boundary layer. Comparison of incoming turbulent and laminar flow has been investigated by Kawai and Lele [2]. The paper suggests that mixing doesn't happen significantly for the incoming laminar flow.

Passive scalar for the given flow setup have been investigated using four different RANS models and compared with the ILES results. Out of investigated RANS models, Realizable-k-ε seems to be the best fit although it over-predicts the ILES results. Progressive dilution is noticed from figures 5-26a to 5-26e. Except realizable k-ε, other RANS models are not able to show significant mixing until X/D =4 (fig 5-26d). Spalart Allmaras and kω-sst seems to predict the correct jet trajectory but fails to predict mixing process. At X/D =1 (fig 5-26a), RSM predicts correct volume fraction of air whereas Realizable-k-ε shows maximum spreading at the leeward side of the jet plume. Similar over-prediction

76

of passive scalar profile at the leeward side of the jet plume is noticed for realizable k-ϵ and kω-sst at all stations and for Spalart Allmaras at X/D = 1 and X/D = 2 (fig 5-26a, 5-26b). Also to be noticed is that all RANS models under-predict the passive scalar profile at a small region above the jet trajectory.

5.2.6 Jet penetration

Jet penetration height and angle has been estimated by using the probe variable in CFD Post and placing at the centre of Mach disk. Jet penetration height has been tabled in table 5-1. Theoretical value of jet penetration is calculated to be 1.4D (= 5.6mm) by Rana et al. [3]. Comparing with the theoretical value, kω-sst over-predicts whereas other RANS turbulence models under-predicts.

Table 5-1 Comparison of jet penetration height for standard JISC case with J = 1.7

	Theoretical (mm)	Computed (mm)	Error
Spalart Allmaras		5.30	-5.3%
Realizable k-ϵ	5.6	5.32	-5%
Kω-sst		5.85	4.4%
Reynolds Stress model		4.92	-12.1%

Table 5-2 compares the jet penetration angle predicted by the RANS models with the experimental measure. Santiago and Dutton [1] measures the jet penetration angle to be 55 degrees which is best predicted by RSM model. All the RANS models under-predict the jet penetration angle.

Table 5-2 Comparison of jet penetration angle for standard JISC case with J = 1.7

	Experimental (degrees)	Computed (degrees)	Error
Spalart Allmaras		43.50	-20.9%
Realizable k-ϵ	55	39.90	-27.4%
Kω-sst		43.07	-21.7%
Reynolds Stress model		54.76	-0.4%

Chapter 6: Numerical investigation on JISC with J = 0.3 (derived from Hyshot-II case)

6.1 Boundary conditions

The computational domain and use of finest mesh is similar to the previous JISC case with J = 1.7. Materials properties of air and hydrogen have been selected where cold hydrogen is injected from the jet port. The same mass diffusivity constant has been used. There are few changes in boundary conditions. For the new jet-to-cross-flow momentum flux ratio of 0.3, static properties of cross-flow air have been maintained but the static properties (pressure and temperature) of cold hydrogen jet have been calculated as shown in Appendix C. Initial hydrogen mass fraction at jet inlet has been enabled with value 1. Also, a major change is with pressure outlet boundary type at the outflow instead of pressure far-field. This is done because pressure far-field boundary type is a reflecting boundary type and unexpected shock wave with recirculation zone is formed as in fig 6-1. Solver settings have been adjusted similar to the previous case.
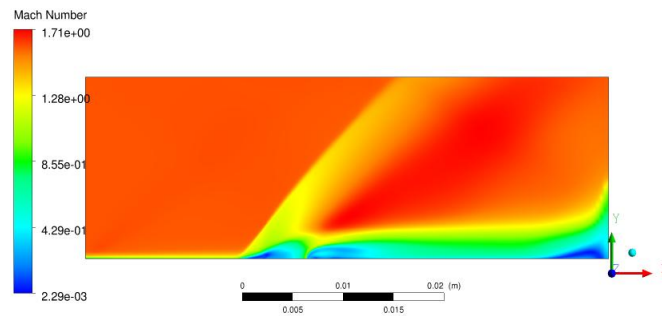

Figure 6-1 Mach number contour at Z/D = 0 mid-plane using realizable k-ϵ model for pressure far-field boundary type at the outflow.

6.2 Qualitative Analysis

6.2.1 Mach number contours at Z/D = 0 plane

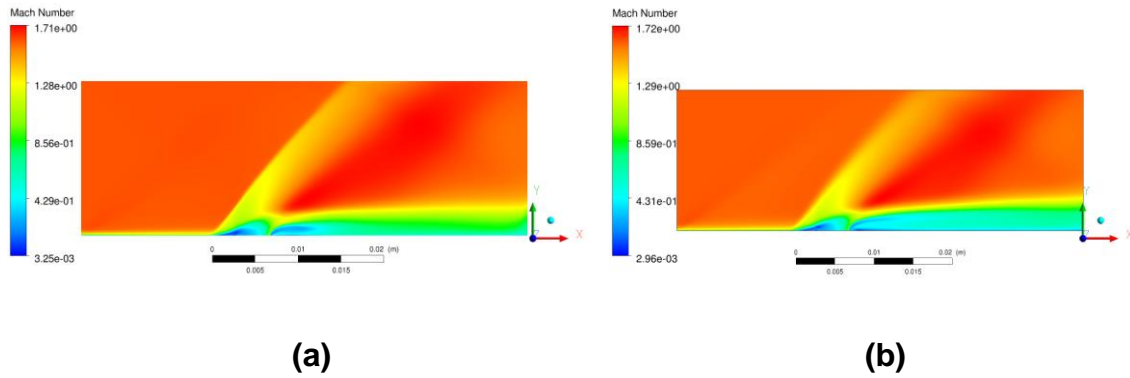(a)   (b)

Figure 6-2 Mach number contours at Z/D = 0 mid-plane (a) realizable k-ϵ (b) SA

Referring to the previous JISC case, realizable k-ϵ best predicts the mixing process whereas SA model best predicts the jet trajectory. Thus, these two RANS models have been chosen for the investigation of this case. Mach contours seen in figure 6-2 are for the cold hydrogen injected into supersonic air cross-flow. Unlike the real case of immediate combustion after injection, the study is done for understanding the flow behaviour of the gases (assuming non-reacting), jet penetration and mixing phenomena.

Similar to the JISC case, the jet injection acts as a barrier for the supersonic cross-flow and flow features like bow shock, barrel shock, and recirculation zones can be figured out. Jet trajectory is seen to be mostly horizontal. Mach contours are almost constant before the jet injection. The recirculation zone just before the jet plume is the area where the jet fuel will be entrained. This entrainment of jet fuel helps in early combustion provided that the temperature is sufficient for combustion. Early combustion improves fuel burning as the residence time in the combustion chamber is very short. Figure 6-2a and 6-2b (realizable k-ϵ and SA) have similar flow structures except the recirculation zone behind the jet plume. Quantitative analysis of the flow at later stage of this section will make the study even more clear.
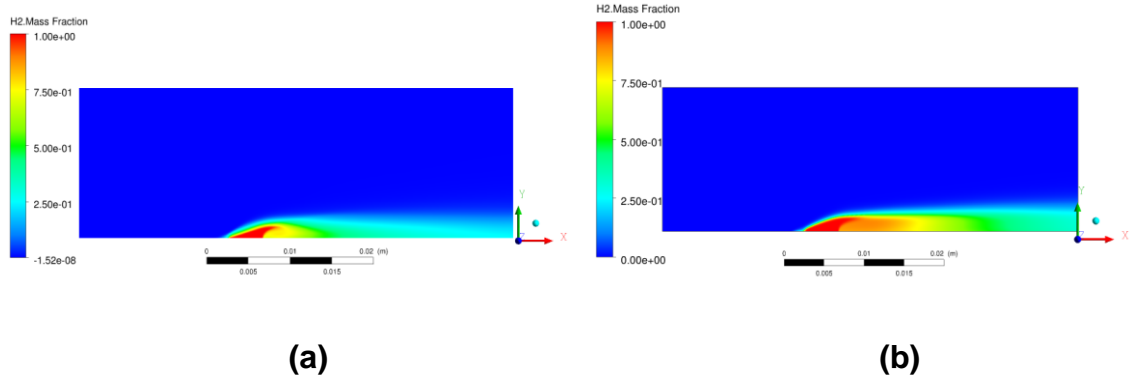
6.2.2 Passive scalar contours at Z/D = 0 plane

<div align="center">(a)   (b)</div>

Figure 6-3 Passive scalar (hydrogen mass fraction) contours at Z/D = 0 mid-plane (a) realizable k-ϵ (b) SA

Passive scalar contours as seen in figure 6-3 show jet fluid following the cross-flow direction, immediately. Compared with JISC case (J = 1.7), this case with J = 0.3 has smaller jet penetration height. Mixing process starts immediately after the jet injection. It can also be noticed that the spreading rate at the jet injection is higher for SA model (fig 6-3b) than realizable k-ϵ model (fig 6-3a). This results in higher hydrogen mass fraction at the surface of bottom wall in the leeward side of the jet plume and slower mixing for SA model. The point that has to be recalled from the previous JISC case is that realizable k-ϵ best predicts the mixing process whereas SA model is better with predicting the jet trajectory.

6.2.3 Turbulent kinetic energy contours at Z/D = 0 plane

Figure 6-4 shows the contours of TKE at mid-plane. High TKE can be seen in the windward side of the jet plume. High TKE is seen at windward side of the jet plume due to high shear layer between the fluids. Also, in the downstream recirculation zone region, high TKE is seen due to the formation of counter rotating vortices. After X/D = 3, TKE diminishes rapidly.
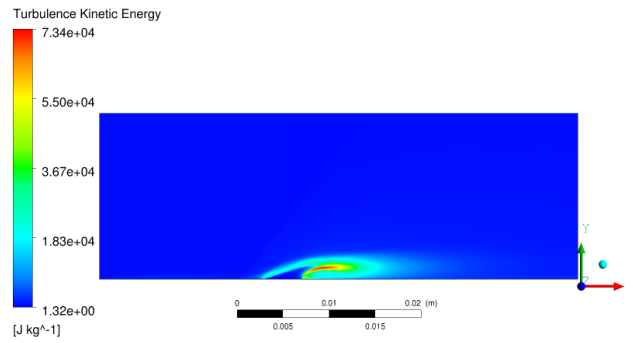
Figure 6-4 Turbulent kinetic energy contours at Z/D = 0 mid-plane

6.2.4 Mach number contours at Y/D = 0.5 plane

(a)

(b)
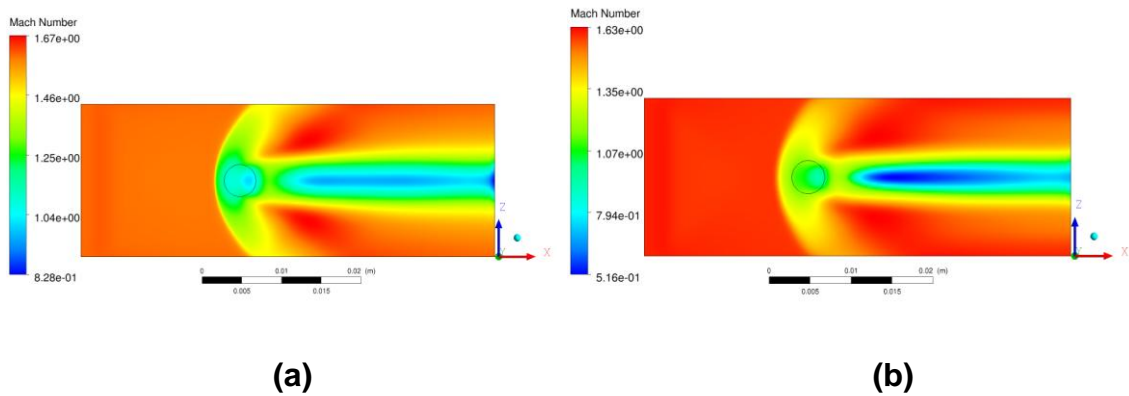
Figure 6-5 Mach number contours at Y/D = 0.5 plane (a) realizable k-ϵ (b) SA

Mach number contours at a height of Y/D =0.5 have been plotted in figure 6-5. Due to the obstruction created by jet, there is a clear separation line before the jet plume. At downstream, clear separation can be noticed between two fluid regions.

6.2.5 Passive scalar contours at Y/D = 0.5 plane

<center>(a)</center>

<center>(b)</center>
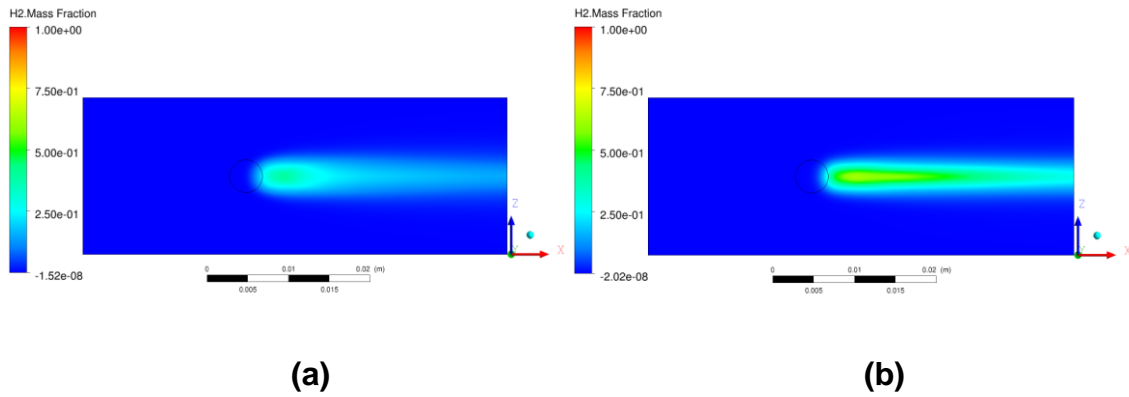
Figure 6-6 Passive scalar (hydrogen mass fraction) at Y/D = 0.5 plane (a) realizable k-ε (b) SA

Passive scalar contours on Y/D =0.5 plane has been shown in figure 6-6. Immediate mixing after the jet injection is predicted by both the turbulence models. Realizable k-ε model (fig 6-6a) shows higher mixing of fluids than SA model (fig 6-6b).Progressive dilution is seen further downstream.

6.2.6 Turbulent kinetic energy contours at Y/D = 0.5 plane
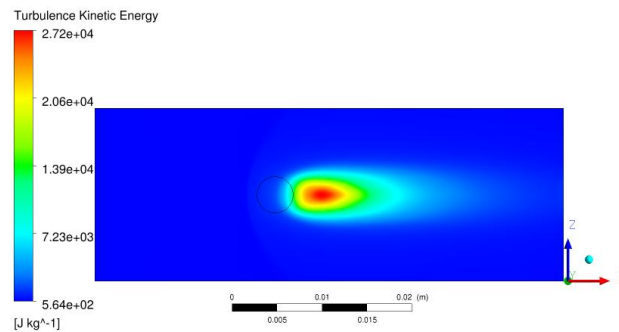
**Figure 6-7 Turbulent Kinetic energy contours at Y/D = 0.5 plane**

Figure 6-7 shows the TKE contours at Y/D = 0.5 plane. The plot depicts high TKE at downstream of jet injection hole. This is actually the region where high shear layer between fluids occur. Further downstream, TKE is dissipated rapidly.

6.2.7 Mach number streamlines at YZ plane

(a)

(b)

(c)

(d)

(e)

(f)

(g) **(h)**
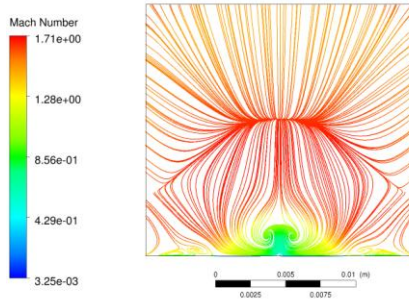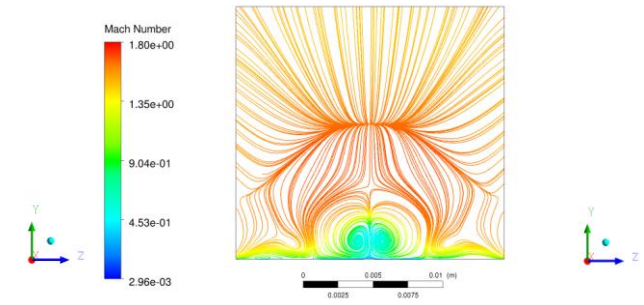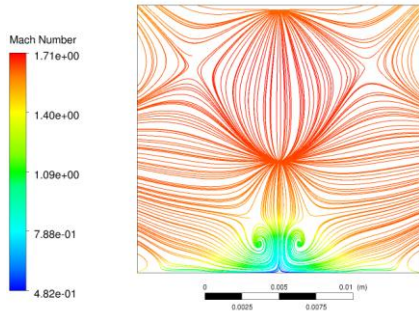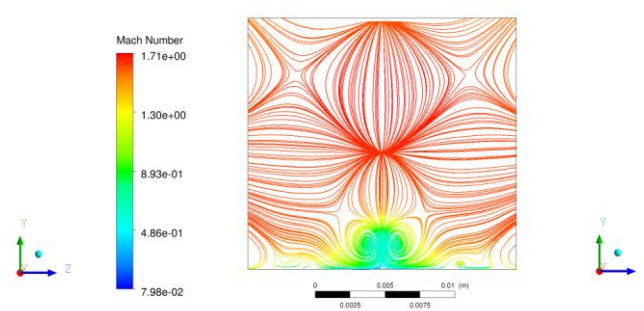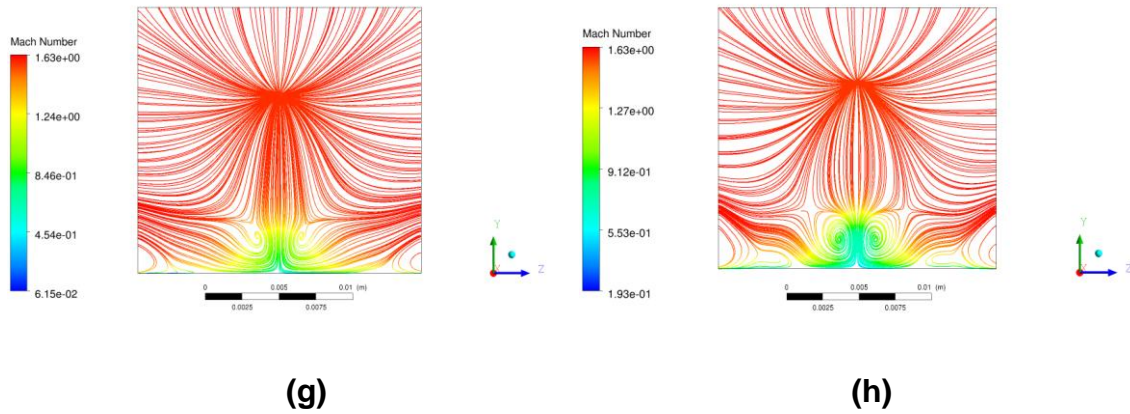
Figure 6-8 Mach number streamlines at YZ plane at different locations for two different RANS models (a) at X/D = 1 for realizable k-ϵ model (b) at X/D = 1 for SA model (c) at X/D = 3 for realizable k-ϵ model (d) at X/D = 3 for SA model (e) at X/D = 5 for realizable k-ϵ model (f) at X/D = 5 for SA model (g) at X/D = 7 for realizable k-ϵ model (h) at X/D = 7 for SA model
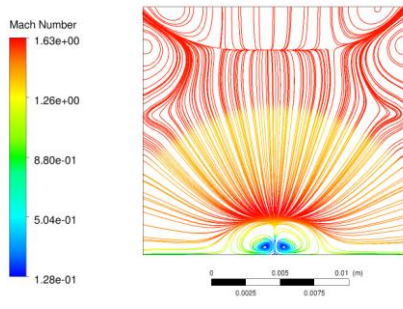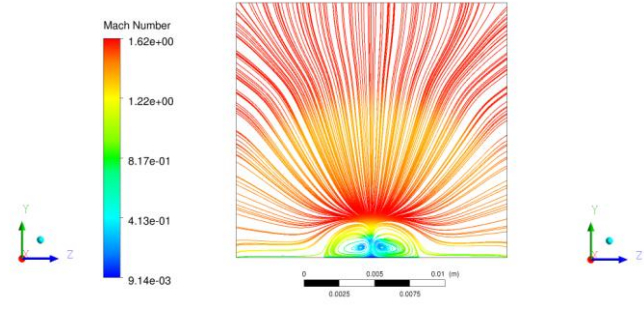
Figure 6-8 shows the Mach number streamlines at different location downstream of jet injection. CRVs are formed just after the injection. These counter rotating vortices play important role in mixing process. Counter rotating vortices that are formed are very symmetrical. SA model predicts very slight growth of CRVs as we move downstream whereas realizable k-ϵ predicts just the increase in height of CRVs. The growth of CRVs is not very prominent in this flow setup compared to the previous case because of the decreased jet-to-cross-flow momentum flux ratio. This decreased jet-to-cross-flow momentum flux ratio doesn't provide enough strength to the flow to entrain fluids in CRVs. Thus, the height of CRVs keeps increasing but not the size. At X/D = 5 (fig 6-8e), there is a hint of another very small trailing counter rotating vortices formed which enhances the mixing process.

6.2.8 Passive scalar contours at YZ plane

(a)

(b)

(c)

(d)

(e)

(f)

(g)   **(h)**
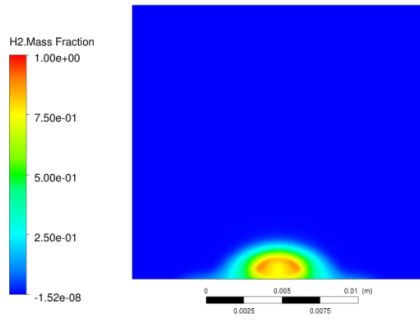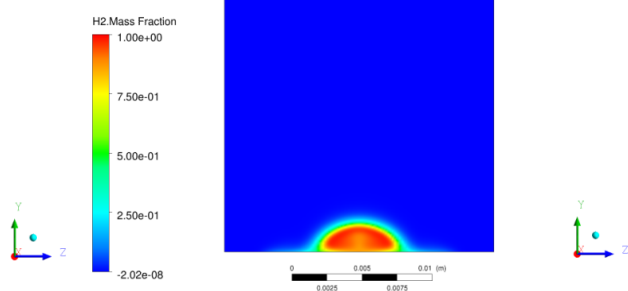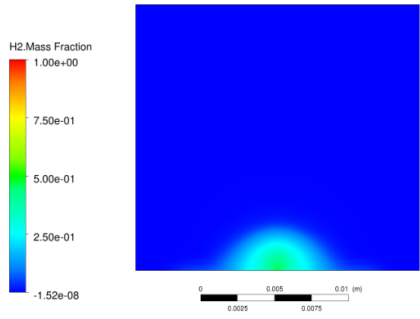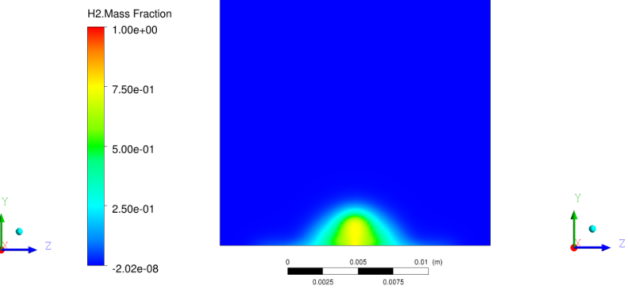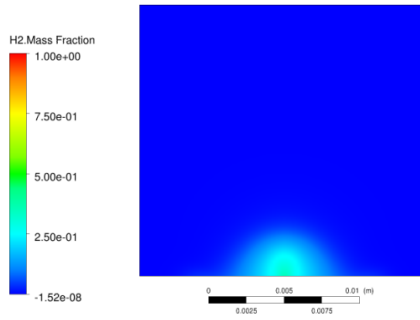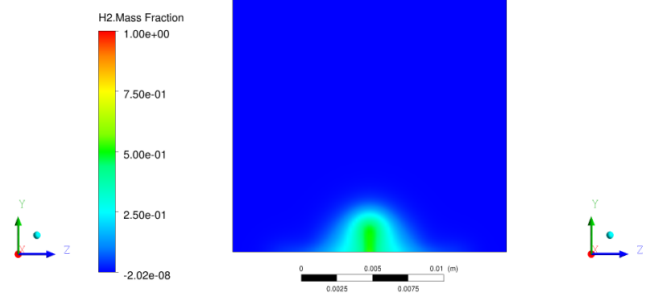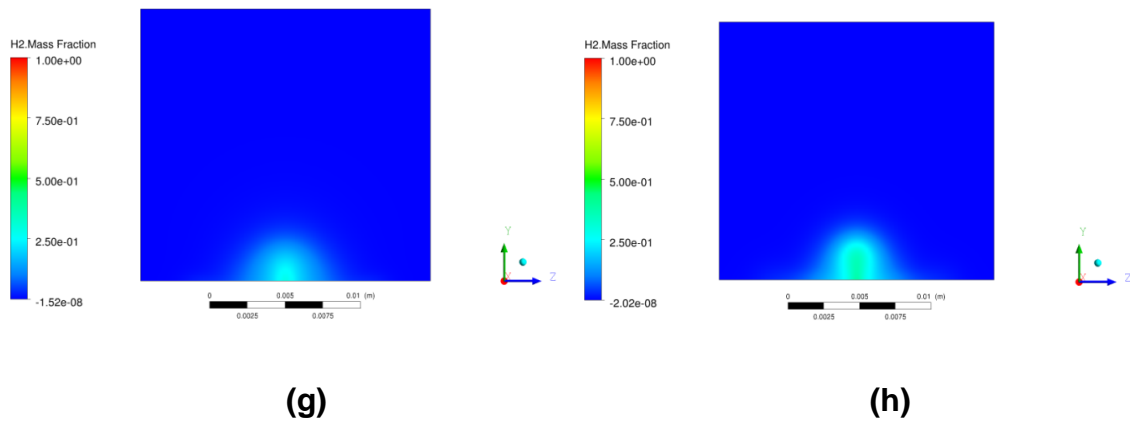
Figure 6-9 Passive scalar (hydrogen mass fraction) contours at YZ plane at different locations for two different RANS models (a) at X/D = 1 for realizable k-ϵ model (b) at X/D = 1 for SA model (c) at X/D = 3 for realizable k-ϵ model (d) at X/D = 3 for SA model (e) at X/D = 5 for realizable k-ϵ model (f) at X/D = 5 for SA model (g) at X/D = 7 for realizable k-ϵ model (h) at X/D = 7 for SA model

Figure 6-9 shows the passive scalar (hydrogen mass fraction) contours. Mixing process starts as soon as the jet in injected and progressive dilution happens rapidly downstream. Clearly, realizable k-ϵ predicts better mixing than SA. Also, SA predicts jet trajectory centreline at increased height than realizable k-ϵ. Referring to previous JISC case, realizable k-ϵ best predicts the mixing phenomena whereas SA model best predicts the jet trajectory.

6.2.9 Passive scalar contours at YZ plane

(a)

(b)

(c)

(d)
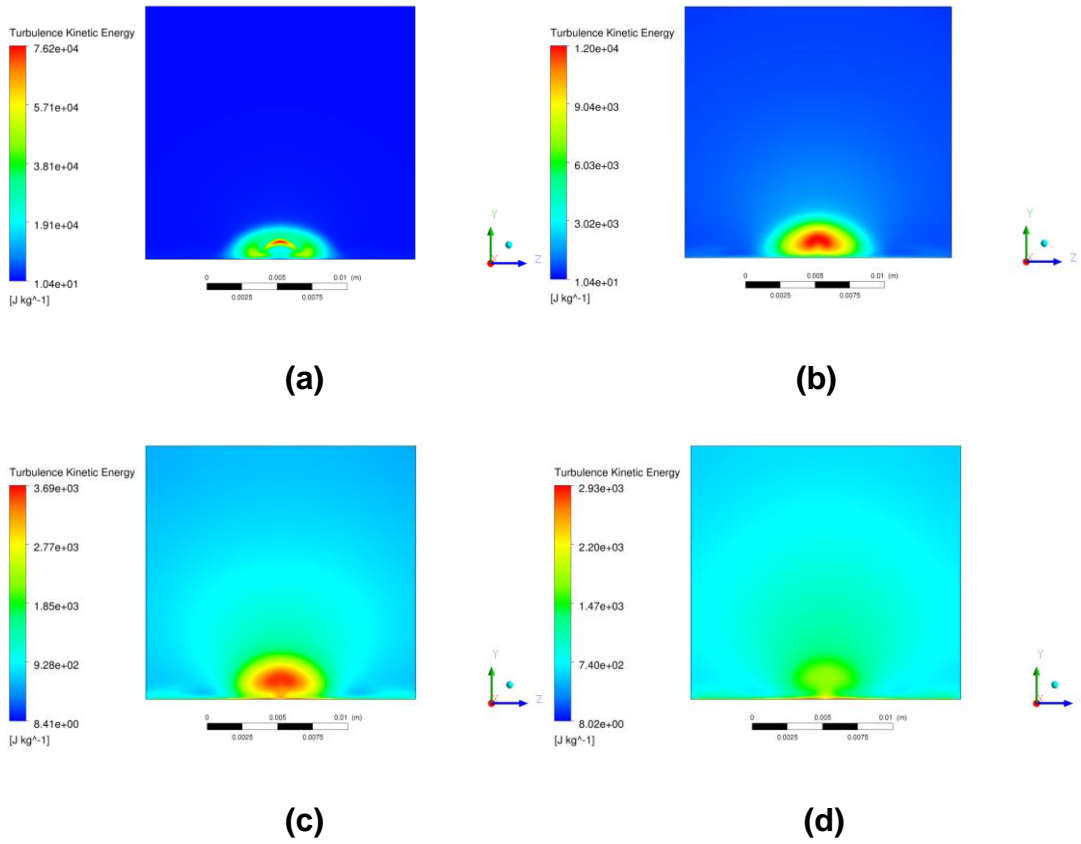
Figure 6-10 Turbulent Kinetic Energy contours at YZ plane at different locations (a) at X/D = 1 (b) at X/D = 3 (c) at X/D = 5 (d) at X/D = 7

TKE contours at X/D = 1, 3, 5, 7 planes have been shown in figure 6-10. As discussed earlier, high TKE is seen near the jet injection hole. In figure 6-10a, maximum TKE is seen at the region of high shear layer between fluids and at origin of CRVs. TKE dissipates quickly downstream as seen in figures 6-10b, 6-10c, 6-10d.

6.3 Quantitative Analysis

6.3.1 X-velocity and Y-velocity profiles

(a)   (b)
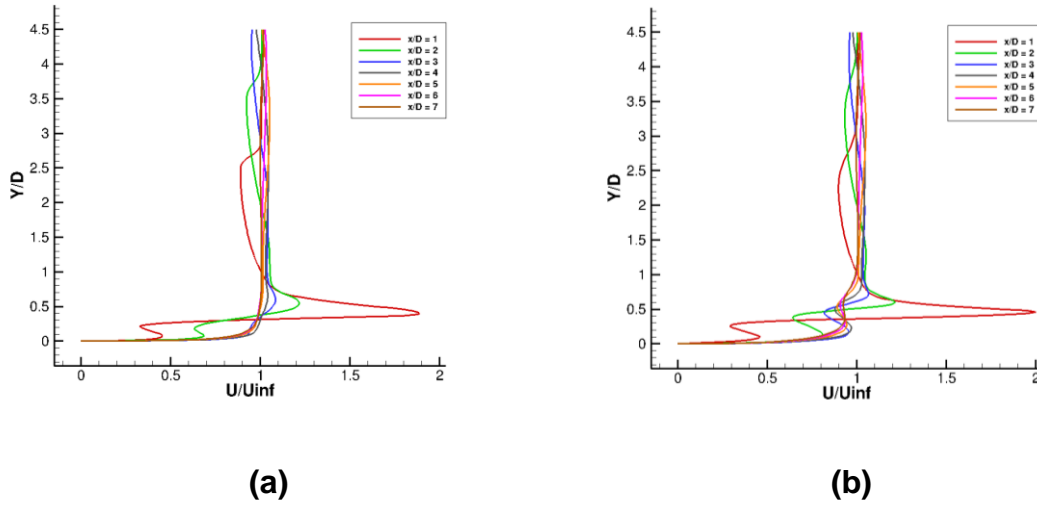
Figure 6-11 X-velocity profile at different locations downstream on Z/D = 0 plane (a) realizable k-ϵ (b) SA

(a)   (b)
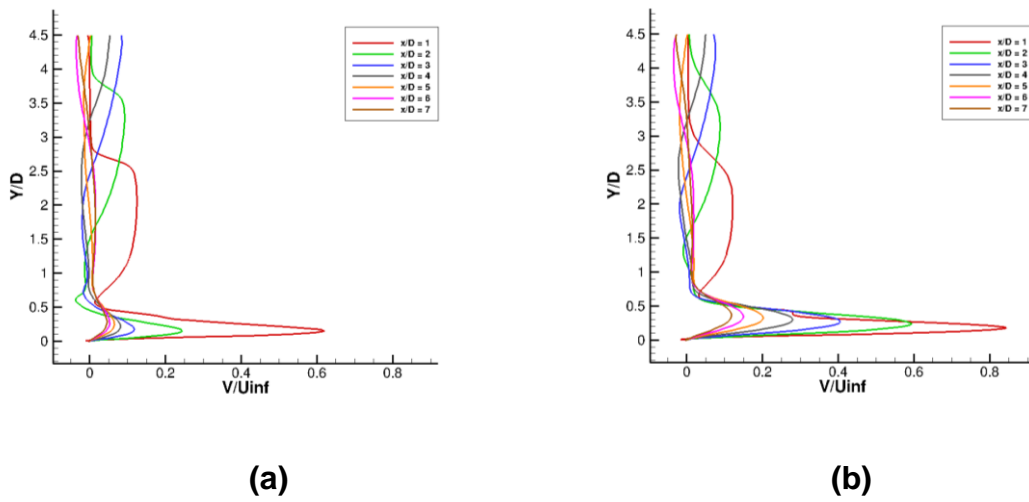
Figure 6-12 Y-velocity profile at different locations downstream on Z/D = 0 plane (a) realizable k-ϵ (b) SA

Figures 6-11 and 6-12 represent the stream-wise normalised by dividing with U_{inf}) and wall normal velocities normalised by dividing with V_{inf}) at the Z/D = 0 mid-plane. The velocities are plotted at different locations (X/D = 1, 2, 3, 4,

5, 6, 7) for realizable k-ϵ and SA models (fig 6-11a and 6-11b respectively). Stream-wise velocity plot in figure 6-11 explains the existence of recirculation zone at X/D =1. The recirculation zone extends till X/D =2. At X/D = 3, recirculation zone vanishes and is left with a kink which refers to the counter rotating vortices. As we go downstream, the CRVs increase in height and the free-stream velocities profile become smoother. Comparing figures 6-11a and 6-11b, SA models predicts stronger CRVs at downstream positions. Figure 6-12 shows wall normal velocities at corresponding locations. Also, for wall normal velocities, the profiles become smoother as we move downstream.

6.3.2 Passive scalar profiles

(a)   (b)
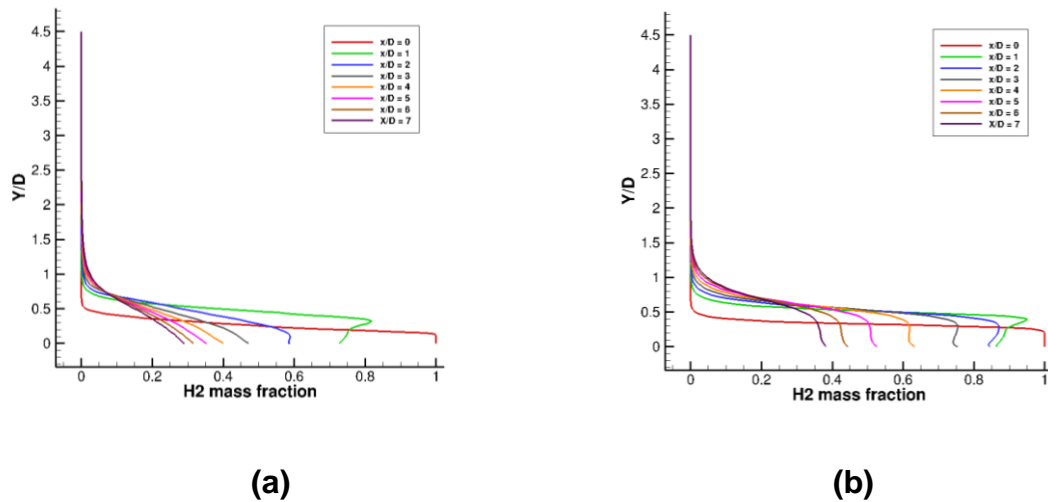
Figure 6-13 Passive scalar (hydrogen mass fraction) profile at different locations downstream on Z/D = 0 plane (a) realizable k-ϵ (b) SA

Figure 6-13 shows passive scalar (hydrogen mass fraction) plots at different location from X/D = 0 to 7 for realizable k-ϵ and SA turbulence models. It can be deduced from figure 6-13 that hydrogen concentration is higher near the injection hole but covers lesser area. As we move away from the injection hole, hydrogen concentration decreases but covers larger area comparatively. The difference that can be extracted from figure 6-13a and 6-13b (realizable k-ϵ and

SA models respectively) is that SA model predicts higher hydrogen concentration near the bottom wall than realizable k-ϵ model.

As explained by Rana et al. [29], 4-74% of hydrogen concentration in air makes an explosive mixture and the auto-ignition temperature is 800 K. As seen from figure 6-13, realizable k-ϵ predicts hydrogen concentration within the range whereas SA model predicts out of range. Referring to results of JISC, realizable k-ϵ is better with passive scalar prediction and SA is useful only for tracking jet trajectory. Here, hydrogen mass concentration predicted by realizable k-ϵ is within the range. Also, temperatures within combustion chamber for Hyshot-II case are above 1000K which is sufficient to ignite the mixture immediately.

6.3.3 Turbulent kinetic energy profiles
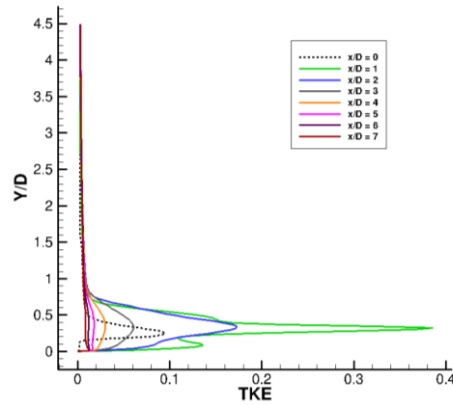
Figure 6-14 Turbulent kinetic energy profile at different locations downstream on Z/D = 0 plane

Figure 6-14 shows the TKE plots (normalised by dividing with U_{inf}^2) at locations from X/D = 0 to 7 which is throughout the length of the domain after the jet injection. It can be understood that TKE peak at X/D = 1 location is due to the high shear layer between fluids and the origin of counter rotating vortices. From figure 6-14, we can deduce that maximum mixing happens between X/D = 1 to 3. As we move downstream, the flow dissipates TKE rapidly.

Chapter 7: Conclusion

This thesis was done to investigate the accuracy of four RANS turbulence models for jet interacting with supersonic cross-flow in supersonic combustors. The numerical investigation details the qualitative and quantitative analysis of the flow for two cases. The first case aims to the standard JISC case of cross-flow with Mach number = 1.6 and jet-to-cross-flow momentum flux ratio = 1.7 where jet and cross-flow are both air. The results have been compared with available experimental and ILES data and discussed the limitations and accuracy of RANS models. The next case is derived from Hyshot-II case (jet-to-cross-flow momentum flux ratio = 0.3) which allows cold hydrogen jet injection to supersonic air cross-flow. The investigation focuses on the ability of RANS models to predict flow structures, flow properties and most importantly mixing phenomena.

The position of lambda shock at upstream position (X/D = -1.5) is not predicted well by the RANS models. This leads to incorrect size of separation zone. Also to be noted is that at downstream positions, the results are very competitive with ILES. The Mach number just before the Mach disk is over-predicted by RANS models. Spalart Allmaras predicts the best with M=4.7 which is still very high compared to M=2.66 (experiment) and M=2.7 (ILES). Realizable k-ϵ fails to predict Mach disk. Jet penetration height and jet penetration angle is best estimated by kω-sst and RSM respectively. Kω-sst and RSM predicts tertiary vortices in the separation zone which was reported by Chenault and Beran [38]. Realizable k-ϵ best predicts passive scalar contours. This means that the mixing phenomena can be better understood using this model. Kelvin-Helmholtz instabilities at the windward side of jet plume are responsible for mixing phenomena. However, the correct jet trajectory is given by Spalart Allmaras. Realizable k-ϵ also shows better results for TKE prediction. The counter rotating vortices are well predicted by RANS models. The most interesting result by RANS is that RSM model predicts asymmetry in the TKE contours at planes between X/D = 3 and X/D = 5. Similar asymmetry has been reported in experiment for unknown reasons. Here, the existence of asymmetry in RANS

modelling could be the affect of additional Reynolds transport equations that redistributes Reynolds stresses since other RANS models with one and two equations models predict perfect symmetry.

Introducing new jet-to-cross-flow momentum value of 0.3 and cold hydrogen injection, the jet penetration decreases by one third. The decreased J value doesn't provide enough strength to the flow to entrain fluids in CRVs. Remaining flow behaviour is similar for both cases.

REFERENCES

[1]   Santiago, J., Dutton, J. "Velocity Measurements of a Jet Injected into a Supersonic Flow", *Journal of Propulsion and Power*, Vol.13, March-April 1997.

[2]   Kawai, S., Lele, S. "Large-Eddy Simulation of Jet Mixing in Supersonic Turbulent Cross-flows", *AIAA Journal*, Vol.48, September 2010.

[3]   Rana, Z. A., Thornber, B. , Drikakis, D., "An ILES Analysis of Transverse Jet Injection in to Supersonic Cross-flow with Synthetic Turbulent Boundary Layer", *49th AIAA Aerospace Sciences Meeting including the New Horizons Forum and Aerospace Exposition,* 4 - 7 January 2011, Orlando, Florida.

[4]   Higgins, K., Schmidt, S., "Simulation of a sonic jet injected into a supersonic cross-flow", *16th Australasian Fluid Mechanics Conference*, Crown Plaza, Gold Coast, Australia. 2-7 December 2007.

[5]   Rana, Z. A., Thornber, B. , Drikakis, D., "Analysis of Hydrogen Injection into the Combustor of Hyshot-II Scramjet Engine using ILES", *AIAA*-2011-050

[6]   Viti, V., Neel, R., Schetz, J.A., "Detailed Flow Physics of the Supersonic Jet Interaction Flow Field", *Physics of Fluids*, Vol.21, 2009.

[7]   Gruber, M. R., Nejad, A.S., Chen, T.H., Dutton J. C., "Large structure convection velocity measurements in compressible transverse injection flow-fields", *Exp. Fluids*, Vol. 12, No.5, 1997, pp. 397–407.

[8]   Rana, Z. A., Thornber, B., Drikakis, D., "Investigation of Sonic Jet Mixing in a Stream of Supersonic Cross-flow using Large Eddy Simulation", *Proceedings of 27th Congress of the International Council of the Aeronautical Sciences* (ICAS-2010), Nice, France, 2010.

[9]   Schetz, J, Billig, F., "Penetration of gaseous jets injected into a supersonic stream", *Journal of Spacecraft.*, Vol. 3, No. 11, November 1966.

[10]   Meilan, Qi, Chen, Z., Fu, R. "Flow structure Of the Plane Turbulent Impinging Jet In Cross Flow", Dept. of Hydro-Engineering, Tsinghua Univ., Beijing 100084, China.

[11]   Kelso, R. M., Lim, T. T., Perry, A. E. (1996), "An experimental study of round   jets in cross-flow", *J. Fluid Mech.*, 306, 111-144.

[12]   Muppidi, S., Mahesh, K., "Direct Numerical Simulation Of Round Turbulent Jets In cross-flow", *J. Fluid Mech*. (2007), Vol. 574, Pp. 59–84.

[13] Van Lerberghe, W., Santiago, J., Dutton, J., Lucht, R., "Mixing of a sonic transverse jet injected into a supersonic flow". *AIAA Journal.* Vol. 38, issue 3 March, 2000.

[14] Peterson, D. M., Candler, G. V., "Hybrid Reynolds-Averaged and Large-Eddy Simulation of Normal Injection into a Supersonic Crossflow", *Journal Of Propulsion And Power* Vol. 26, No. 3, May–June 2010.

[15] Donaldson, C.D., Snedeker, R.S., "A study of free jet impingement. Part 1. Mean properties of free and impinging jets", *J. Fluid Mechanics*, 1971, 45, (2), pp 281–319.

[16] Admason, T. and Nicholls, J., "On the Structure of Jets from Highly Underexpanded Nozzles into Still Air", *Journal of th Aerospace Sciences*, Vol.26:pp. 16–24, 1958.

[17] Chizhikov, A. S., "On the Gas Flow Rate through a Mach Disk In An Underexpanded Jet", *Journal Of Engineering Physics And Thermophysics*, Vol. 82, No. 2, 2009.

[18] Schetz, J. A., Gilreath, H. E., Lubard, S. C., "Fuel Injection and Mixing in a Supersonic Stream", Aerospace Engineering Department, University of Maryland, College Park, Maryland

[19] Walker, R. E., Kors, D. L., "Multiple Jet Study", Aerojet Liquid Rock-et Company, Sacramento, California 95812: Prepared for NASA.

[20] Kovar, A., Schulein, E., "Comparison of experimental and numerical investigation on a jet in a supersonic cross-flow", *The Aeronautical Journal*, June 2006.

[21] Fric, T. E., Roshko, A., "Structure in the near field of the transverse jet. Proc. 7th International Symposium on Turbulent Shear Flows", Stanford University, pp 225-237, 1989

[22] Gruber, M. R., Nejad, A. S., Dutton J. C. "Circular and elliptical transverse injection into a supersonic crossflow - The role of large-scale strucutres" *AIAA*, Paper no. 95-2150, 1995

[23] Gruber, M. R., Nejad, A. S., Chen T. H., Dutton J. C., "Compressibility effects in supersonic transverse injection flowfields". *Phys. Fluids,* 9, 1448 (1997); doi:10.1063/1.869257

[24] Chuech, S. G., Lai, M. C., Faeth, G. M., "Structure Of Turbulent Sonic Underexpanded Free Jets", *AIAA Journal* , Vol. 27, No. 5, May 1989.

[25] Wanga, G., Lub, X., "Effects Of The Jet-To-Crossflow Momentum Ratio On A Sonic Jet Into a Supersonic Crossflow", *Theoretical & Applied Mechanics Letters,* 1, 012005 (2011).

[26] Ali, M., Ahmed, S., Sadrul, Islam A. K. M., "The Two-Dimensional Supersonic Flow and Mixing with a Perpendicular Injection in a Scramjet Combustor", *J. of Thermal Science*, Vol.12, no.4.

[27] Van Lerberghe, W., Santiago, J., Dutton, J., Lucht, R., "Mixing of a sonic transverse jet injected intoa supersonic flow", *AIAA Journal.* Vol. 38, issue 3, March 2000.

[28] Cohen, L., Coulter, L., Egan, W., "Penetration and mixing of multiple gas jets subjected to a cross-flow", *AIAA Journal.*Vol. 9, No. 4, April 1971.

[29] Amano, R.S., Sun, D., "Numerical Simulation Of Supersonic Flowfield With Secondary Injection", *24th International Congress Of The Aeronautical Sciences*, 2004.

[30] Spalart, P., Allmaras, S., "A one-equation turbulence model for aerodynamic flows", *Technical Report AIAA-92-0439*, American Institute of Aeronautics and Astronautics, 1992

[31] ANSYS FLUENT 12.0 Theory Guide (2010), ANSYS

[32] Shih, H., Liou, W. W., Shabbir, A., Yang, Z. , Zhu, J. , "A New k-ϵ Eddy-Viscosity Model for High Reynolds Number Turbulent Flows - Model Development and Validation", *Computers Fluids*, 24(3):227-238, 1995

[33] Menter, F. R., "Two-Equation Eddy-Viscosity Turbulence Models for Engineering Applications", *AIAA Journal*, 32(8):1598-1605, August 1994

[34] Gibson, M. M., Launder, B. E., "Ground Effects on Pressure Fluctuations in the Atmospheric Boundary Layer", *J. Fluid Mech.*, 86:491-511, 1978

[35] Launder, B. E., "Second-Moment Closure: Present and Future?", *Inter. J. Heat Fluid Flow*, 10(4):282-300, 1989.

[36] Launder, B. E., Reece, G. J., Rodi, W. , "Progress in the Development of a Reynolds-Stress Turbulence Closure", *J. Fluid Mech.*, 68(3):537-566, April 1975.

[37] Adelp, R., Longo, J. A., Edmunds, H., "Flow field study of Supersonic Jet Exiting into a Supersonic Stream", *DLR*, Institute of Aerodynamics and Flow Technology, Germany

[38] Chenault, C. F., Beran, P. S., "k-ϵ and Reynolds stress turbulence model comparisons for two-dimensional injection flows", *AIAA,* J. 36, 1401 (1998)

APPENDICES

Appendix A Calculation of static properties at inflow conditions for standard JISC case with J = 1.7

A.1 Cross-flow inlet condition

The calculations were done using isentropic relations (equation A-1, A-2)

A.1.1 Temperature

Stagnation temperature, $T_o = 295K$

$$\frac{T_o}{T} = 1 + \frac{\gamma - 1}{2} M^2 \tag{A-1}$$

$$\frac{295}{T} = 1 + \frac{0.4}{2} X \, 1.6^2$$

Static temperature of cross-flow, $T_c = 195.11K$

A.1.2 Pressure

Stagnation pressure, $P_o = 241 \, kPa$

$$\frac{P_o}{P} = \left(1 + \frac{\gamma - 1}{2} M^2\right)^{\frac{\gamma}{\gamma - 1}} \tag{A-2}$$

$$\frac{241000}{P} = \left(1 + \frac{0.4}{2} 1.6^2\right)^{\frac{1.4}{0.4}}$$

Static pressure of cross-flow, $P = 56700.55 \, Pa$

A.2 Jet inlet condition

A.2.1 Temperature

Stagnation temperature, $T_o = 295K$

Using equation A-1,

$$\frac{295}{T} = 1 + \frac{0.4}{2} \, X \, 1^2$$

Static temperature of jet, $T_j = 245.83K$

A.2.2 Pressure

Stagnation pressure, $P_o = 476 \; kPa$

Using equation A-2,

$$\frac{476000}{P} = \left(1 + \frac{0.4}{2} \, 1^2\right)^{\frac{1.4}{0.4}}$$

Static pressure of jet, $P = 251462.131 \; Pa$

Appendix B Calculation of static properties at inflow conditions for JISC case with J = 0.3 (based on Hyshot–II case)

Jet –to-cross-flow momentum flux ratio, $J = 0.3$

Static pressure of cross-flow, $P_c = 56700.55\ Pa$

Using relation for jet penetration from equation 2-1,

$$J = \frac{\gamma_j}{\gamma_c} \cdot \frac{P_j}{P_c} \cdot \frac{M_j^2}{M_c^2}$$

$$0.3 = \frac{1.41}{1.4} \cdot \frac{P_j}{56700.55} \cdot \frac{1^2}{1.6^2}$$

Static pressure of jet with hydrogen injection, $P_j = 43237.185$

Using ideal gas relation ($P = \rho RT$),

For jet with hydrogen injection,

$$43237.185 = 0.08189\ X\ 4124\ X\ T_j$$

Static temperature of jet, $T_j = 128.03K$